Chemical Partitioning and Resultant Effects on Structure and Electrical Properties in Co-Containing Magnetic Amorphous Nanocomposites for Electric Motors

Vincent G. DeGeorge

Submitted in partial fulfillment of the requirements
for the degree of Doctor of Philosophy
in Materials Science and Engineering,
College of Engineering,
Carnegie Mellon University
Pittsburgh, PA

Thesis Advisor:
Prof. Michael E. McHenry

Examination Committee:
Prof. David. E. Laughlin
Prof. Vincent M. Sokalski
Dr. Paul R. Ohodnicki, Jr.

ii. Abstract

The chemical partitioning of Cobalt-containing soft magnetic amorphous and nanocomposite materials has been investigated with particular focus on its consequences on these materials' nanostructure and electrical resistivity. Theory, models, experiment, and discussion in this regard are presented on this class of materials generally, and are detailed in particular on alloys of composition, $(Fe_{65}Co_{35})_{79.5+x}B_{13}Si_2Nb_{4-x}Cu_{1.5}$, for X={0-4at%}, and Co-based, $Co_{76+Y}Fe_4Mn_{4-Y}B_{14}Si_2Nb_4$, for Y={0-4at%}. The context of this work is within the ongoing efforts to integrate soft magnetic metal amorphous and nanocomposite materials into electric motor applications by leveraging material properties with motor topology in order to increase the electrical efficiency and decrease the size, the usage of rare-earth permanent magnets, and the power losses of electric motors. A mass balance model derived from consideration of the partitioning of glass forming elements relates local composition to crystal state in these alloys. The 'polymorphic burst' onset mechanism and a Time-Temperature-Transformation diagram for secondary crystallization are also presented in relation to the partitioning of glass forming elements. Further, the intrinsic electrical resistivity of the material is related to the formation of virtual bound states due to dilute amounts of the glass forming elements. And lastly, a multiphase resistivity model for the effective composite resistivity that accounts for the amorphous, crystalline, and glass former-rich amorphous regions, each with distinct intrinsic resistivity, is also presented. The presented models are validated experimentally on the Co-containing alloys by Atom Probe Tomography performed through collaboration with Pacific Northwestern National Laboratory.

iii. Contents

iv. Acknowledgements

I graciously acknowledge funding for this work from the Department of Energy ARPA-e (Advanced Research Projects Agency - Energy) Grant FOA-0000474.

Personal Acknowledgements

To Dr. McHenry; Because of you, I did more than I otherwise could have done.

To my professors in MSE at CMU and Physics at JCU; because of you I learned more than I otherwise could have learned.

To my group and classmates at CMU; Because of you I worked harder than I otherwise would have - and stayed human. Sam, Alex, Josefina, Hussein, Whitney, Michael, Prya, Natan, Lily, Brian, Miaolei, Ellen, Justin.

To Mr. Rho. Thank you.

To the students I have been able to, and hope to be able to, tutor and teach; because of you I care more about learning than I otherwise would.

To those who had the ability and the opportunity to do this before me; because of you I had examples to follow.

To those who had the ability and not the opportunity to do this; because of you I did my best work.

To my CMU, Oakland, and Newman Center friends; thank you for the place to belong.

To the CMU Humanist League; because of you I explored important ideas that I otherwise would not have.

To the Diocese of Wheeling-Charleston; in thanks, and in hope.

To my 'friends of Friendship;' because of you I was reminded there is more to life than magnets. Rob Poland.

To my friends from Morgantown and JCU; you made me ready for this.

To my family in and around Pittsburgh; thanks for dinner!

To all my grandparents; thanks for the engineering genes, and your love. Nancy DeGeorge. Nel Igne.

To my siblings; we can't experience everything, but together I feel like we've all experienced more. I love you.

To my parents; Because of you I am the person I am. I love you.

To God; from whom all blessings flow.

Chapter 1.0 Introduction: Magnetism and Magnetic Materials

1.1 Context in the Materials Science Paradigm

This work has been completed within the materials science paradigm, in which the structure, properties, processing, and performance of materials are evaluated in their own right and as each relates to the others.

Structure: As amorphous and partially devitrified, that is nanocomposite, materials have been studied over the past +30 years this work focuses on a particular aspect of amorphous nanocomposites, the partitioning of constituent elements during and as a result of crystallization. Chemical partitioning is explored in depth in Chapter 4, in which a mass balance ties local composition, measured through Atom Probe Tomography, to crystal state during the devitrification process. I also relate processing variables to structure by presenting a TTT (Time, Temperature, Transformation) diagram for secondary crystallization in a Co-based alloy in this chapter. Chapter 2 includes a review of the state of amorphous and nanocomposite materials being implemented in electric motors.

Properties: While this class of materials is primarily used for its combination of high permeability and high saturation induction, the material property on which I principally focus in this document is the electrical resistivity of MANCs. In Chapter 5, the electrical resistivity of these materials is tied to structure, specifically that resulting from chemical partitioning, and the formation of Virtual Bound States in this system. And, Chapter 6 explores the relation between processing and properties with a multiphase resistivity model that related the effective resistivity of the composite to its crystallization state. Co-based MANCs' mechanical properties are also considered with respect to this material's use in electric motors in Chapter 2.

Processing: This document deals mainly with three materials' processes: 1) planar flow and melt-spin casting, 2) conventional thermal annealing, and 3) shaping of amorphous ribbon through stamping, cutting, or other means. The rapid solidification techniques used to synthesize amorphous materials are described later in Chapter 1. While advancements in more complicated annealing techniques, i.e. field and strain annealing, are currently underway here I present on the conventional thermal annealing process that partially crystallizes amorphous ribbon and forms MANCs, focusing instead on the less studied secondary crystallization in Chapter 4. In Chapter 2 I also outline current and proposed methods of efficiently shaping amorphous ribbon, one of the chief obstacles facing implementation of amorphous and nanocomposite materials in electric motors.

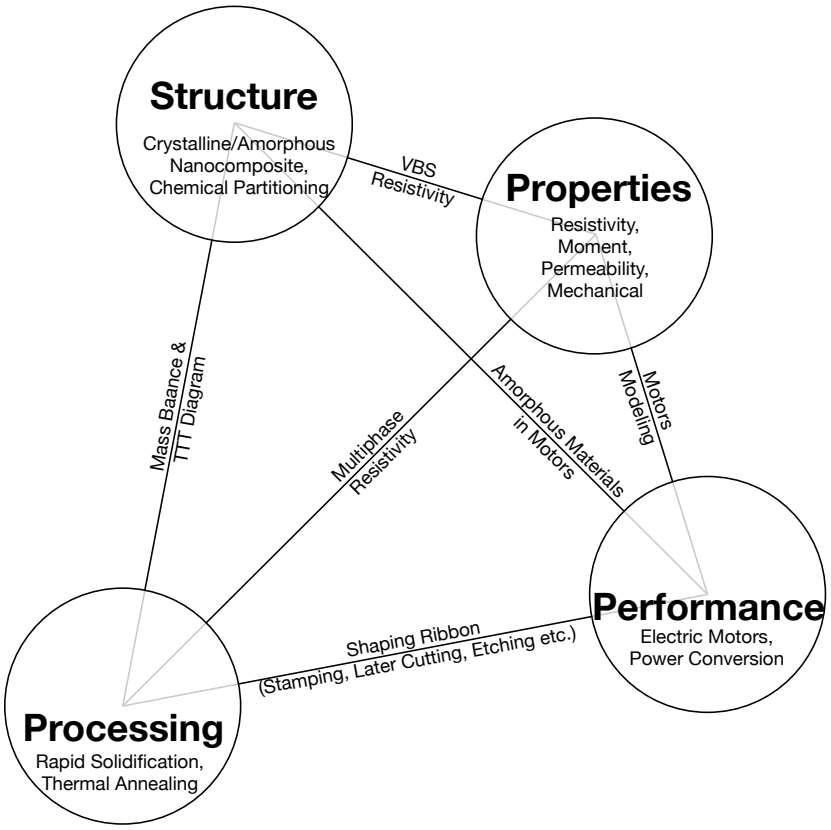

Figure 1.1.1: The Materials Science Paradigm represented by a tetrahedron illustrating that each Structure, Properties, Processing, and Performance are each both distinct and interconnected.

Performance: Amorphous and nanocompsite materials have been used in many applications including magnetic field sensors and power conversion devices. This document reports on prior and current work implementing this technology into electric motors. In Chapter 2 the processing challenges of efficiently shaping ribbon, motor designs featuring amorphous materials, the market potential of MANCs in motors, and finally some performance comparison of Co-based MANCs over convention materials in motors and are all summarized.

1.2 Magnetic Materials

Magnetism in materials is broad in how it is exhibited, but it is fundamental to the nature of matter. Like the mass or charge associated with matter, first principles trace magnetism to the quantum nature of the atom. Of the four atomic quantum numbers two, the spin and orbital angular momentum numbers usually denoted *S* and *L*, respectively, contribute to the magnetism of atoms and in turn matter. Where the magnetic moment of a free electron, $m_{e^-} = \mu_B$, where μ_B is the Bohr Magneton, and has only orbital contributions, an atomic element's magnetic moment can be found by applying Hund's Rules which consider both contributions to magnetism and articulate how a given atom's electron energy levels are filled.

As a material's mass density is determined as atoms collect, order, and form structures with each atom's atomic mass making its contribution, a material's magnetization is likewise an intrinsic property. Where a material's mass density is defined as the sum of each atom's atomic mass normalized per unit volume or number of atoms, similarly a material's *magnetization, **M**,* is the net magnetic moment per unit volume (or mol of atoms) of a material.

However, unlike either mass or density that are scalar quantities magnetic moment is a vector quantity. Thus, where isotropic points - as atomic elements can usually be considered - lead to 14 Bravais lattices, considering the additional symmetry constraints imposed by the chiral magnetic moment vector when it occupies lattice position leads to 36 magnetic Bravais lattices. Similarly, the number of space groups is increased from 230 to 1651[1]. The fundamental symmetry that the magnetic moment, $\vec{\mu}$, introduces is illustrated in Fig. 1.2.1. Here time inversion symmetry breaks symmetry in the chiral magnetic moment vector that is otherwise conserved under mirror inversion.

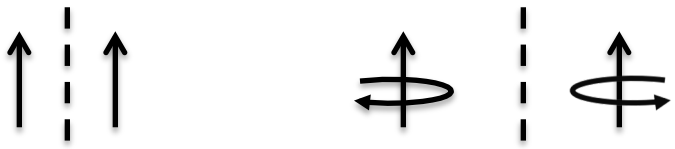

Figure 1.2.1 Though an atom's magnetic moment is often represented by a simple vector arrow, the magnetic moment is in fact a chiral vector with consequences in the magnetic structure of materials.

There are several ways in which atom's magnetic moments commonly arrange, or *order,* with respect to one another. Magnetic dipole moments, $\vec{\mu}$, that are each arranged facing the same way, or that are aligned in

the same direction as shown in figure 1.2.2(B) are called *ferromagnetic* materials, or are said to exhibit *ferromagnetism*. Oppositely, one might consider an array of identical magnetic moments that have no orientational relationship with regard to one another, or are completely un-ordered. This configuration of magnetic moments is a *paramagnet,* and shown in figure 1.2.2 (A). Ferromagnetism and paramagnetism are the focus of the magnetic materials discussed in this document. *Antiferromagnetism* and *ferrimagnetism* describe perfectly ordered configurations of magnetic moments, the later of different magnitudes, oriented antiparallel to one another and are shown in Fig. 1.2.2 (C&D).

These configurations of magnetic moments can be described in terms of ordering and an order parameter, η. The paramagnetic state is an entirely disordered state, $\eta=0$. While the ferromagnetic state is a completely ordered state, $\eta=1$. Physically, the disordering of magnetic moments in a lattice of atoms is a thermally activated phenomena. A material can transition from a completely ordered, $\eta=1$ ferromagnetic state, to a completely disordered, $\eta=0$ paramagnetic state, continuosly with increasing temperature. The temperature below which a magnetic material is ferromagnetic and at and above which a completely disordered state is reached is referred to as the Curie Temperature, T_C.

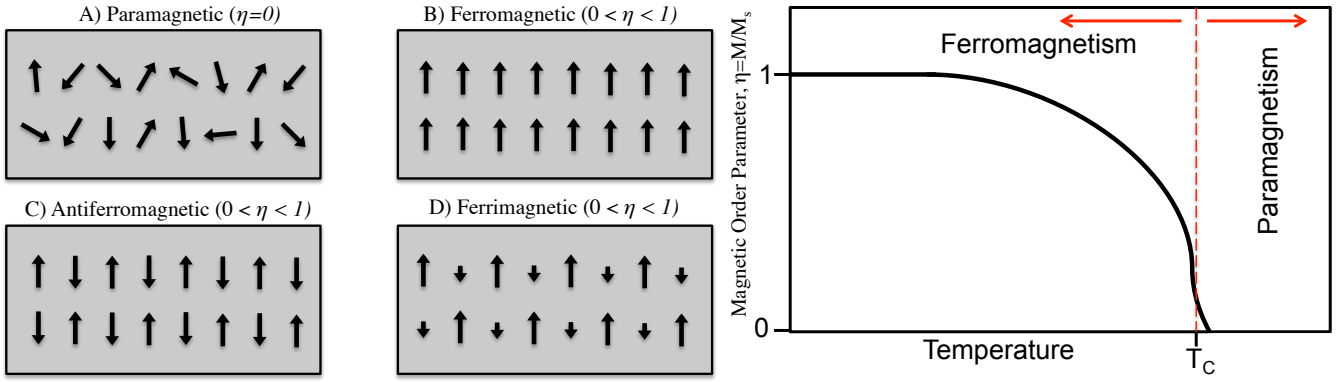

Figure 1.2.2 (left) Schematic illustrating magnetic ordering giving rise to common types of magnetism. (right) Plot of magnetization versus temperature also describes magnetic ordering parameter which becomes zero at a material's Curie Temperature.

Thermodynamically, magnetization, $\boldsymbol{M}$, is what is called the extensive *displacement* variable, which responds to the thermodynamic conjugate intensive *force* variable for magnetism which is the applied magnetic field, $\boldsymbol{H}$. In the same way that a material's entropy, S, or volume, V, responds to their conjugate variables temperature, T, or pressure, P, respectively a magnetic material's magnetization, $\boldsymbol{M}$, responds to the magnetic field, $\boldsymbol{H}$, and contributes to that material's internal energy,

$$dU = TdS\text{-}PdV+HdM+\sum_i \mu_i dN \,. \qquad \text{Eq. 1.2.1}$$

Another useful quantity is a magnetic material's *Induction*, $\boldsymbol{B}=\mu_0(\boldsymbol{H}+\boldsymbol{M})$, a field quantity whose field lines are continuous across the magnetic material interface, and is also used to characterize a magnetic material. The response of a magnetic material's magnetization, $\boldsymbol{M}$, or Inducrtion, B, to an applied magnetic field, $\boldsymbol{H}$, is conveyed by M-H or B-H curves or loops, also referred to as hysteresis loops, that are characteristic of a magnetic material. A schematic hysteresis loop is shown in Fig. 1.2.3 and several features of the curve are particularly worth noting.

As the applied field increases the magnetization of the material also increases until it cannot increase any more. This maximum of the magnetization is referred to as the *Saturation Induction,* B_S, (or *Saturation Magnetization*, M_S) and corresponds to the point in which all atom's magnetic moments are all aligned in the same direction.' Upon beginning to decrease the applied field back to zero after saturating a magnetic material energy is stored within the material as magnetic moments prefer to remain aligned and the material magnetized. The induction (or magnetization) of the material when the applied field reaches zero after being saturated is referred to as the *Remnant Induction,* B_R, (or *Remnant Magnetization,* M_R) and is a measure of this stored energy. A more common metric of measuring the amount of energy stored within a magnetized material is the *Coercive Field,* H_C. This is the value of the magnetic field, applied in the direction antiparallel to magnetization, required to return a saturated magnetic material's induction (or magnetization) back to zero.

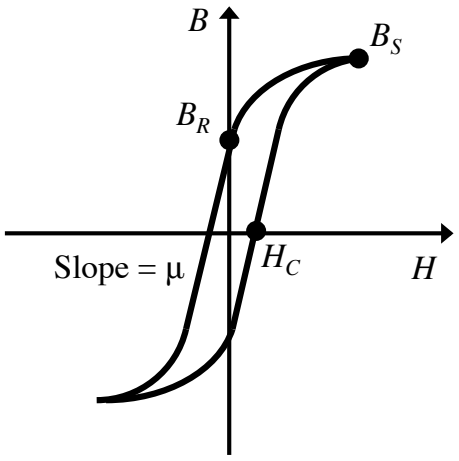

Figure 1.2.3 A schematic hysteresis loop of magnetic induction, B, versus field, H, showing Saturation Induction, B_S, Coercive Field, H_C, and magnetic permeability, μ.

Another material property of interest that is readily extracted from the hysteresis loop is a material's *magnetic permeability*, μ. (Unlike magnetic moment, $\vec{\mu}$, magnetic permeability, μ, is a scalar quantity.) Permeability is a measure of how easily a material magnetizes in response to an applied magnetic field. As such, it is defined as the slope, $\mu = \frac{dB}{dH}$, of the B-H curve. As illustrated in Fig. 1.2.3 the permeability of magnetic materials is typically linear at small applied fields, this behavior is indicative of magnetic switching via domain wall motion. At larger fields and as the material approaches saturation the permeability begins to decrease and the B-H is no longer linear. This behavior corresponds to the higher energy magnetic switching via the rotation of magnetic moments as will be discussed later in this chapter. As will also be noted later in this chapter, the area under the B-H defines the *hysteresis losses* associated with cycling a magnetic material through a complete magnetic switching loop.

1.2.1 Hard Magnetic Materials

With regard to Fig. 1.2.3 hard magnetic materials are those that exhibit large hysteretic behavior upon magnetic switching, maintain large remnant magnetization after being saturated, and that exhibit large coercive fields required to return the material's induction back to zero. Therein, hard magnets are also commonly referred to as permanent magnets (PMs), because their magnetization remains 'permanently' even after the magnetizing field is removed. Thus, a saturated permanent magnet stores energy as it is magnetized in an amount equal to $M_s H_c$, the so called "*energy product,*" and common figure of merit for hard magnetic materials.

The coercivity and energy product of several of the most common hard magnetic materials are shown in Fig. 1.2.4(left)[2]. Figure 1.2.4(right) shows the coecivity and saturation magnetization for several hard magnets as well, along with the years in which they were developed[2]. Note that the largest energy products belong to a class of magnetic developed since the 1960's, the so-called "Rare Earth" (RE) permanent magnets - FeNdB and SmCo. These magnets have been commercialized since the 1980's and 1990's but the cost of these materials is high and volatile due to the scarcity of the rare earth elements – the 15 lanthanides - for which they are named.

Most of the discussion of hard magnets, particularly rare earth PMs, in this document is in attempt to minimize their usage. This can be accomplished by noting that while the energy product of the RE PMs is

unparalleled, the saturation magnetization of several materials, including amorphous and nanocomposite soft magnets, is comparable or higher than FeNdB or SmCo. In this way, in some applications that require high energy product PMs we can reduce the amount of expensive RE PMs used by instead using a combination PMs and soft magnetic materials of equal or greater saturation magnetization.

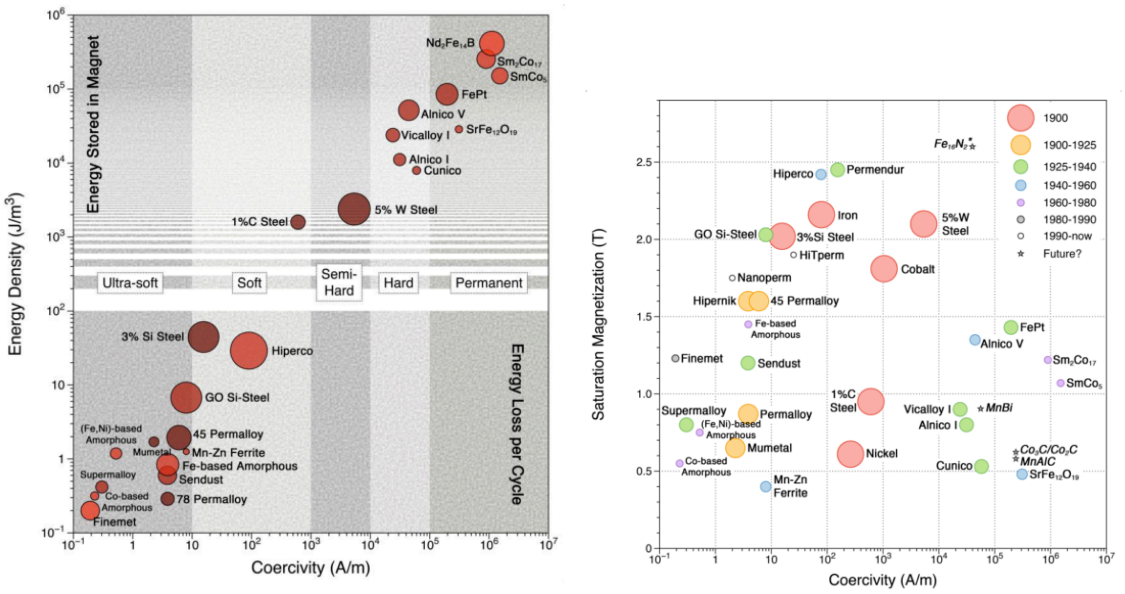

Figure 1.2.4 (left) Combined plot of energy product and energy loss per cycle versus coercivity in hard and soft magnetic materials. (right) Saturation magnetization versus coercivity for common magnetic materials and indication of the years of development.

1.2.2 Soft Magnetic Materials

In contrast to hard magnetic materials, soft magnetic materials exhibit very little hysteresis in the B-H or M-H curves, very small remnant magnetizations, and also very low coercive fields. In this way, soft magnetic materials can be easily switched to and from anti-parrallel magnetic states with a relatively small applied field. As noted earlier, soft magnetic materials can still exhibit very large saturation magnetizations however.

As a soft magnetic material is switched between anti-parallel magnetic states it exhibits energy losses per cycle, as noted previously, equal in energy to the area enclosed by its B-H hysteresis loop. That is,

$$E_{hyst} = \oint H\, dB\,, \qquad \text{Eq. 1.2.2}$$

and we refer to these energy losses as *Hysteresis Losses*.

Magnetic hysteresis losses are largely determined by switching mechanism. In general, magnetic materials switch first (at lowest energies or applied fields) by domain wall motion and later (at higher applied

fields) by rotation of magnetic dipole moments themselves. These switching processes can be controlled however for instance by imparting anisotropy in a magnetic material.

As will become particularly relevant in subsequent chapters I will also introduce now two of the other most prominent sources of losses incurred during the switching of magnetic materials. The total power losses incurred in a soft magnetic material during high frequency switching have contributions from1) Hysteresis Losses, there are 2) Eddy Current losses, and 3) Anomalous Eddy Current Losses. Summing the three terms produces,

$$P_L = P_{hyst} + P_{eddy} + P_{anam} \qquad \text{Eq. 1.2.3)}$$

As noted earlier hysteretic losses are defined as the area enclosed by the hysteresis loop, A_{hyst}, and as such are incurred with every switching cycle. Then, expressed as power losses as a function of switching frequency,

f, we see that hysteretic losses are proportional to or linear with switching frequency,

$$P_{hyst} = f \oint H\, dB = A_{hyst} f \ . \qquad \text{Eq. 1.2.4}$$

Another source of power losses associated with magnetic switching in soft magnetic materials is *Eddy Current Losses,* or 'conventional' eddy current losses if further precision is desired. These losses are illustrated in Fig. 1.2.5 (left) and are resultant of the changing magnetic flux with the magnetic material itself incurred when magnetic materials switch by the low energy, domain wall motion mechanism. By Lorenz' law of induction, the changing magnetic flux induces a current to flow within the area of domain wall motion, these are the so-called 'eddy currents.' These losses have been demonstrated to be related to the switching induction, B, and the geometry and electrical properties of the soft magnetic material – depth, d, perpendicular the flux change and electrical resistivity, ϱ, - and the switching frequency, f, as follows:

$$P_{eddy} = \frac{d^2 B^2 f^2}{\rho} \ . \qquad \text{Eq. 1.2.5}$$

The squared dependence on switching frequency makes eddy current losses particularly restrictive at large frequencies.

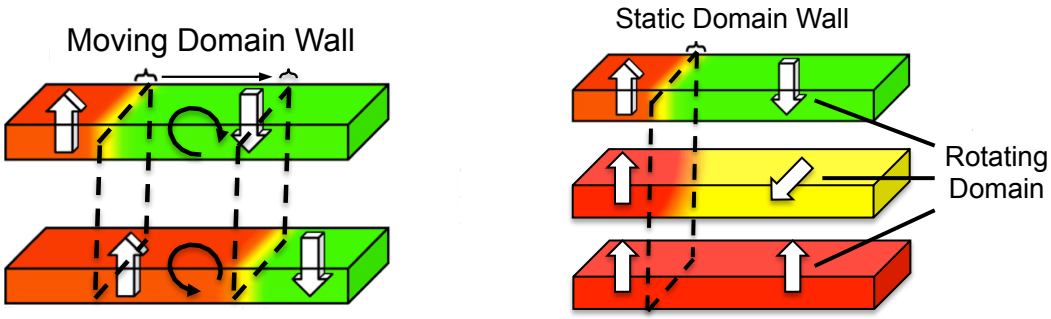

Figure 1.2.5 (left) Magnetic switching via low energy, domain wall motion results in 'conventional' eddy current losses which scale with the square are switching frequency. (right) Magnetic switching via the higher energy, domain rotation mechanism incurs anomalous eddy current losses which scale with *less* than the square of frequency.

Finally, the last power loss contribution results from magnetic switching that occurs via the higher energy, domain rotation mechanism, and is illustrated in Fig. 1.2.5 (right). These losses are also incurred as eddy currents induced due to the changing magnetic flux within the soft magnetic material that accompanies magnetic switching, however due to the domain rotation instead of domain wall motion. These eddy currents are related to the orthogonal depth, electrical resistivity, and switching frequency via,

$$P_{anam} = \frac{df^{x}}{\rho}, \qquad \text{Eq. 1.2.6}$$

where $1<x<2$.

1.3 Amorphous and Nanocomposite Materials

As can be seen in Fig. 1.2.4, two important classes of soft magnetic materials that exhibits very low losses per cycle and very high saturation magnetization are amorphous alloys and nanocomposite alloys, collectively magnetic amorphous and nanocomposite (MANC) materials. These materials have been developed largely over the past 30 years and are now in the process of becoming commercially available.

1.3.1 Synthesis of Amorphous Materials

The amorphous metals studied here are synthesized by the rapid solidification, either melt-spin or planar-flow casting, of a glass forming alloy composition. Glass forming compositions are identified by alloys with deep eutectics and further employ the so-called *confusion* principle so that atoms have insufficient time to move into lattice positions in crystal structures that are too complicated to form in the available time. Inoue's three empirical rules for glass formability are also exceedingly helpful in guiding alloy selection:[3]

1) Multi-component alloy usually consisting of *at least three* constituents.
2) Constituents chosen that have large, negative enthalpies of mixing, so as to ensure mutual dissolution.
3) Constituent elements significantly vary in atomic radius, i.e. large, medium, and small radii elements, so that inter-diffusion is slow and to prevent structural ordering.

In both planar-flow and melt-spin casting techniques an alloy is melted, often by means of RF induction coils, before being rapidly expelled onto a quickly spinning wheel. The wheel is engineered to have very high thermal conductivity so as to allow heat from the melt to rapidly dissipate through the wheel and in so doing rapidly quench the ribbon. Wheels can either be actively cooled or simply have enough thermal mass to be unaffected by a small amount of hot ribbon. Partially devitrifying, or crystallizing, an amorphous precursor by thermal treatment thereafter forms Nanocomposites.

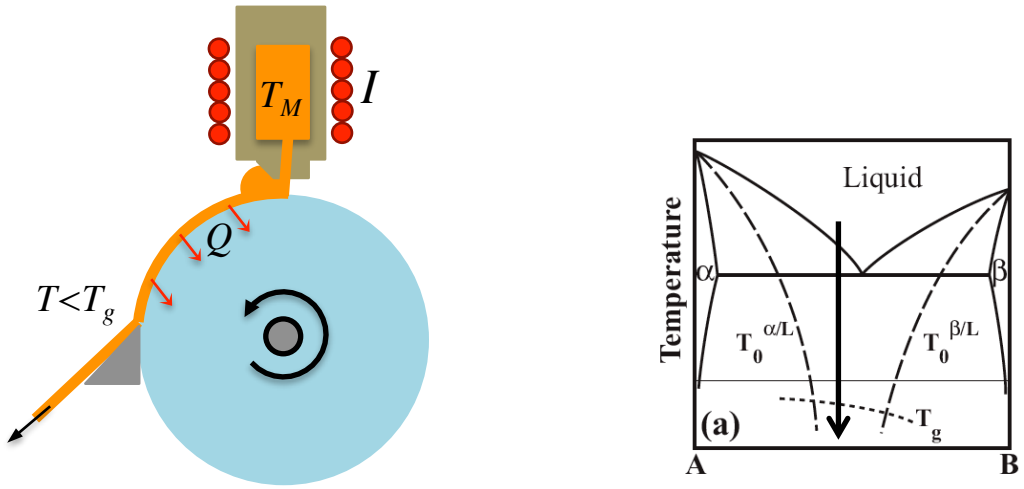

Figure 1.3.1 (left) Schematic of the planar flow casting rapid solidification synthesis technique used to procure amorphous ribbon. (right) Schematic deep eutectic binary phase diagram illustrating the necessity to quench below T_g while remaining above T_0, constructed by equating the Gibbs free energy of the liquid and crystalline phases, in order to achieve a metallic glass.

As rapid solidification techniques such as planar-flow casting (PFC) have been continually improved throughout the developmental history of amorphous and nanocomposite materials this synthesis technique is now very mature. Laboratory and even industrial sized PFC apparatuses are now commercially available. Many amorphous alloys can be continuously produced by the kilogram. However, a readily modifiable caster is conducive to the development of new alloys.

1.3.2 The Random Anisotropy Model

The high permeabilities and low coercivities of both amorphous and nanocomposite materials stems from the disordered atomic structure of the amorphous phase. Unlike crystalline magnetic materials that exhibit *magnetocrystalline* anisotropy because there are no preferred, crystallographic directions in the amorphous phase these materials do not exhibit magnetocrystalline anisotropy and are thus extremely magnetically soft. Nanocomposite materials maintain their magnetic softness despite possessing crystalline particles embedded in an amorphous phase because of collective cancellation of magnetocrystalline anisotropy described by Herzer in the *random anisotropy model*[4].

Magnetic anisotropy, the property of a magnetic material being easier to magnetize in one direction (or a few related directions) than in others is quantified by the anisotropy constant,

$$K_u = \frac{1}{2}\mu_0 H_a M_s \qquad \text{Eq. 1.3.1}$$

where M_s is the saturation magnetization of the material and H_a is the *anisotropy field*, the field required to saturate the material in a hard direction. When considering a crystalline magnetic material the magnetocrystalline anisotropy constant which describes the directional preference simply due to the symmetry of the crystal lattice itself can be as large as $10^4 J/m^3$ ($K_1=4.7x10^4 J/m^3$ for Iron). Despite the large source of anisotropy from crystal structure, because of the RAM nanocomposite materials can have anisotropy constants as low as amorphous materials, $K_u<60 J/m^3$ for Finement. How does the RAM accomplish this?

Because both the primary crystalline phases and the amorphous matrix are ferromagnetic, nanocrystals are not isolated from each other but are instead coupled through the ferromagnetic amorphous matrix over an exchange length, L_{ex}. As shown in Fig. 1.3.2, as crystal size, D, drops below this characteristic exchange length and many crystals, $N>10^2$, occupy an exchange volume because the crystals are randomly oriented their magnetocrystalline anisotropy averages over this exchange volume, and the resultant *average* magnetocrystalline anisotropy constant varies with grain size as,

$$\langle K_1 \rangle = K_1 (D / L_{Ex})^6 . \qquad \text{Eq. 1.3.1}$$

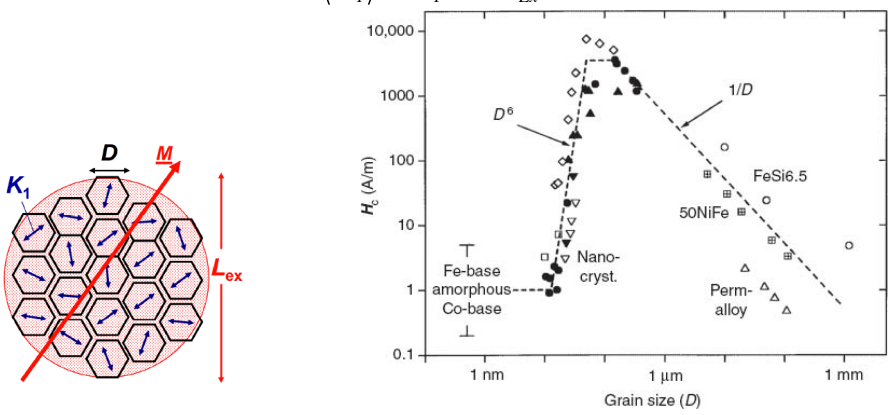

Figure 1.3.2 (left) RAM schematic showing the magnetocrystalline averaging resulting from many randomly oriented crystal grains being coupled within an exchange volume determined by L_{Ex}. (right) The D^6 power dependence predicted by Eq. 1.3.1 observed in nanocrystalline alloys[4].

Additional sources of anisotropy are present and/or can be induced in MANC's and contribute to the overall anisotropy of the material. Some examples include pair ordering, which can be induced by crystallizing in an applied magnetic field, or anisotropy resultant from applying uniaxial stress, σ, to a material as in strain annealing or even rolling.

1.3.3 Crystallization Theory in MANCs

Nanocomposite materials are produced through devitrification of an amorphous precursor, a process that is described well through conventional nucleation and growth and JMAK theory. Nucleation of crystals in amorphous metals can be accurately described using the same first order transformation constructs of, for instance, the solidification of a liquid. By considering the change in Gibbs free energy of the precipitate and precursor phases,

$$\Delta G = V_{nuc}\Delta G_V + SA_{nuc}\gamma_{\text{int}} + SW \text{ ,} \qquad \text{Eq. 1.3.2}$$

- with contributions from the enthalpy of formation, interfacial energy, and any other contribution (like internal strain) - a critical nuclei radius, r*, and energy barrier, G*, can be derived. These barriers are almost always decreased when heterogeneous nucleation occurs, for instance due to wetting or when low interfacial energy interfaces are available.

After nucleation, growth, G, of nuclei occurs by

$$G \propto e^{-\frac{Q_f}{kT}} e^{-\frac{\Delta G_{A\to B}}{kT}} \qquad \text{Eq. 1.3.3}$$

in which two regimes can be identified:

1) small undercooling: in which the driving force, $\Delta G_{A\to B}$, is small so $G \propto \Delta T$, or
2) large undercooling: in which the formation energy barrier, Q_f, and low temperature limits the growth rate.

The crystallization of amorphous metals discussed in this report occurs in the large undercooling regime because the amorphous liquid is not a molten liquid in equilibrium, but is instead is a liquid that has been frozen into a metastable solid amorphous state. In this way crystallization proceeds by raising the temperature of the "frozen" amorphous precursor, instead of cooling a liquid amorphous one. In this regime growth is limited by atomic mobility. This temperature limited growth is apparent on a TTT diagram, a tool commonly used to describe the kinetics of transformation.

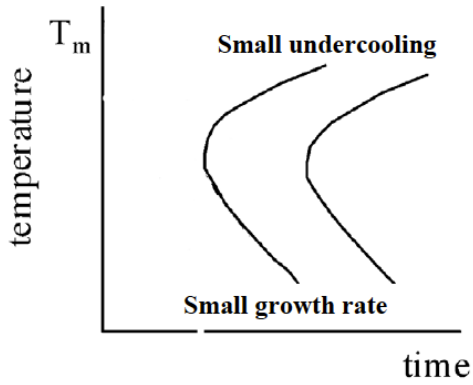

Figure 1.3.3: Schematic of a TTT diagram illustrating the large and small undercooling limits of a nucleation and growth transformation.

As a thermally activated process crystallization obeys an Arrhenius equation in which the growth rate,

$$k = k_0 e^{\frac{-Q^*}{RT}} \qquad \text{Eq. 1.3.4}$$

where RT is the thermal energy, Q^* is the thermal activation energy of the crystallization process, and k_0 is a growth constant. The fraction of a sample crystallized as a function of time is then expressed,

$$X(t) = 1 - e^{-(kt)^n}, \qquad \text{Eq. 1.3.5}$$

in which n is the Avromi time exponent. The Avrami exponent,

$$n = p + q, \qquad \text{Eq. 1.3.6}$$

indicates the nucleation, through p, and growth, through q, mechanisms. For diffusion controlled, three-dimensional growth in which most all nucleation has occurred by t=0, which is the case for most MANCs, p=0 and q=n=3/2.

For crystallization events which transition, from first proceeding by one mechanism to then proceeding by another, the Avrami exponent similarly takes continuous values. Such is the case observed for primary crystallization in the FINMENT system as studied by Pradell et al [5]. This experimental and theoretical treatment of the Avrami exponent begins with interfacial growth for which n=1. Early in crystallization (at small crystal fractions) the diffusion of large glass forming elements begins to limit crystal growth and for a period n takes approximately 3/2. However, by the late stages of growth Pradell describes by the 'soft impingement' mechanism that diffusion profiles of neighboring crystallites begin to overlap and n approaches 0 as crystal growth ceases.

Activation energies for crystallization events can be determined by Kissinger analysis, in which alloys are crystallized under various constant heating rates, ϕ, and the temperature at which peak crystal growth is

achieved, T_P, is recorded, for instance by monitoring heat evolved as in Differential Scanning Calorimetry (DSC). In this scheme, $\ln(\phi/T_P)$ is plotted versus $1/T_p$ so that a linear fit of the re-ordered growth equation,

$$\ln\left(\frac{\phi}{T_P^2}\right) = -\frac{Q^*}{RT_P} + const \qquad \text{Eq. 1.3.7}$$

can be fit to yield the activation energy, Q^*.

1.3.4 Fe, Co, and FeCo based MANCs

The magnetic metal base (Fe, Co, or FeCo) primarily determines many of the magnetic properties of MANCs. A brief review of MANCs from this perspective is summarized in table 1.3.1 and is discussed here.

	Saturation Induction, B_s [T]	Relative Permeability (μ/μ_0)	Curie Temp, T_C (amorphous) [C]	Primary Crystalline Phase(s)
Fe-based	1.2-1.5[6]	10^3-10^5[7]	350-570	BCC
Co-based	1-1.3[8]	10-10^4[8]	625-925[9]	BCC, HCP, FCC [10]
Fe-Co based	1-1.85T[11]	10^2-10^4[11]	210-600C[12], [13]	BCC, FCC[10]

Table 1.3.1: Trends and characteristic advantages of Fe, Co, and FeCo based MANC alloys give each niche applications.

Fe-Co based alloys exhibit the highest Saturation Induction, B_s, of the MANCs, and are used in applications that require such. The Slater-Pauling curve, Fig. 1.3.4, can be used to predict an alloy's saturation magnetization, or concomitant saturation induction, B_s. The atomic dipole moment stems from unpaired electrons in the d-shell of the atom. While the occupation of orbitals is fixed for elemental atoms, by alloying a continuous occupation number of the d-shell can be achieved. It is noted that the peak of the Slater-Pauling curve occurs in an Fe-Co alloy. The maximum in saturation induction at Fe:Co=65:35 experimentally observed in MANCs occurs because of this and considerations of the Bethe-Slater curve relating exchange strength with alloying.

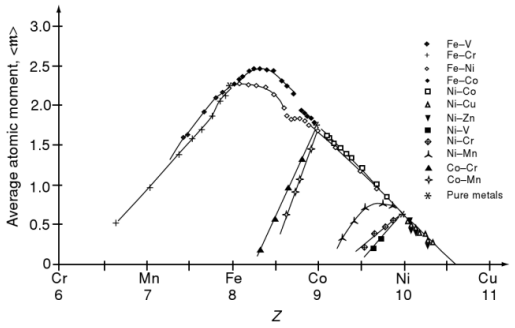

Figure 1.3.4 The Slater-Pauling curve relates atomic moment to electron occupancy, Z, in magnetic alloys, and predicts a maximum saturation magnetization in Fe-Co alloys.

Phase selection is another important trait of MANCs that can affect several properties including induced anisotropy, effective magnetostriction, and ultimately power losses and performance in device applications. The equilibrium Fe-Co phase diagram can be used as a guide in predicting phase selection in Fe, Co, and FeCo based MANCs. As the equilibrium diagram suggests the disordered bcc, α-Fe(Co) phase is the primary, first, crystal phase to form upon annealing the amorphous precursor in not only Fe-based MANC alloys, but also into the FeCo alloys. The ordered fcc, γ-FeCo phase, and eventually hexagonal, ε-Co, forms in Co-basec alloys[14]. However, even into Co-based alloys with Fe:Co<10:90 prefernce for bcc crystal formation has been observed[10]. Reasons for preferential bcc nucleation include reduced amorphous/bcc interfacial and/or strain energies compared to closed packed nuclei and glass formers, such as Nb, Ze, B, acting to stabilize the bcc phase[10].

Largely in keeping with phase selection in these alloys Curie Temperature, T_C, tends to increase with decreasing Fe:Co ratio, with Co-based alloys exhibiting the largest magnetic thermal stability. However, T_C is very sensitive to alloying with none-magnetic elements such as glass formers. Similarly, induced anisotropy, which can be indicated through a material's relative permeability, tends to increase in more Co-rich alloys. In intermediate Fe:Co ratios this is due to pair ordering in the crystalline phase. Anisotropy induced through strain annealing has been related to magnetostriction and residual stresses locked into the crystalline/amorphous compsite structure[15]. However, in Co-rich alloys even this phenomena cannot explain observed aniostropies as large as K_u=1.89erg/cm^3, and the presence of uniaxial hexagonal phases are suggested to contribute to such[8].

Chapter 2.0 Motivation: Magnetic Materials for Application in Electric Machines

This section summarizes the extremely prevalent use of magnetic materials in electric motor applications. I first motivate the topic of magnetic materials for electric motor applications through an energy usage and efficiency analysis. I then outline the basic function of both soft and hard magnetic materials in motors and then focus on the history and proposed use of amorphous and nanocomposite materials in electric motors. I then report results of computational models demonstrating that reductions in motor size and amount of costly permanent magnetic material can be actualized by incorporating MANCs into hybrid motor design. I close by summarizing the results of a C2M market analysis which identified the industrial and transportation motor markets as standing to benefit the integration of MANCs into electric motors.

This chapter summarizes and contextualizes work that from the following publications:

1) "High speed electric motors based on high performance novel soft magnets." J. Silveyra, A. Leary, V. DeGeorge, S. Simizu, and M. McHenry. *J. Appl. Phys*. Vol 115, 17. (2014).[16]
2) "Amorphous and Nanocomposite Materials for Energy-Efficient Electric Motors." J. Silveyra, P. Xu, V. Keylin, V. Degeorge, A. Leary, and M. McHenry. *Journal of Electronic Materials*. (2015). [17]
3) "Iron-Cobalt Based Magnetic Amorphous Nanocomposites for Smaller, Lighter, More Efficient and More Powerful Electric Motors." A. Chun, D. Hellebusch, P. Hogan, B. Li, D. Liu, C. Reed, V. DeGeorge, A. Leary, and M. McHenry. University of California at Berkeley C2M Final Report. Dec. (2014). [18]

2.1 Electric Motors

In either a discussion of the applications of magnetic materials or of energy usage it is difficult to avoid discussing electric motors. The use of both classes of magnetic materials, hard and soft, in electric machines makes motors the largest end use of magnetic materials.[19] The additional consideration that electric motors are the largest end use of electricity in the US and the world only further motivates this discussion of improving the energy efficiency of electric motors through novel use of magnetic materials.[20]

2.1.1 Energy Considerations

Perhaps the best indicator of the prevalence of electric machines is the gross amount of energy that is consumed by them. Lawrence Livermore National Lab reports, Fig 2.1.1, that in 2011 of the 4.9×10^{20}J of energy produced on earth over a third, 1.9×10^{20}J or 38.8%, is converted into electricity[21]. The primary end use of this electrical power is electric machines, which accounts for 46% of electricity usage, Fig. 2.1.2(a) [20]. That is, 8.7×10^{19}J or nearly a fifth, 17.8%, of all the power generated on earth is used by electric motors! This is more energy than the total amount of energy used for transportation, or more energy than is produced by all renewable sources combined. This general trend holds for the United States as well.

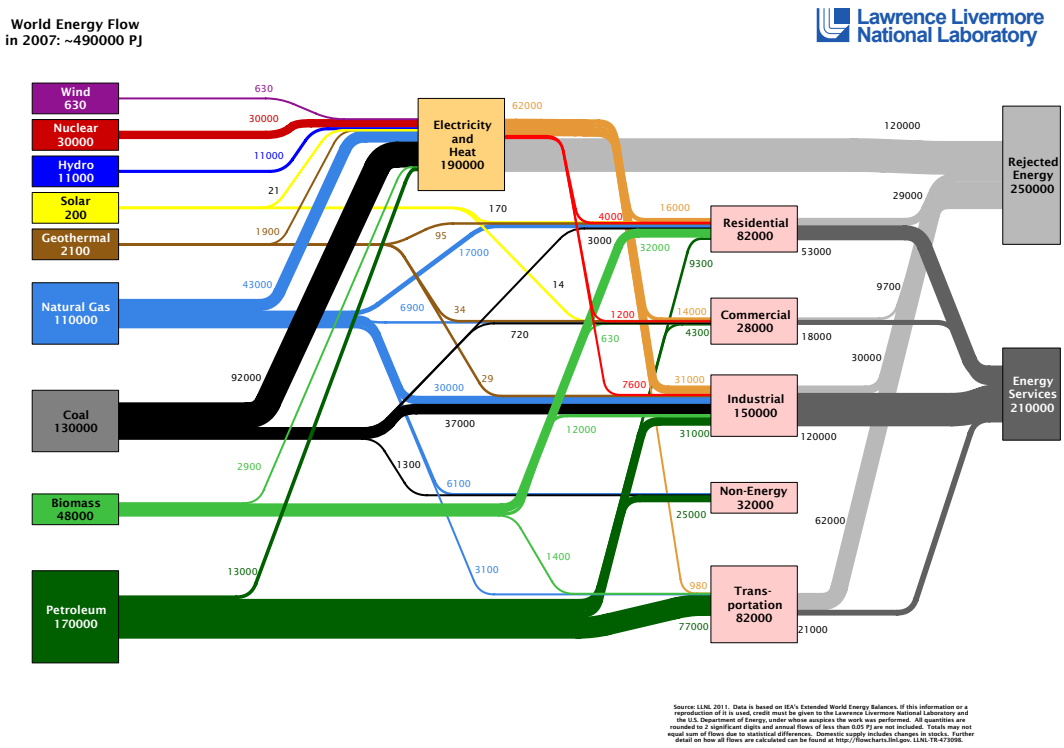

Figure 2.1.1 Schematic chart of world energy generation, by source, to usage, by sector, indicating that where nearly half, 40%, of the energy generated is converted into electrical power, more than half of this electrical power is wasted in energy losses. Trends hold for U.S.[21]

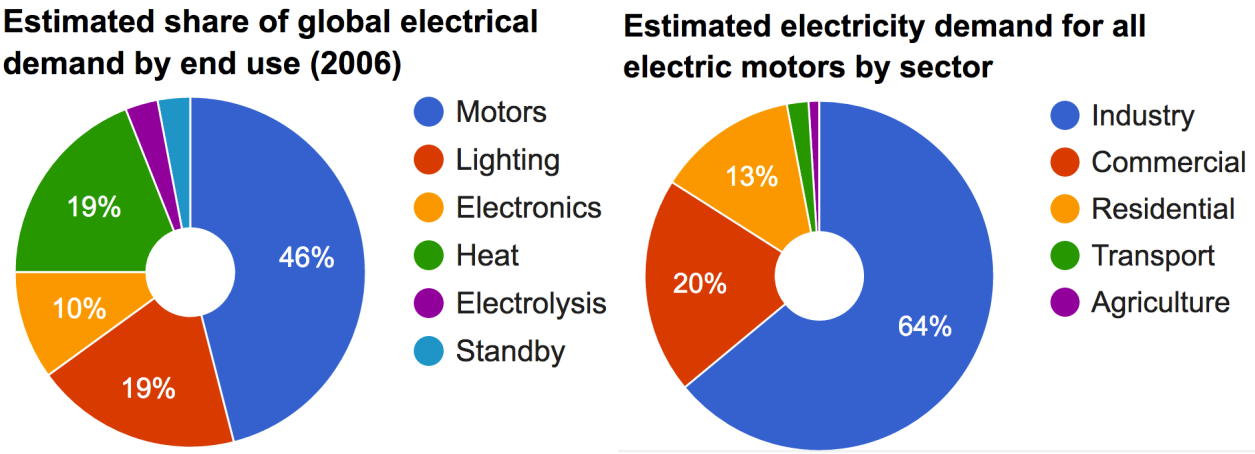

Figure 2.1.2 Of the 1.9×10^{20}J of energy converted into electricity (left) nearly half, 46%, is used by electric motors. The electrical energy used by motors is divided by sector (right) for further context within Fig. 2.1.1. [20]

2.1.2 Electric Motor Operation and Design

Figure 2.1.3 categorically illustrates the most common and general types of electric motors. AC and DC motors are differentiated by the input electrical signal, either alternating or direct current, on which the machines operation. The Squirrel Cage Induction AC motor is by far the most common electric motor by number in use and also by energy usage[20]. All motor topologies employ soft magnetic materials in at least some components, usually inside the coils in the stator. The topologies – Synchronous, Brush and Brushless DC and PPMT - that can also employ permanent magnets (PMs) are indicated as such. Distinction between induction, synchronous, brushed DC, and brushless DC motors requires further background in the basic principles of motor operation beyond the purview of this document. A description of Parallel Path Motor Technology (PPMT) will however be discussed due to its particular advantages with regard to usage of Magnetic and Amorphous Nanocomposites.

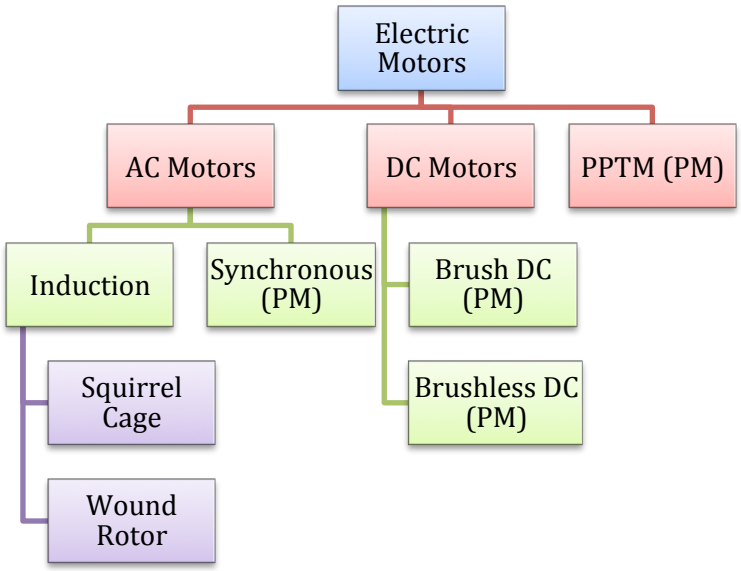

Figure 2.1.3 Schematic categorizing some of the most common classifications of electric motors.

There are two essential components to every electric motor of any topology: the 1) *Stator* and the 2) *Rotor*. In general, the *stator* is the component of the motor which is stationary, which takes in electrical power, and which produces a, usually rotating, magnetic field to be coupled to the rotor. Therein, the *rotor* is the component of the motor that couples (through various means) to the magnetic field produced by the stator. The rotor itself spins or *rotates*, and outputs mechanical power and torque. The means by which a magnetic field is

produced in the stator and couples the rotor is the basis by which motor topologies are differentiated and distinguished.

The stator for most AC machines can be generalized as an array of electromagnets, current carrying coils surrounding a soft magnetic core material, also referred to in motors as *poles*. In Fig. 2.1.2 a six pole radial stator is shown. The soft magnetic material inside the coils is almost always laminated into thin sheets that are stacked together so as to minimize eddy current losses incurred during magnetic switching. The distinction between *radial* and *axial* motors refers to the direction of the magnetic flux set up in the stator and which couples to the rotor. If this flux is radial with respect to the axis of rotation of the motor we call these radial motors, and if it is parallel the axis of rotation we call these axial machines. In the stator of Fig. 2.1.4 electrical current is input through these coils, such that a continuous rotating radial magnetic field is produced.

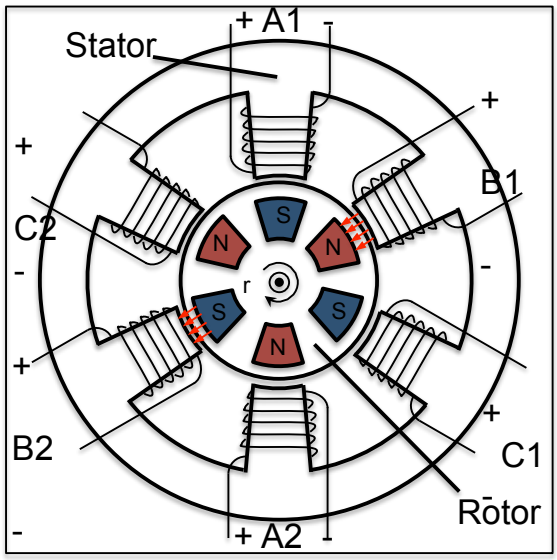

Figure 2.1.4: The stator of most all AC motors consists of several pairs of wire coils which produce a rotating magnetic field to be coupled to the spinning rotor. Soft magnetic material fills the coils amplifying, focusing, and guiding the magnetic field.

The rotating magnetic field produced by the stator can be coupled to the rotor by several means. In a synchronous, usually PM, motor the rotor is simply coupled to this rotating field by the static magnetic field of permanent magnets which are affixed to the rotor. The whole stator configuration then rotates with, or in-"sync" with, the stator's rotating magnetic field.

Squirrel cage induction motors couple to the stator by allowing the stator's rotating magnetic field to *induce* a current to flow in circuits, which collectively look like squirrel cages, built into the rotor. These induced currents in turn produce another magnetic field in the rotor which then couples to the stator and produces torque. Because a magnetic flux change in the circuits of the rotor is required for the rotor's induced

current, and concomitant magnetic field, to be present the rotor of squirrel cage motors must always rotate slower than the rotations of the magnetic field produced by the stator for any torque to be produced. Thus, squirrel cage induction motors are *non-synchronous* machines. This is a unique feature of the squirrel cage induction motor. Moreover, the clever design allows for the rotor to couple to the stator via electromagnetics (in both the rotor and stator) but does so while providing galvanic insulation between the rotor and stator (there are no electrical contact points sliding past one another as in motors with brushes) and while maintaining a rotor free of permanent magnets.

International Efficiency (IE) Standards

The efficiency of electrical motors is defined as the ratio of mechanical output power to electrical input power. In 2008, the International Electrotechnical Commission introduced the precisely defined and open-ended international efficiency-classification scheme using the classifications, IE1-IE4 listed and defined by performance below and in Fig. 2.1.5, to denote the efficiency of motors from least efficient to most efficient.

International Electrotechnical Commission Motor Efficiency Classes:
IE1: Standard Efficiency
IE2: High Efficiency
IE3: Premium Efficiency
IE4: Super Premium Efficiency
[IE5: Unnamed, but introduced by Hitachi in 2015]

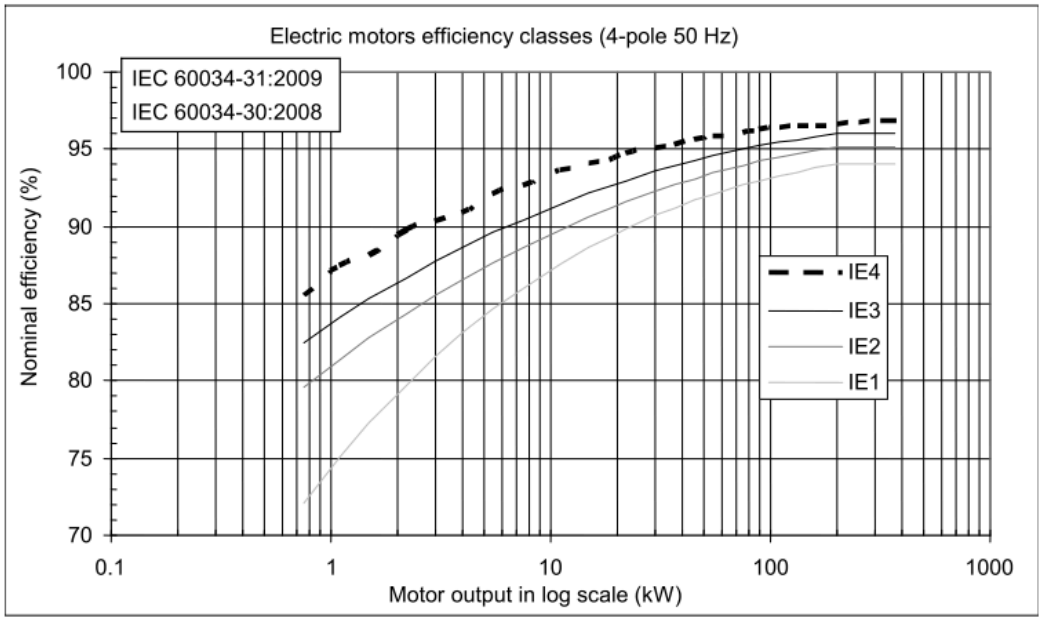

Source: IEC 60034-30 and IEC 60034-31, draft 2009.

Figure 2.1.5 The efficiency classes of standard IE1-IE4 four pole motors based on nominal operating efficiency as a function of output power.

M. Doppelbauer of the International Electrotechnical Commision outlines how the current international standards relate to prior efficiency standards, which historically have spanned a given country, continent, or market. The report also discusses how three phase squirrel cage induction motors, by far the most prevalent motor topology, cannot typically achieve efficiencies higher than IE3, and only with difficulty can achieve IE4 [22].

In 2011 the International Energy Agency issued a working paper report *Energy-Efficiency Policy Opportunities for Electric Motor-Driven System* that was the first global analysis of energy consumption in electric motor-drive systems. The report first assessed the tremendous amount of energy consumed by electric motors and then outlined where the most significant efficiency gains could be actualized. The report found that the most significant losses in induction motors consist of: Stator Losses (30-50%), Rotor Losses (20-25%, and Core Losses (20-25%). Rotor and stator losses correspond to losses incurred in the conductive circuits of the rotor and stator respectively, whereas core losses correspond to those incurred by the magnetic core material during flux switching.

The report also identified and rated areas of motor design that stood to actualize the largest improvements of motor efficiency. The report identified that the components of the induction motor that stood to most improve energy efficiency were as follows, from most impact to smallest impact:

Ranking of Areas of Improvement for Induction Motor Performance[20]

1) Active Material
2) Stator and rotor geometry
3) Temperature level
4) Lamination material
5) Manufacturing tolerances
6) Air gap dimensions
7) Fan efficiency
8) Heat transfer rate

In summarizing these results we note that 5 of the areas of improvement relate to subjects discussed in this project - 3 pertaining to magnetic material and 2 pertaining to motor topology. Areas of improvement #3, 4 and 8 – temperature level, lamination material, and heat transfer rate - are each specifically magnetic material properties limitations. The magnetic material being analyzed in that report is premium electrical Si-Steel.

MANCs demonstrate property benefits over Si-steels in each these categories. The other two areas of improvement pointed out here #2 and # 6 – Stator and rotor geometry and Air gap dimensions – pertain to changes in motor design and topology and hence motivate the next subsection of this report, unconventional motor design. (The "Active Material" in area #1 refers to the conductive induction material of induction motors, i.e. Copper or Aluminum.)

Unconventional Motor Topologies

As their primary applications have remained consistently focused on large industrial and commercial use induction motors have undergone gradual and incremental improvements in design and efficiency over decades, and Si-steel has remained the most prevalent magnetic core material. However, with increased interest in light-weight, higher energy-density electric motors for transportation – not independent from advancements in increased energy density batteries – less conventional designs and materials, including MANCs, are being considered and explored for improved performance in specific and developing applications. Here two such unconventional designs – Axial Motors and Parallel Path Magnetic Technology (PPMT) - are discussed as they lend themselves most to the integration of MANCs into their designs.

Axial Machines

As noted earlier *axial* motors are those in which the changing magnetic flux that couples the stator to the rotor is parallel to the motor's axis of rotation.[23] A schematic of an axial PM motor is shown in Fig 2.1.6. Axial motor topologies are conducive to the incorporation of MANCs because of the orientation of the stator, specifically the stator core. Because MANCs tend to be long and narrow ribbons, instead of sheets as in electrical steel, and tend to be orders of magnitude both thinner and harder than Si-steel laminates there is a preference for winding MANC ribbon concentrically to make a stator core, instead of stamping/cutting and then stacking, as in Si-Steel. This concentric winding lends itself to being wound by the current carrying wires in the same direction and around the wound magnetic core. This arrangement of the current carrying wire and the magnetic wound core produces separate, unconnected pole pieces that, unlike stacked sheets, can be oriented with the winding axis parallel to the axis of rotation of the motor, i.e. axially. Axial motor topologies tend to fill more space in the motor, have more surface area over which flux can be exchanged, and have smaller air gaps

between the rotor and stator. The end result is that axial motors, of which MANCs lend themselves, tend to be more energy dense electrical machines.

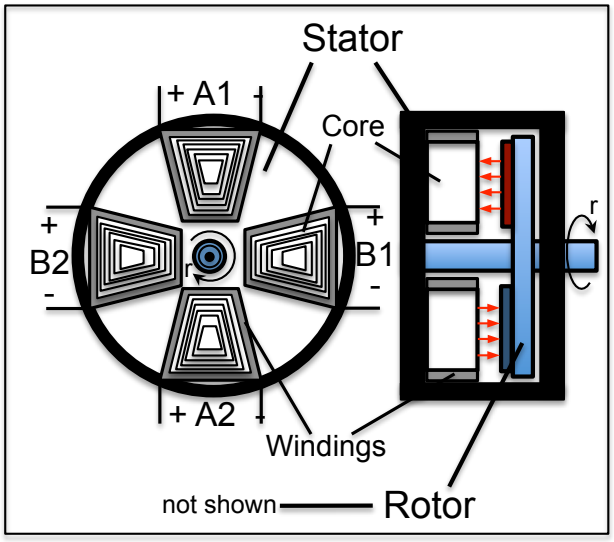

Figure 2.1.6 A schematic of an axial motor showing cutaways of the stator - axial cross-section parallel to *r* - (left) and whole motor assembly – perpendicular to axis of rotation, *r* - (right). Soft magnetic material on the stator is shown in white, current carrying windings are shown in grey, the rotor is designated by light blue, Permanent Magnetics in red and dark blue, and the motor housing is shown in black.

Parallel Path Magnetic Technology (PPMT)

Another unconventional design which the integration of MANCs into motors has generated considerable interest is Parallel Path Magnetic Technology (PPMT). In 2006 C. Flynn released the design for a hybrid magnetic circuit, featuring both PMs and soft magnets, that can be used as electrical machines. The underlying premise behind the design, illustrated in a linear actuator in Fig. 2.1.7, is that the strong permanent magnets are used to provide a large magnetic field. Then, selectively placed electromagnets direct this magnetic field along different paths through a soft magnetic material. Thus, PMs provide the strong magnetic field, and the electromagnets simply direct the field, and in so doing change the force experienced between different legs of the magnetic circuit (which can be used to do mechanical work). Because the electromagnets are not supplying the magnetic field that couples the rotor to the stator but instead are only directing it PPMT is a less energy-intensive motor design. This same principle is at work in the more complicated radial PPMT electric motor design.

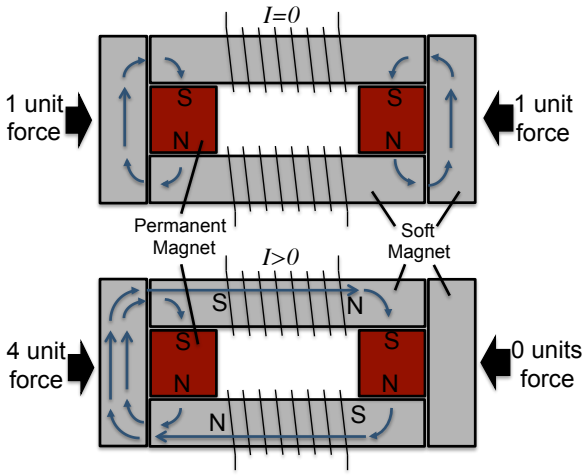

Figure 2.1.7 Schematic of a linear actuator illustrating the operating principle of Parallel Path Magnetic Technology (PPMT). Here permanent magnets, shown in red, produce a strong magnetic field that is directed by electromagnets through carious paths of soft magnetic material to create changing force throughout the magnetic circuit.

2.1.3 Magnetic Materials for Motor Applications

While the principles of magnetism are essential for the operation of all electric motors, soft magnetic materials themselves serve "merely" to improve their operation into practical and operable regimes (this excludes PM motors). Squirrel cage induction motors, the most common electric motors, use only soft magnetic materials for both the stator and rotor. Most all permanent magnetic motors, in addition to using soft magnets in either the stator or rotor, will use exclusively permanent magnets in the other. Hybrid motors usually refer to motor designs that combine the use of both soft and hard magnets in either the stator, or the rotor, or both.

The primary role of soft magnetic materials in electric motors is primarily to amplify, focus, and guide the magnetic field coupling the rotor and stator, much like a ferromagnetic core of a solenoid. In this regard, a high saturation magnetization is important in these devices. A survey of commonly used magnetic materials, both hard and soft, representative of their class of magnetic materials – MANCs, PMs, electrical steel, ferrites, or pure elements – is shown in Fig. 2.1.8.

However, soft magnetic materials are almost always used in this capacity in AC, switching devices so high permeability and low switching losses – usually achieve through high electrical resistivity and thin geometries - are also crucial. Moreover, because motors are almost always multi-pole devices magnetic materials end up switching at frequencies considerably higher than the angular frequency of the rotating stator. In this way it becomes important to be able to switch with low losses at high frequencies and high temperatures

(because losses at high frequency generate considerable heat). The combination of high saturation magnetization, low permeability, and high electrical resistivity are the primary properties that beg MANCs' use in electric motors.

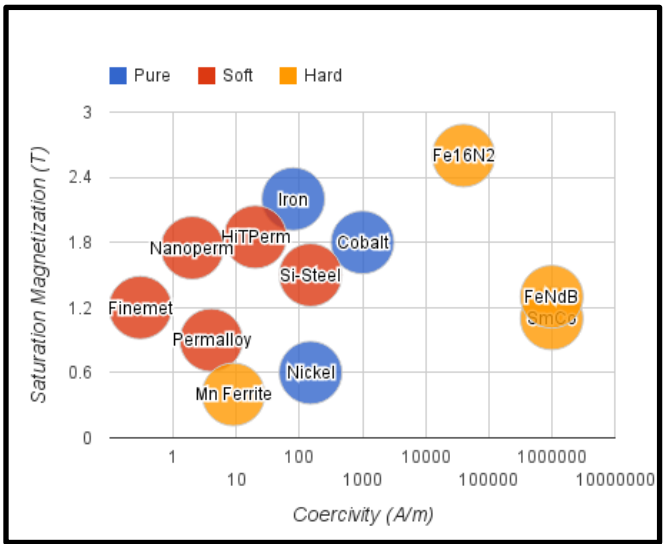

Figure 2.1.8 A properties plot of Saturation Magnetization vs. Coercivity for commonly used magnetic materials shows that the right combination of high B_S and H_C is desired for particular uses in motors.

The development and commercialization of rare earth PMs greatly increased the energy density achievable in electric motors.[24] Using magnetic fields produced from permanent magnets instead of electromagnets eliminates both induction coils and the soft magnetic material that would fill them. This has lead to more simple, more energy dense - though also more expensive electric motors - the net result of which has been the growing prevalence of PM motors particularly in electric vehicle motors.[25]

2.2 Amorphous Magnetic Materials for Electric Motors

In this section I discuss the progress, both historical and ongoing, of integrating amorphous and nanocomposite materials into electric motors.

2.2.1 Prior Work Integrating MANCs into Motors

Baldwin, in 1988, provides an excellent outline of the rise to prominence of electric motors, their technologically quiescent period, and identifies the beginning of a new period of innovation driven by advances in power electronics, and both soft and hard magnetic materials [26]. As noted by Baldwin, with the advent of amorphous soft magnetic materials, FINMET and other Fe-based alloys in the late 1980s and early 90s, their use in electric motors was a logical application. Metglass's FINEMET was first investigated in an electric motor in the 1980's and efforts have continued to today. As noted previously, the combination of high saturation magnetization, extremely low magnetic permeability, and large electrical resistivity readily suggest the use of MANCs in electric motors.

Below is a chronology of some of the key events in the integration of amorphous and nanocomposite materials into motors. I summarize the progress made toward integrating MANCs into electric motors into the following movements:

I) Direct Substitution: 1980-1990:
Direct substitution of Amorphous, Iron-based materials into conventional motor designs.

II) Selective Integration: 1990-2010:
Use of simple, wound, Iron-based amorphous alloys in less conventional motor topologies – PM, Axial, SR, etc. - chosen in consideration of the amorphous material.

III) Complete Design: 2010-Present
2010-present: Use of complex amorphous alloys in complex geometries achieved though advanced processing featured in unconventional motor topologies extensively designed under direct consideration of the unique magnetic material.

History of MANCs in Electric Motors:

1) 1981: First found attempt at incorporating amorphous alloys into electric induction motors: *Test Results on a Low Loss Amorphous Iron Induction Motor*. W. Mischler et. al. IEEE Transactions on Power Apparatus and Systems (1981).
2) 1982: *Application of Low Loss Amorphous Metals in Motors and Transformers*. L. Johnson et. al. IEEE Transactions on Power Apparatus and Systems (1982).
3) 1983: *Utilization of Amorphous Metals in Electric Motors*. L. Johnson. General Electric Company, Corporate research and development for the Oak Ridge National Laboratory operated by Union Carbide Corp for the DOE. (1983).
4) 1989: *Test Results on a Super-High-Speed Amorphous-Iron Reluctance Motor*. T. Fukao et. al. IEEE Trans on Ind. Apps. (1989). [27]
5) 1992: *A Low-Loss Permanent-magnet brushless dc motor Utilizing Tape-Wound Amorphous Iron*. C. Jensen et. al. IEEE Trans. on Ind. Apps. (1992).
6) 1998: *Electric Motor or Generator*. Caamano. US Patent 5731649. (1998).
7) 1999: *Amorphous Metal Stator for a Radial-Flux Electric Motor*. N. DeCristofaro et. al. PCT Application WO 99/6624. (1999).
8) 2002: *Bulk Amorphous metal magnetic components for electric motors*. N. Decristofaro et. al. US Patent 6420813. (2002)
9) 2003: *High frequency electric motor or generator including magnetic cores formed from thin film soft magnetic material*. Caamano. US Patent 6603237. (2003)
10) 2006: *Practical Design and test of High Torque Density/High Frequency Electric Motors*. A. Hirzel. American Society of Navy Engineers, EMTS. (2006) [28]
11) 2006: *Investigation of Axial Field Permanent Magnet Motor Utilizing Amorphous Magnetic Material*. G. Liew. et. al. (2006)
12) 2008: *Test results of an SRM Made from a Layers Block of Heat-Treated Amorphous Alloy*. A. Chiba et. al. IEEE Trans. on Ind. Apps. (2008)
13) 2010: *Development of a Permanent Magnet Motor Utilizing Amorphous Wound Cores*. Z. Wang et. al. IEEE Trans on Magnetics. (2010).
14) 2011: *Development of an Axial Gap Motor With Amorphous Metal Cores*. R. Masaki. et. al. IEEE Trans. Ind. Apps. (2011).[29]
15) 2011: *Application of amorphous alloy in the new energy-efficient electrical motor*. Z. Wang et. al. Applied Mechanics and Materials. (2011).
16) 2011: *Stator used in an electrical motor or generator with low loss magnetic material and method of manufacturing a stator*. PCT/US11/64535. (2011).
17) 2012: Hitachi 11kW, IE4 efficiency motor using amorphous Metglas material.
18) 2014: Hitachi 11kW, IE5 efficiency axial flux motor (Metglas). [30]
19) 2014: Simulation Co-based MANC in PPMT: *High speed electric motors based on high performance novel soft magnets*. J. Silveyra. J. Appl. Phys. (2014).
20) 2015: Waterjet Cut Tapered Amorphous Magnetic Material Core. Kahourzade. Adelaide, Australia. [31]
21) 2015: Simulation and small scale proof of concept, Co-based MANC in PM: *Amorphous and Nanocomposite Materials for Energy Efficient Electric Motors*. J. Silveyra. JEM. (2015)

2.2.2 Engineering Progress and Challenges

The first movement of integrating amorphous and nanocomposite materials into motors began in the 1980's and early 90's as these magnetic materials were being developed. As their unique magnetic properties were being observed and noted as theoretically attractive for motor applications attempts were made to directly substitute the most common and developed amorphous magnetic material of the time, Fe-based alloys like metglas, into convention induction motor designs. L. Johnson's work putting 'low loss amorphous metals' in

electric motors in 1982 and 1983 represent this movement well. Tests were run and performance measured, but rarely were these motors' performance superior to the same motor with the convention soft magnetic material, so these attempts were largely proof of concept. It might be said that efforts were made to make amorphous alloys conform to the motors of the day.

The second movement I characterize lasted from the 1990's and through the early 2010's as amorphous materials became well developed, when their materials properties had been readily identified as beneficial to electric motors, and the unique considerations of these amorphous materials began influencing, not so much motor design, but choice of motor topology. From 1989 to 2006 Fukao, Jensen, DeCristofaro, and Liew integrated wound amorphous iron cores into reluctance, dc brushless, radial flux, and axial PM devices, respectively. While the topology of the motors was chosen with special engineering consideration to amorphous ribbons, in each of these cases prototypes were made using Fe-based amorphous materials.

This period also saw some fruitful results. These efforts began to demonstrate that motors using amorphous materials can achieve superior performance to those using conventional electrical steel, particularly in niche applications like high-speed, or high energy density designs - Fukao and Liew's work represent this well. These efforts also demonstrated that the chief engineering challenge was less the materials properties of the amorphous alloys themselves but more-so processing challenges of how to practically and effective integrate these materials into a working device so as to exploit these superior properties. In this regard we start to see increased interest in processing amorphous materials, represented well by DeCristofaro's work in 1999. In this stage it could be said that motor topology is chosen in order to readily conform with easily achievable amorphous ribbon components.

Efforts to process amorphous materials specifically for application in electric machines lead to what I characterize as the present stage of integrating MANCs in electric motors. In this stage in which development of amorphous and nanocomposite materials is very mature both the magnetic material itself and the design of the motor itself are significantly modified and designed so as to best suit one another. Perhaps the most representative examples of this are Kahourzade's waterjet cut tapered core – in which Fe-based amorphous

ribbon is processed by waterjet cutting so as to best maintain material properties and then wound into a completely novel tapered core with slits accommodating the current carrying windings. J. Silveyra's simulation of Co-based magnetic materials in motors also features a unconventional and highly engineered alloy leveraged in a very unique way in the unconventional PPMT topology. Both of these efforts were made in 2015 and both demonstrate a complete design of electrical machines around the unique properties of amorphous materials.

It is worth noting that in all of the efforts to date all of the prototype and proof of concept motors featured amorphous and not nanocomposite alloys. This decision is driven both out of prevalence of Fe-based, Metglas like material, because these are still the most developed materials, but also because Fe-based nanocomposites lack the mechanical properties required for motor applications. However, considerations of high and extended temperature operation suggest and motivate the use of a more thermally stable material like nanocomposites. What's more, the mechanical prerequisites for electrical motors does seem to rule out Fe-based nanocomposites, while begging further investigation of Co-based alloys with considerably more robust mechanical properties.

2.2.3 FeCo-based and Co-based Alloys in Electric Motors

Two alloys - one FeCo-based and the other Co-based – are reported and discussed in this work within the context of exploring MANCs for application in electric motors. The FeCo-based alloy, $(Fe_{65}C0_{35})_{79.5+X}B_{13}Nb_{4-X}Cu_{1.5}$ and also denoted as HTX002, has been developed specifically for high saturation induction as its Fe/Co ratio is chosen at the peak of the Slater-Pauling Curve. The Glass Formers, B and Nb, and their composition are chosen so as to ensure glass formability, also to optimize saturation induction, and for thermal stability. [11], [32], [33] For these reasons this alloy is being explored in this work. Later in this document this alloy is studied via Atom Probe Tomography while developing the mass balance of Chapter 4,

The other Co-based $Co_{77.2}Fe_{1.4}B_{14}Si_2Nb_4Mn_{1.4}$ alloy, also referred to as HTX005 and one of the HiTperm alloys has been explored as part of ongoing efforts studying Co-based amorphous alloys with particular interest in their magnetic, mechanical, and thermal properties as well as phase evolution. To this end the temperature analysis and TTT diagram of chapter 4 focuses on this material as well as the processing and resultant changes

in properties, specifically anisotropy, of Leary et. al. [34], [35] Additionally, J. Silveyra et. al. include this Co-based alloy in the work simulating the performance amorphous and nanocomposite materials being used in PPMT hybrid motors.[16], [17]

To the end of developing more economic, energy dense electric motors with reduced rare earth PMs a hybrid motor design, featuring Parallel Path Magnetic Technology (PPMT), was modeled by Silveyra [16] et al. This technology reduces the amount of rare earth PMs required by say conventional PM motors by selectively replacing rare earth magnets with highly engineered combinations of rare earth PMs and soft magnetic material. Results of this model showed that by using the Co-based HTX005 MANC instead of commercial Si-steel in a PPMT hybrid motor 70% size reductions and an 85% reduction in the amount of rare earth FeNdB hard magnetic material could be actualized.

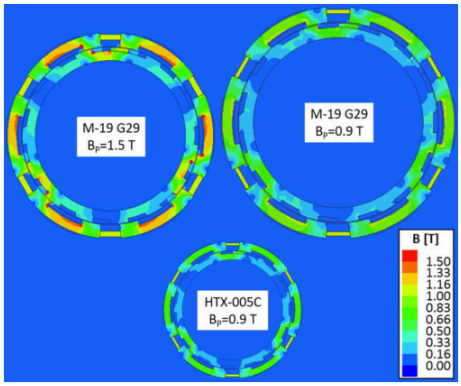

Figure 2.2.1: Results of a model using Co-based MANC materials instead of Si-Steel in a PPMT hybrid motor demonstrated significant reductions in size and the amount of rare earth magnets.[16]

2.3 Market Analysis and C2M Report

Additionally, in the fall of 2014 our group in the MSE department at CMU collaborated with a group from the Haas School of Business at the University of California-Berkeley and completed the Clean Tech to Market (C2M) program. The group from CMU provided technical details of magnetic amorphous and nanocomposite materials and the UCB team used this information to identify strategic advantages and conduct market analysis of applications for MANCs. The market research involved significant interface with and input from professionals in both the electrical transformer and electric motor market, the contacts compiling from such has been maintained as a source of potential partnerships. The final report of the C2M effort has been compiled.[18]

The C2M project identified the 1) increased electrical efficiency, 2) increased power output (both high torque and high speed), and 3) smaller, that is, more energy dense motors as being the strategic advantages of integrating MANCs into electrical motors, over conventional materials. The team also reported industrial and transportation markets as having the most market potential for MANC integrated motors. Within the transportation market both electric vehicles and also an increasingly electrified aircraft/ air transportation market were identified as having potential as the combination of size and efficiency are premium in both markets. Again, more details can be found within the complete C2M report. [18]

Conclusions: Soft Magnetic Amorphous and Nanocomposite Materials for Motors

In all, the 1) superior combination of magnetic, mechanical, and thermal properties, 2) the tremendous energy impact of increased electrical efficiency in electric machines, and 3) the rapidly developing but still significantly unexplored areas of research in amorphous materials in motors pointedly motivate further exploration into integrating MANCs into electric motors. Prominent areas of research include development of novel, unconventional and mutually informed motor design and MANC processing, specifically with respect to the possible advantages of using Co-based nanocomposites over what has become conventional Fe-based amorphous material. Finally niche markets including transportation where size, weight, and efficiency are premium are identified as areas of interest.

Chapter 3 Theses

In Co and Co-Fe based Magnetic and Amorphous Nanocomposite systems in general, and the following compositions in particular:

I) $(Fe_{65}Co_{35})_{79.5-x}B_{13}Si_2Nb_{4-x}Cu_{1.5}$ X={0-4at%} and,

II) $Co_{76-Y}Fe_4TE_YNb_4Si_2B_{14}$ TE={V, Cr, Mn} Y={0-8at%}

the 3d Early Transition (TE) metal Growth Inhibitor (GI) elements - Nb, V, Cr, Mn - and their partitioning during crystallization have the following effects, each with consequences to this material's potential use in electric motors:

1) They correlate crystal state to local GI concentration via a mass balance because of their role in the crystallization processes. And they correlate secondary crystal state to processing and/or operating variables –Time and Temperature – as conveyed through a TTT diagram for secondary. crystallization
2) They increase electrical resistivity - in all the crystal, amorphous, and composite - through the formation and resultant effects of Virtual Bound States (VBS).
3) They relate crystal state to effective nanocomposite resistivity through a multiphase resistivity model accounting for crystalline, amorphous, and interfacial regions, each of distinct GI concentration and corresponding electrical resistivity.

These three effects on thermal stability and electrical resistivity allow for the effective engineering of Co and Co-Fe based MANCs that, together with these materials' magnetic and mechanical properties, make them suitable candidates for use in electric machine device applications.

Chapter 4.0 Chemical Partitioning in MANCs

4.0 Chemical Partitioning

4.0 Chemical Partitioning in Magnetic and Amorphous Nanocomposite Materials

This chapter summarizes chemical partitioning during crystallization of magnetic amorphous nanocomposites(MANCs) and focuses on the high induction, $(Fe_{65}Co_{35})_{79.5-x}B_{13}Si_2Nb_{4-x}Cu_{1.5}$, and Co-based, $Co_{77.2}Fe_{1.4}B_{14}Si_2Nb_4Mn_{1.4}$, alloys. Similar to the tie-line construction of multiphase fields in equilibrium phase diagrams, a mass balance for these non-equilibrium systems is presented for this and similar MANCs which correlates local composition to primary crystal fraction which can aid in structure-properties analysis. Results of a collaboration with Pacific Northwest National Lab in which Atomic Probe Tomography (APT) was conducted on the high induction $(Fe_{65}Co_{35})_{80+x}B_{13}Nb_{4-x}Si_2Cu_1$ alloy is presented which tests the proposed mass balance. The effect of chemical partitioning during primary crystallization on the onset mechanism of secondary crystallization is also explored. And, a TTT (Time Temperature Transformation) diagram for secondary crystallization in the Co-based alloy is also presented and is related to the chemical partitioning of Growth Inhibiting (GI) Glass Former (GF) species. Lastly, I describe how some properties of interest depend on chemical partitioning. This chapter summarizes and contextualizes the original publications:

1) V. Degeorge, A. Devaraj, V. Keylin, J. Cui, and M. E. McHenry, "Mass Balance and Atom Probe Tomography Characterization of," *IEEE Trans. Magn.*, vol. 51, no. 6, 2015. [36]

2) V. DeGeorge, E. Zoghlin, V. Keylin, and M. E. McHenry, "Time temperature transformation diagram for secondary crystal products of Co-based Co-Fe-B-Si-Nb-Mn soft magnetic nanocomposite," *J. Appl. Phys.*, vol. 117, no. 17, p. 17A329, 2015. [35]

The mass balance tying GF concentration to crystal fraction is applicable for any of the GF species that partitions during primary crystallization. Some special cases of the mass balance, like calculation of the final

crystal fraction, are only applicable to the growth limiting species, typically Nb or Zr in FINEMENT and HITPERM. In the HTX005 Co-based system, $Co_{1-x}Nb_xFeTE_yBSi$, $0<x<4$, TE={Mn, Cr, V}, $0<y<8$, the growth limiting species is also Nb.

4.1 Theory and Prior Work

4.1.1 JMAK Kinetics for MANCs

Having established the conventional JMAK kinetics for first order, discontinuous phase transformation in Chapter 1, we now narrow our scope to that of the primary crystallization of amorphous alloys which produces nanocomposites. It is noted again that the primary crystallization events discussed here are between metastable states and not the equilibrium phase transformations JMAK kinetics formally treats. Despite this much of the formalism still applies as is discussed, as well as the adjustments to the conventional kinetic for the treatment of nanocomposites.

The general form of the JMAK equation from Chapter 1, which relates crystal fraction as a function of time, $X_{xtl}(t)$, to the kinetic constant, k, and Avrami exponent, n, applies to crystallization of amorphous alloys[37]–[39]

$$X_{xtl} = 1 - e^{-(kt)^n}. \qquad \text{Eq. 4.1.1}$$

The JMAK equation for crystal fraction has been modified further to more aptly account for two physical considerations of crystal fraction in systems, one pertaining to precipitation and growth transformations generally, and a second more specifically to the MANC system. Early analysis and application of the JMAK equation to first order transformations in metals illustrated the need to consider what has been referred to as the 'extended volume fraction, $\tilde{X}$, which accounts for the overlap between hypothetical crystal particles independently nucleating and growing (as two particles cannot physically occupy the same space). The physically meaningful, 'actual' crystal fraction, X_{xtl}, is thus related to the originally proposed JMAK extended volume fraction, $\tilde{X}$, by,

$$X_{xtl} = 1 - e^{\tilde{X}}. \qquad \text{Eq. 4.1.2}$$

It can be seen that the JMAK formalism's treatment of this consideration is fortuitous in that models which yield a theoretical expression for extended volume fraction, $\tilde{X}(k,n,t) = (kt)^n$, readily lend themselves to the form of the JMAK equation for physical volume fraction.

The second consideration of crystal fraction transformed which applies to the nanocomposite system is that the transformation does not proceed to the full sample volume being transformed, that is at $t = \infty, X_{xtl} \neq 0$. This phenomena is consequence of the underlying mechanisms – the diffusion controlled, soft-impingement mechanism - by which primary crystallization proceeds and more importantly is limited in the nanocomposite system. In this system primary crystallization ceases, and the transformation has proceeded to completion at a final crystal fraction, $X_{f<1}$. When the final crystal fraction, X_f, is known the modification to conventional JMAK kinetics needed to account for this is very straightforward. Eq. 4.1.2 is amended by introducing a reduced crystal fraction, $\hat{X}_{xtl}$, which is simply the crystal fraction of Eq. 4.1.2 scaled by the final crystal fraction, X_f. That is,

$$\hat{X}_{xtl} = X_f X_{xtl} . \qquad \text{Eq. 4.1.3}$$

In this way when primary crystallization has gone to completion and growth has ceased the reduced crystal fraction $\hat{X}_{xtl}(t \to \infty) = 1$, even though the actual crystal fraction of the nanocomposite , $X_f<1$.

Analysis of first order transformations such as precipitation and growth have elucidated that the Avrami exponent is indicative of the nature of both nucleation and growth, i.e. dimensionality and mechanism. Otherwise put, the Avrami exponent has been written as a combination of two terms, p and q, which are associated with nucleation and growth respectively,

$$n=p+q. \qquad \text{Eq. 4.1.4}$$

For instantaneous nucleation in which all nucleation events can be assumed to occur at time, t=0, p=0. If nucleation is better approximated to be constant with time then p=1. The growth term, q, of the Avrami exponent can be related to growth mechanism and growth rate, G=dr/dt for a spherical crystalline particle of radius r, in the following way.

Supposing growth is constant with time, i.e.

$$G = \frac{dr}{dt} = u , \qquad \text{Eq. 4.1.5}$$

yields particle radius, r, as a function of time,

$$r(t)=kt+r^*, \quad \text{Eq. 4.1.6}$$

where r* is the critical nucleus, and an expression for crystal fraction as a function of time,

$$X_{xtl}(t)=\frac{4}{3}\pi(t-r^*)^3. \quad \text{Eq. 4.1.7}$$

Thus, the growth contribution of the Avrami exponent for constant growth, which is the case for interface controlled growth, is q=3. Similarly when we consider a diffusion controlled growth process, as is the case with the devitrification of this class amorphous and nanocomposite alloys, in which the growth rate is proportional to the negative square root of time,

$$G=\frac{dr}{dt}=kt^{-1/2}, \quad \text{Eq. 4.1.8}$$

yields crystal radius and crystal fraction as a function of time,

$$r(t)=2kt^{1/2}+r^*, \quad \text{Eq. 4.1.9}$$

and

$$X_{xtl}(t)=\frac{4}{3}\pi(2kt^{1/2}+r^*)^3=\frac{32}{3}\pi(kt)^{3/2}+r^*. \quad \text{Eq. 4.1.20}$$

Thus for diffusion controlled growth the growth component of the Avrami exponent, q=3/2.

Finally, we consider the theoretical specifics of the soft-impingement mechanism, the diffusion controlled and saturation limited growth process exhibited by this class of MANCs. Conceptually, soft-impingement refers to the specifics of the diffusion controlled growth demonstrated in these nanocomposites during which neighboring particles' glass former diffusion profiles impinge on one another, before the particles themselves come into contact, and in so doing terminate crystal growth as the concentration of the amorphous matrix equilibrates to its peak value, C*. For this reason the large, slow-diffusing species such as Nb and Zr in MANCs are aptly referred to as 'growth inhibitors.'

The soft-impingement formalism established by Pradell et al considers growth that is dependent not only on the diffusion of growth inhibitors, but more specifically on the concentration gradient of growth inhibitors in the amorphous phase[40]. That is,

$$G = \frac{dr}{dt} = \frac{D}{r}\nabla C\,, \qquad \text{Eq. 4.1.11}$$

as is consistent with Fick's second law of mass transport in which C is the growth inhibitor concentration.

The distinct, local concentrations of GIs of the crystalline and amorphous metastable phases are shown in Fig 4.2.2. The GI concentration of the amorphous precursor, C_0, and the crystalline phases, C_{xtl}, are homogenous with the crystalline phase being more depleted of GI than the amorphous precursor, i.e. $C_{xtl}<C_0$. Pradell then asserts that because growth is diffusion limited, instead of interface limited, atoms of the growth inhibiting species will build up on the amorphous side of the crystal/amorphous interface forming a high growth inhibitor concentration 'shell' as local equilibrium is established at the interface. The transformation then continues as GI atoms diffuse away from the interface and into the matrix. Pradell notes that because diffusion is very slow compared to crystal growth, i.e. D<<G, and in keeping with the condition for local equilibrium at the interface the concentration of GIs at this interface, denoted C*, is a constant (further comment on the specific physics of C* is given in subsequent sections).

The last local concentration of GI that Pradell notes is that of the amorphous phase far from the crystal/amorphous interface. This concentration, denoted C_{Am}, is variable and is not constant with time. At the beginning of the transformation, t=0, this concentration of the amorphous phase far from the interface is the same as it is throughout the entire homogenous amorphous precursor, i.e. $C_{Am}^{(t=0)} = C_0$. Even as crystallization proceeds, at its early stages the concentration of GI far from the interface remains equal to that of the precursor even as amorphous phase closer to the interface becomes enriched in GI. At an intermediate stage in crystallization as more GIs are expelled out of the crystal and into the amorphous phase and diffusion profiles of neighboring crystallites begin to overlap with one another this concentration of GI in the amorphous phase far from the interface also begins to increase above C_0. As will be shown in subsequent sections, C_{Am} continues to increase monotonically from C_0 and when crystallization proceeds to completion, at $t = \infty$, C_{Am} approaches its final value, C*. The increase of C_{Am} from C_0 to C* is governed by the mass balance of GI atoms as will be described in the next section. It is worth noting that the final state of the amorphous phase at the completion of primary crystallization is homogenous and the final concentration of this residual amorphous phase is

$C_{Am}^{(t=\infty)} = C*$, and this is the same concentration of the amorphous 'shell' adjacent the interface and which has established local equilibrium with the crystal since the beginning of the transformation.

In this way Eq. 4.1.XI can be further expressed in terms of these local concentrations,

$$G = \frac{dr}{dt} = \frac{D}{r}\left(\frac{C* - C_{Am}}{C_0 - C_{xtl}}\right). \qquad \text{Eq. 4.1.12}$$

We note that then the crystalline radius, r, the concentration of GI far from the interface, C_{Am}, and consequently the concentration gradient are each functions of time,

$$\begin{aligned} G(t) &= \frac{dr}{dt} = \frac{D}{r(t)}\nabla C(t) \\ &= \frac{D}{r(r)}\left(\frac{C* - C_{Am}(t)}{C_0 - C_{xtl}}\right) \end{aligned} \qquad \text{Eq. 4.1.13}$$

And, as we will see r(t) is related to $C_{Am}(t)$ through the mass balance such that the growth rate is also not constant, but is too a function of time.

Examination of Eq. 4.1.XIII yields the expected end behavior of growth proceeding according to the soft-impingement mechanism. We note that because C_{Am} and r monotonically increase and $C_0 \le C_{Am} \le C*$, the concentration gradient will be greatest at t=0 and early stages of crystallization. We also note that as the transformation nears completion at long times, as $C_{Am} \rightarrow C*$ the gradient approaches zero, $\nabla C(t \to \infty) = \left(\frac{C* - C_{Am}^{t\to\infty}}{C_0 - C_{xtl}}\right) \to 0$, as the numerator vanishes and hence the growth rate consequently also goes to zero, as is expected by the soft impingement model.

Pradell et al develops the ensuing kinetics and time variant Avrami exponent for which this soft-impingement formalism results. Their formalism is described to this point so as to both familiarize the reader with the well established kinetics governing this nanocomposite system, and to introduce the necessary parameters – like the local growth inhibitor concentrations - that will be used in the subsequent sections.

4.1.2 Atom Probe Tomography Characterization of MANCs

Atom Probe Tomography(APT) is a powerful experimental technique that elucidates both the spatial and chemical character of metals, semiconductors, oxides, and increasingly soft materials[2], [10], [41]–[43]. Unlike microscopy techniques which produce two-dimensional images of samples, and like other tomography techniques APT produces a three-dimensional reconstruction of the samples being characterized. The spatial resolution of APT can be on the same scale at TEM, 10^{-9}m, but the technique is most commonly operated with resolution comparable to SEM, 10^{-8}m[44]. However, unlike TEM and high resolution SEM, APT characterizes much larger sample volume, ~$10^{2\text{-}3}$nm^3, as opposed to 10nm^2 sample areas for TEM. Moreover, unlike SEM or TEM APT is a destructive characterization technique.

A schematic of the Atom Probe Tomography technique is shown below in Fig. 4.1.1. APT produces three-dimensional spatial and chemical maps of samples by ablating and collecting samples atom by atom. Samples' atoms are ablated by locally exceeding the material's work function by exposure to either a pulsed focused ion beam, or a pulsed high-energy laser. The sample being measured is kept at ground potential, and as sample ions are removed they are accelerated a known distance through a known electric field after which they are collected by an area ion detector. Because the accelerating potential, times of ablation and detection, and the relevant distances (on the area detector and from the sample) are known time-of-flight measurements can be done on each detected ion. In this way each detected atom's initial spatial position within the sample and ion charge, which indicates chemical species can be back-calculated and the sample is reconstructed into a high resolution 3-D chemical map.

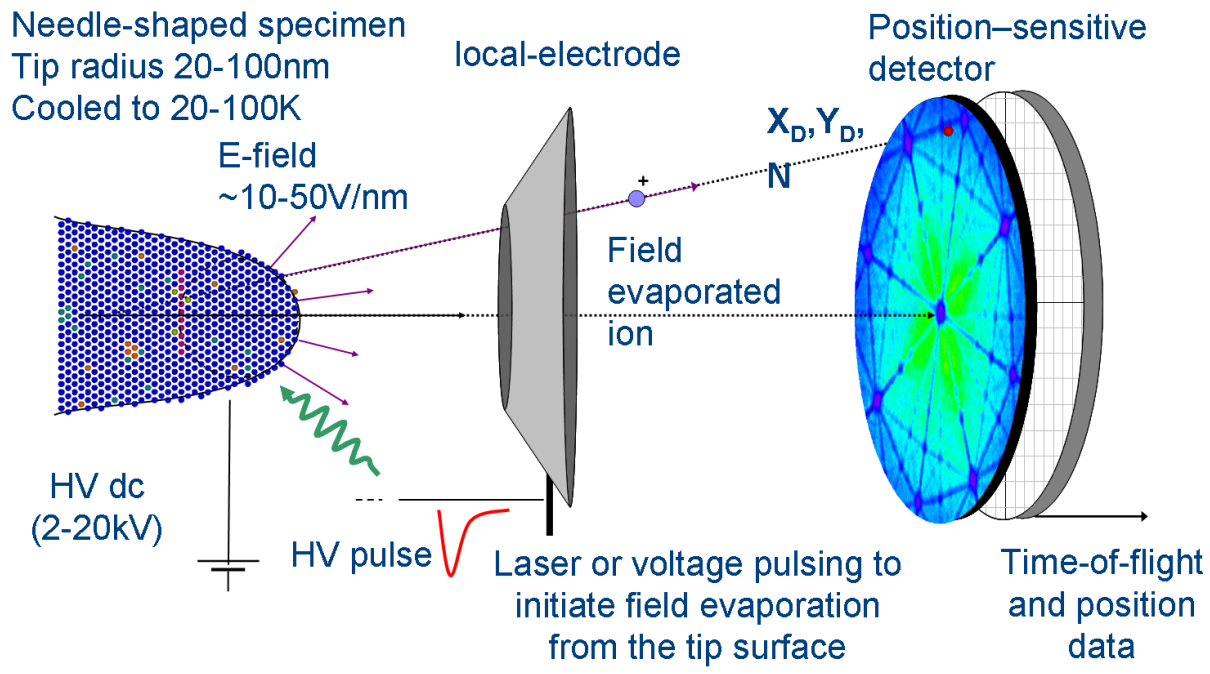

Figure 4.1.1 A schematic of the process by which atoms are (from left to right) ablated off of a sample, accelerated through a potential field, and collected by an area ion detector after which processing software compiles the information and produces a representative 3-D chemical map reconstruction of the sample[45].

In practice, only about 30% of a sample's atoms are spatial and chemically resolved after having been ablated, accelerated, and detected. Grating, masks, and mesh used to establish the accelerating field and used in the ion area detector, as well as ablation losses, contribute most to ion loss throughout APT characterization. Therefore the 3-D reconstructions of a sample produced by APT is more accurately a 'representative' sampling of the sample being characterized, and great efforts are made to ensure the resolved ions are indeed representative of the sample writ large. Even considering that more than half of a sample's atoms are lost in the characterization process APT data sets are enormous as information is collected from upwards of $100nm^2$ of a solid's atoms.

Automated software compiles the time-of-flight measurements and sample reconstruction. As such resolution in the final 3-D reconstruction is dependent on hardware limits - detector grating size and configuration – and software parameters - predominately sample binning, voxel (volume pixel) size, and smoothing functions. In subsequent sections an error analysis is conducted in which these instrumental and analytical contributions to uncertainty are approximated into a single Gaussian uncertainty envelope whose effects on APT data are explored.

History of APT and Soft Magnetic Materials

Modern APT was developed in the mid 1980's and began being available for research throughout the 1990's, close to the same time amorphous and nanocomposite magnetic materials were seeing great advancements in their development. Because of the chemical complexity and the nanosized structure and mechanisms of magnetic nanocomposites APT was quickly applied to these systems. Some of the first efforts to characterize MANCs using APT were done by K. Hono, as the relationship between structure and properties in MANCs was being formalized[41], [43], [46]–[48].

Throughout the 1990's APT tomography characterized several Fe-based MANC systems. In addition to, confirming the characteristics of the nanostructure, APT tomography was the chief instrument being used to investigate the phenomena of Cu clustering, which APT readily reveals in MANCs, and its role in the nucleation of Fe-Si DO3 structured crystalline precipitates in Fe-based systems [43], [46]. It was found that in Fe-based systems Cu is an important nucleation agent, due to Cu clusters acting as heterogenous nucleation cites for primary crystallization[41]. However, the correlation of Cu clusters to nanocrystals was found not to be one to one. Even more so in the Co-based, and to a lesser extent Fe-Co based systems, it was found that the presence of Cu clusters did not correlate to the nucleation of precipitates and can often be omitted[49].

Further work characterizing MANCs with APT provided the understanding of the partitioning of B, Si and Zr during crystallization that is had today and lead to the diffusion controlled transformation mechanisms described in this document [47], [50]. Later work by McHenry, Ohodnicki, and Long further elucidated the partitioning of other glass formers and began to investigate their roll in secondary crystallization[51]. APT has also been used to study the partitioning of Co in both Co-based and Co containing MANCs and even its concentration within crystalline precipitates and this effect on grain size[52], [53]. APT continues to be an invaluable characterization tool for the MANC system, recently investigating MANCs processed through ultrahigh crystallization rates and throughout this work investigating the roll and partitioning of glass formers in this class of materials[42].

4.2 Mass Balance

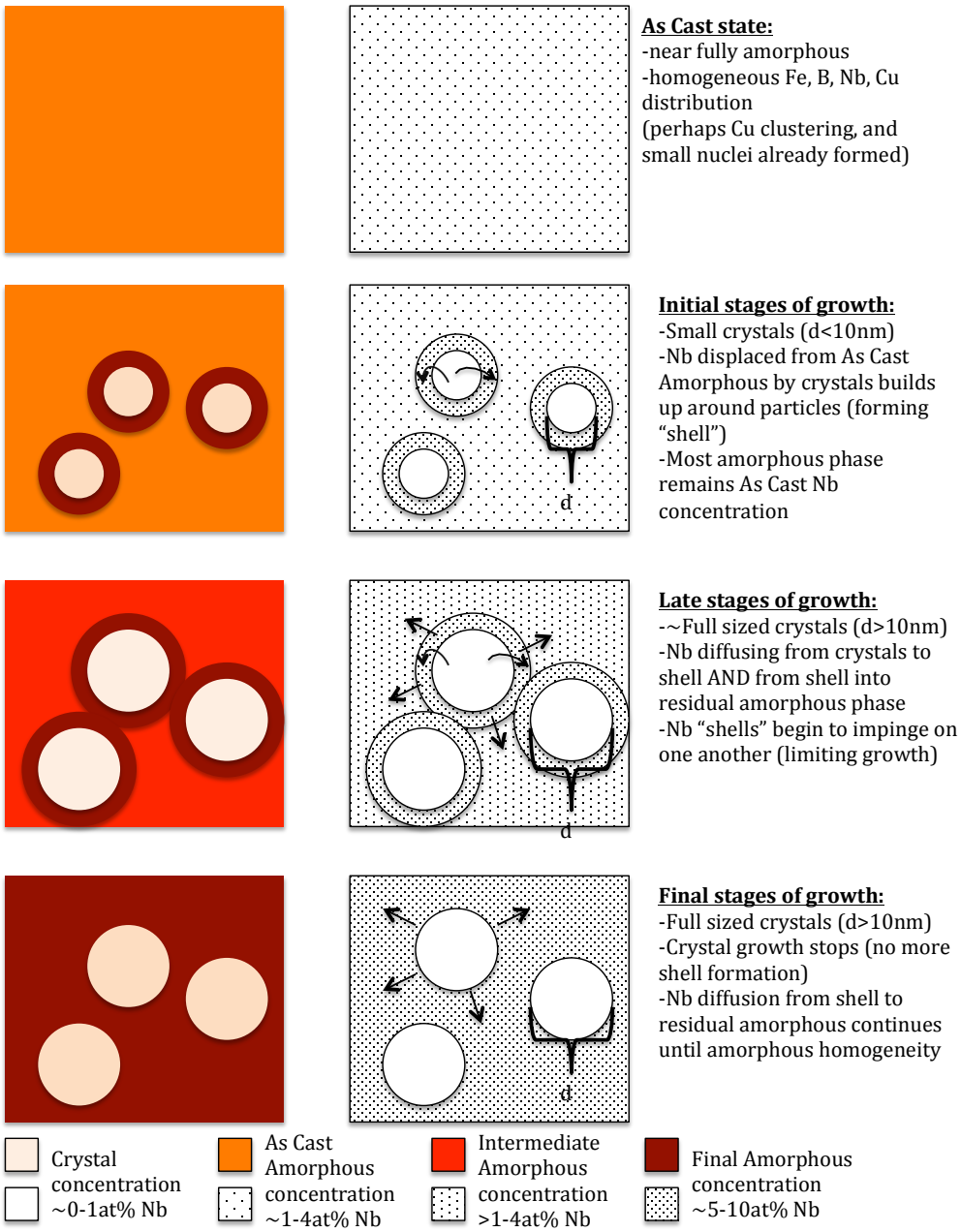

Figure 4.2.1: A Schematic graphic illustrating the chemical partitioning of magnetic amorphous nanocomposites from the as-cast amorphous state and through final stages of partial devitrification, or primary crystallization.

4.2.1 Crystal Fraction and Local Composition

Chemical partitioning, as described by Fig. 4.2.1, in this class of materials has been the focus of previous investigations. Most studies have focused on the diffusional processes limiting growth and several crystallization kinetics models have been developed for nanocomposite materials [5], [54]–[56].

Following the scheme of Pradell et. al., we consider a GF profile for the growth inhibiting species shown in Fig. 4.2.2 for the MANC system throughout crystallization. The fixed GF concentration of the crystalline and maximally enriched amorphous phases are denoted C_{xtl} and C^* respectively. The initial GF concentration of the amorphous phase is C_0 and is equal to the nominal the GF concentration of the overall alloy. The GF concentration of the residual amorphous phase far from a crystal interface, which changes with crystallization, is denoted C_{Am}.

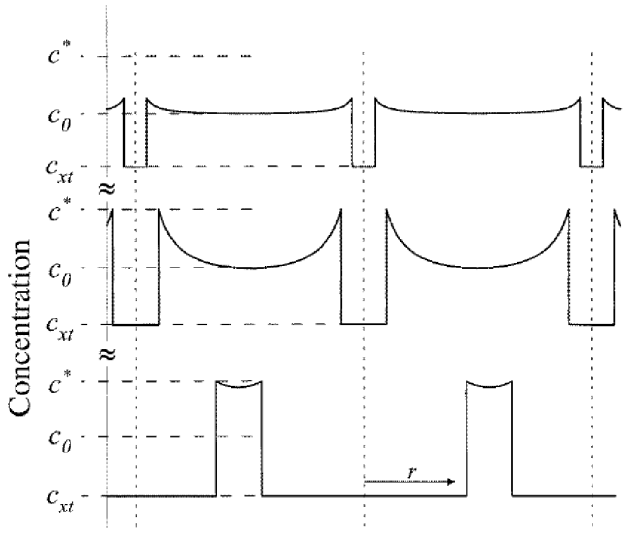

Figure 4.2.2: Concentration profiles of the primary crystallization of MANC show the partitioning of growth inhibiting glass former elements as crystallization proceeds from early stages (top), intermediate stages (middle) and through completion (bottom). [5].

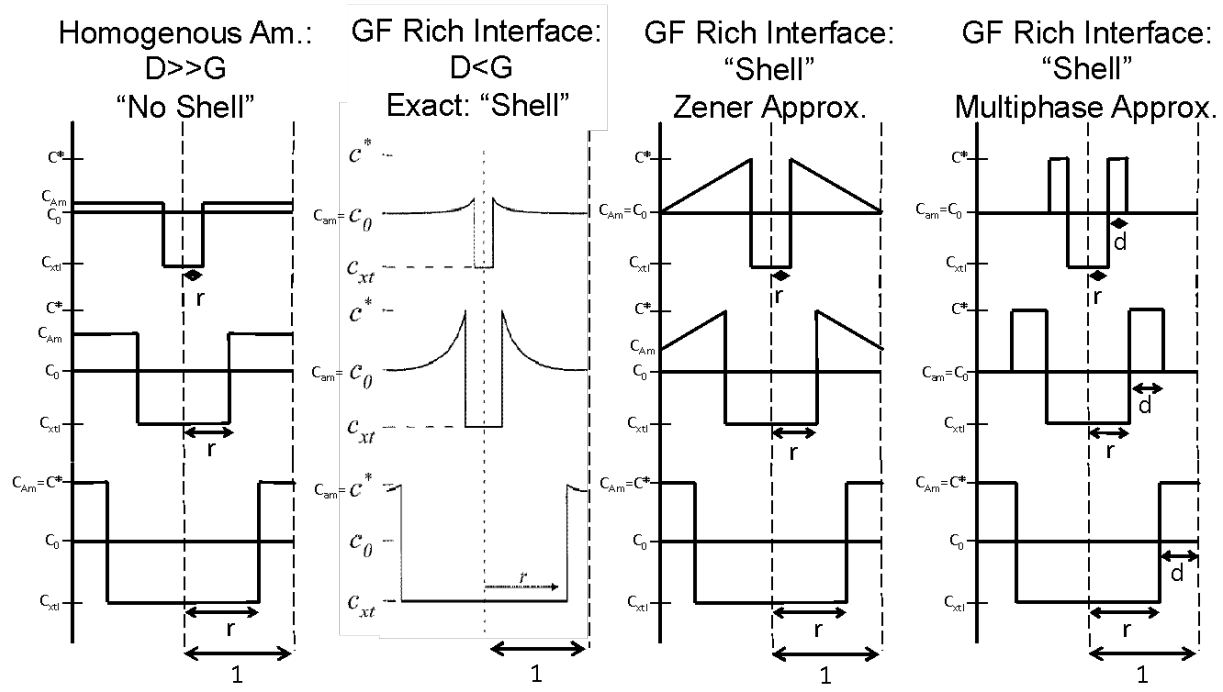

Figure 4.2.3: Various approximations for the concentration profile of MANCs during primary crystallization used throughout this work. (Left) The 'No Shell' approximation in which the amorphous matrix does not feature a concentration gradient. (Center Left) The 'Exact Solution' in which Fick's second law with moving interface and mass balance yields an error function profile in the amorphous phase. (Center Right) The 'Zener ' approximation in which the exact solution is linearized. (Right) The 'Shell' approximation in which the enriched matrix is treated as a distinct, homogenous phase.

	Homogenous Amorphous	Exact Solution	Zener Approximation	Multiphase Approximation
GF Mass Balances	✓	✓	✓	✓
$V_{xt;} \rightarrow V^{f}_{xtl}$: $C_{am} \rightarrow C^*$	✓	✓	✓	✓
Treatable Resistivity	✓	✗	✗	✓
Variable(s) that balances mass:	C_{Am}	C_{am} & "d"	C_{Am} & d	d

Table 4.2.1: For each treatment of the concentration profile the advantages, checks, and limitations are tabulated.

Using this notation a mass balance has been written which accounts for the number of GF atoms expelled from the precipitating crystal, N_{xtl}, and which diffuse into the amorphous phase, N_{Am}, during crystallization [36]. That is,

$$N_{xtl} = N_{Am}. \quad \text{Eq. 4.2.1}$$

At this point we make two assumptions concerning the chemical partitioning of the GFs in the amorphous matrix:

a) Shell: If diffusion of the growth inhibiting GFs is slow compared to the growth rate, G, of the crystal then a GF composition gradient is established within the residual amorphous phase as shown in Fig. 4.2.3(Center Left through Right).

$$D_{GF} << G = \frac{ds}{dt} \quad \text{Eq. 4.2.2(a)}$$

b) No Shell: If diffusion of GFs is fast compared to the growth of the crystal then the composition of both the crystal and amorphous phases will be constant as shown in Fig. 4.2.3 (Left).

$$D_{GF} >> G = \frac{ds}{dt} \quad \text{Eq. 4.2.2(b)}$$

In his original work Pradell assumes (a) and develops his diffusion controlled kinetic model. Following this approach, and approximating the gradient linearly as in the Zener approximation [57], the GF mass balance becomes,

$$(C_0 - C_{xtl})V_{xtl} = \left[\frac{1}{2}(C^* - C_{am}) - C_0\right](1 - V_{xtl}), \quad \text{Eq. 4.2.3}$$

where Vxtl is the crystalline volume fraction.

Following assumption (b) in which diffusion is fast compared to crystal growth and the amorphous phase is considered homogeneous throughout devitrification the mass balance becomes:

$$(C_0\text{-}C_{xtl})V_{xtl} = (C_{am}\text{-}C_0)(1\text{-}V_{xtl}). \quad \text{Eq. 4.2.4}$$

Here we note for familiarity sake that these mass balances, Eq. 4.2.3 & 4.2.4, do for this non-equilibrium amorphous/crystalline composite and metastable system what the tie-line construction and lever rule do for multiphase regions of equilibrium phase systems. That is, these relations scale the amount of each phase, in volume fraction, by the concentration of that phase, in atom percent. Note that in all of these cases the units for the product on each side of the balance are in units of number of atoms, in moles.

In both approximations C_{Am} increases with V_{xtl} and approaches C* upon which primary crystallization ceases as the entire amorphous phase is then both homogenous and equilibrated with the primary crystalline phase. In this state, the two approximations, shell and no-shell, converge and the final volume fraction can be expressed,

$$V_{xtl}^{f} = V_{xtl}^{(C_{Am}=C^*)} = \frac{(C^* - C_{Am})}{(C_0 - C_{Xtl})} \qquad \text{Eq. 4.2.5}$$

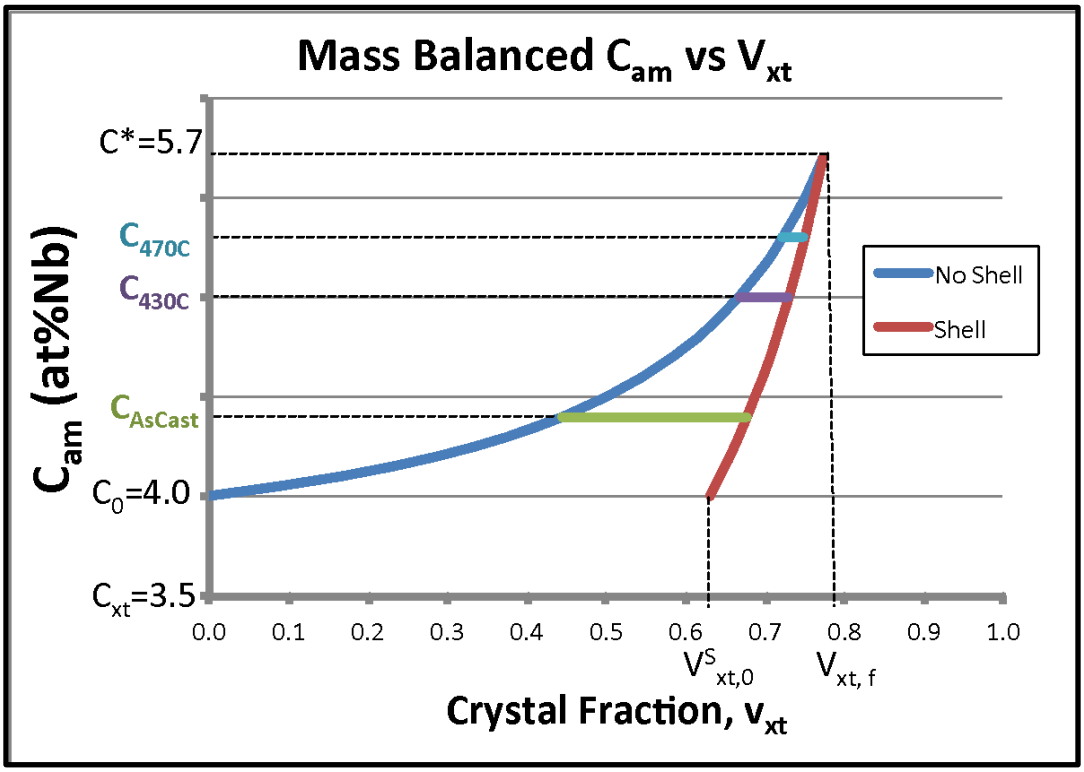

Figure 4.2.4: The local concentration of the amorphous phase far from the crystal interface, C_{Am}, is plotted versus crystal fraction, V_{xtl}, as predicted under the "shell" and "no shell" assumptions of the mass balance. The two approximations converge as primary crystallization approaches completion.

Using the mass balance under both of the GF chemical partitioning assumptions, Eq. 4.2.II(a) & (b), the local amorphous composition, C_{Am}, is plotted as a function of crystal fraction, V_{xtl}, in Fig. 4.2.4. For all but the earliest stages of growth, typically $V_{xtl}>0.5$ for nanocomposites during primary crystallization, both approximations are applicable. As the "No Shell" function illustrates, in systems in which approximation (b) is more accurate the amorphous phase can accommodate more GFs with a smaller crystal fraction. As derived, the convergence of $C_{Am}(V_{Xtl})$ to C* for both chemical partitioning approximations is evident as V_{Xtl} approaches the final primary crystal fraction, V^f_{xtl}. These two trends are general for any $C_{xtl}<C_0<C_{Am}<C^*$ for the primary

crystallization processes of MANCs. These plots also include experimentally determined values for C_0, C*, C_{xtl}, and C_{Am} obtained by Atom Probe Tomography and are further explained in the following section.

4.2.2 Experimental Investigation: Atom Probe Tomography

Atom Probe Tomography (APT) is a high precision, destructive experimental technique by which high spatial and chemical resolution of samples' atomic makeup can be obtained [50], [51]. As described in DeGeorge et al, samples of nominal composition $(Fe_{65}Co_{35})_{79.5-X}B_{13}Si_2Nb_XCu_{1.5}$ in the as-cast and various stages of crystallization were measured at Pacific Northwest National Lab by APT[36]. This experimental technique was used to directly determine the local GF concentrations specified by the Pradell and previously discussed mass balance schemes.

APT produced 3D atom maps of all alloy constituents as shown in Fig. 4.2.5. While more homogeneous than heat treated samples, pre-formed crystals in as-cast samples[54], and Cu clustering in all samples [10], [58] were observed which is consistent with previous reports. Contrary to findings in Co-rich alloys, [10], [51] crystals in this alloy are identified in atom maps as depleted in B.

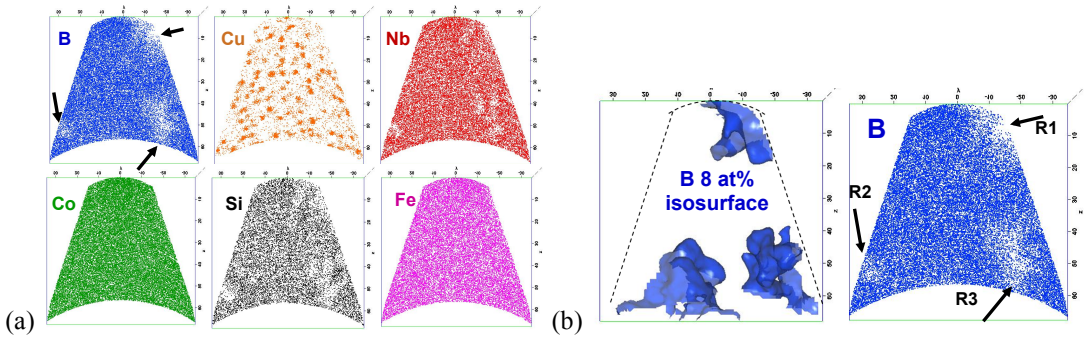

Figure 4.2.5: (a) 3D atom maps obtained through APT for each constituent element for samples annealed at 430C. (b) Boron map, with highlighted 8at% isosurface shows B-depleted regions corresponding to nanocrystals.

To investigate chemical partitioning across phase boundaries, radial concentration profiles centered about B-depleted regions, corresponding to crystals, are produced for each constituent and are shown in Fig. 4.2.6. The interface between the crystal and amorphous phases is taken as the zero position and is formed by analytically constructing Boron isosurfaces (equi-concentration surfaces) at the average of the crystalline and amorphous Boron concentrations. This value tended to be about 8at% for these samples. Boron isosurfaces that

are used as the crystal/amorphous interface are shown in Fig. 4.2.5(b). The construction of these isosurfaces and the crystal/amorphous interface will be discussed in the context of APT precision in the next section.

The local concentrations of each constituent in the crystal phase (B-depleted regions) and amorphous phase (B-rich regions) near and far from the interface were obtained from these profiles and are shown in Table 4.2.2. The concentrations of each constituent in the crystal were found to be constant for the as-cast, 430^{0}C, and 470^{0}C annealed samples. Additionally, average Cu and Si concentrations in the amorphous phase showed little variation with crystal state. Concentrations of Fe, Co, B, and Nb in the amorphous phase far from the interface were found to evolve with crystallization state as reported in Table 4.2.2.

		Fe	Co	B	Nb
	Nominal Overall (at%)	51.7	27.8	13	4
As Cast	APT (at%) ΔC_{am} (at%)	50 +/-0	31 +/-0	13 +/-0	4.4 +/-0
430C	APT (at%) ΔC_{am} (at%)	49 -1	28 -3	14 +1	5 +0.6
470C	APT (at%) ΔC_{am} (at%)	45 -5	24 -7	16.2 +3.2	5.3 +0.9

Table 4.2.2: Evolution of local composition of the amorphous phase with crystal growth shows depletion of TE and enrichment of GF with growth as predicted from mass balances.

Local concentrations obtained through APT were then used in the previously described mass balances. Because Nb has been shown to be the slow diffuser in this system and limits crystal growth [5], local Nb concentrations are used for C_{xt}, C_0, C^*, and C_{am} of Eq. 4.2.III-4.2.V, and results are shown in Fig. 4.2.4.

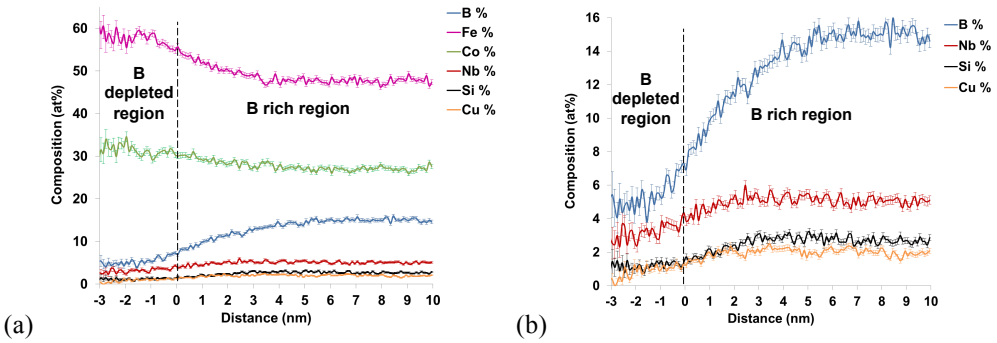

Figure 4.2.6: Composition profiles of HTX002 alloys annealed for 1hr at 430C show (a) crystals enriched in Fe and Co, and (b) the residual amorphous phase enriched in glass formers.

The final volume fraction predicted by Eq. 4.2.V based on these results is $V^f_{xtl,}$= 0.77. This value is consistent with previous studies of MANC alloys [11], [32]. The crystal fractions of the different crystal states

predicted by the two structural approximations corresponding to a given C_{am} can be regarded as limits within which to expect V_{xtl}.

*4.2.3 Physical Limits Establishing C**

In this subsection the physical significance of the parameter C*, which was introduced in the previous section, is expanded upon. Specifically, C* is discussed with respect to its effect on:

1) the concentration of Glass Formers in the 'Shell' or grain boundary phase,

2) the cessation of primary crystallization due to soft impingement as $C_{Am} \rightarrow C^*$, and

3) the conditions for secondary crystallization to proceed massively, i.e. a 'polymorphic burst.'

In this way we will more rigorously link the parameter C* as introduced in the literature to the physical parameters underlying the both primary crystallization and the polymorphic, massive transformation which has been proposed by S. Shen and McHenry et. al. for secondary crystallization in this system[59]. Building upon the previous work of S. Shen and McHenry the argument is made that it is the partitioning of glass formers into the residual amorphous phase during primary crystallization that is the essential prerequisite for the proposed massive polymorphic secondary transformation, if such a transformation does indeed take place. Moreover, it is the specifics of this polymorphic transformation, i.e. phase selection, which establish the physical bounds for which the value C* can take and which determines the onset of secondary crystallization. In this was the concentration of the secondary phase is related through the constraints imposed by such a massive transformation to the maximum concentration of glass formers in the residual amorphous phase, i.e. C*. This section is concluded with an analysis of the pertinent features which much be considered when attempting to measure and determine C* experimentally. Maintaining focus on the APT technique this subsection closes with a simple error analysis simulation developed to illustrate the necessary considerations of experimental precision and uncertainty that complicate the determination of C*.

*The Shell Concentration, C**

As noted in the previous subsection Pradell introduces parameter C* in 1998 when he developed his diffusion controlled crystallization kinetics model[5], [60]. In his original manuscript Pradell asserts that C* is simply "the concentration of the slowest-moving species at the grain boundary." More insight can be gained by a deeper analysis of why and how this comes to be the case. A Gibbs Free Energy diagram for the primary crystallization transformation in which growth inhibitor poor, C_{xtl}, crystallites precipitate out of a metastable amorphous phase of concentration, C* is shown in Fig. 4.2.7. We note the driving force for this transformation, ΔG^0, is largest when the amorphous phase is at its original concentration, C_0.

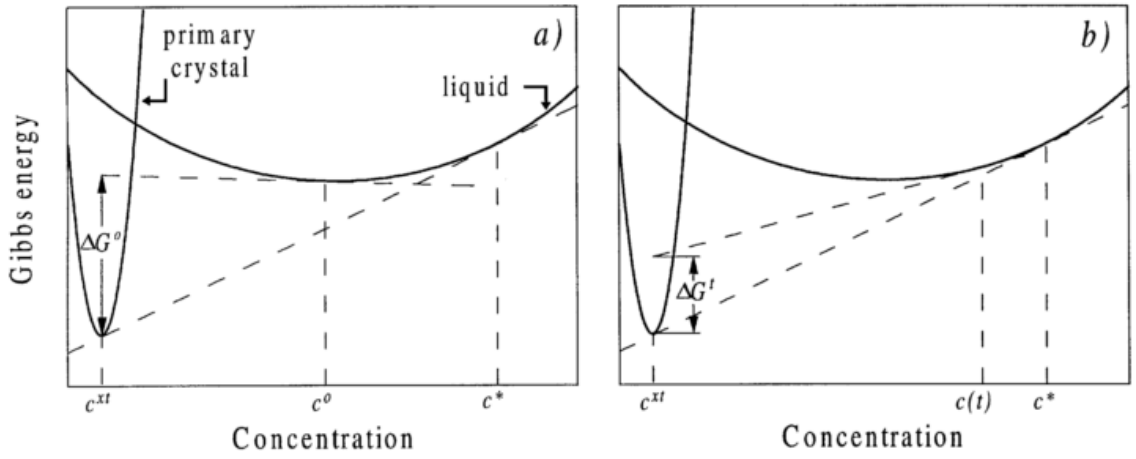

Figure 4.2.7: A schematic Gibbs Free Energy diagram for primary crystallization of alpha (Fe,Co) out of a metastable amorphous liquid shows the relavent compositions, C_{xtl}, C_0, and C*. (Adapted before further editing from [60])

At the earliest stages of nucleation and growth the interface between primary crystallites and the amorphous phase achieves local equilibrium as the *local* concentration increase above C_0 towards C* and the driving force decreases. This occurs very quickly relative to the remainder of the transformation as this is an interface, and not long range diffusion, limited phenomena. When local equilibrium is reached at the interface, when $\Delta G^0 = 0$ and the common tangent has been established, the concentrations of the crystal phase and the amorphous matrix in the immediate proximity of the interface are, C_{xtl} and C*, respectively. And consequently, we note that this area of concentration C* on the amorphous side of the crystal/amorphous interface is precisely how we have defined out 'shell.' (Pradell also refers to it as the 'grain boundary'). The condition of local equilibrium at the

interface is maintained throughout the diffusion limited primary crystallization transformation as glass formers diffuse away from the interface and into the amorphous matrix and the transformation proceeds.

Soft Impingement when $C_{Am} \rightarrow C^*$

Pradell also notes extensively, indeed it is the hallmark of the soft-impingement theory, that primary crystallization terminates as the concentration of the entire amorphous phase, even that far from the grain boundary and interface, approaches the value of C*. Primary crystallization terminates with this convergence of concentrations within the amorphous phase, i.e. $C_{Am} \rightarrow C^*$, because again for the whole system, as it is locally for the interface, this is the common tangent equilibrium condition for which the driving force, $\Delta G^0 = 0$, for the growth inhibitor poor and growth inhibitor rich amorphous phases as shown in Fig. 4.2.7. Thus, just as the grain boundary or shell reaches the glass former concentration C* at the very initial stages of primary crystallization, and maintains this constant concentration through crystallization, at the completion the transformation the entire amorphous phase also approaches this constant concentration, C*.

'Polymorphic Burst' and Secondary Crystallization

At this point it should be noted that the scope of the previous discussion, and indeed that of Pradell, was solely on primary crystallization, and did not make considerations for other, secondary or higher order, phase transformations that can also act on the system. In this way it would be more appropriate to say that the condition for the termination of primary crystallization noted previously, $C_{Am} \rightarrow C^*$, is the condition for termination of primary crystallization *if no other phase transformations take place*. Here now, I discuss the very pertinent scenario of secondary crystallization and not only its effects on the termination of primary crystallization, but indeed the causal relation of the two phenomena.

Following the thorough analysis of Ohodnicki[61] I identify the following conditions for secondary crystallization to proceed via a 'polymorphic burst,' i.e. a very fast, polymorphic massive transformation at the completion of primary crystallization:

1) the existence of 'secondary' metastable phase that is,

2) more stable than the amorphous phase or a two phase - amorphous/crystalline - assembly at,

3) a concentration very close to C*, such that the secondary crystallization event occurs at the end of primary crystallization, and

4) occupies a volume of the matrix with a dimension larger than the critical nucleus of the secondary phase particle, r*.

That is, for a secondary crystal phase, Xtl,2, $G_{xtl,2}(C_2) < G_{Am}(C_2)$ where $C_{Am} \geq C_2 = C^* - \partial$ over a possible polymorphic area, $A_{Poly} \geq r^*$.

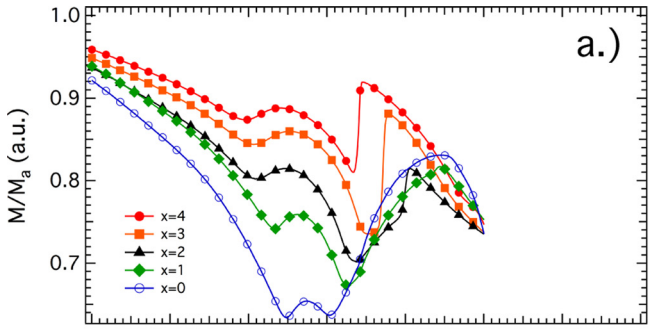

Figure 4.2.9: Magnetization versus Temperature data for the high induction Fe-Co based nanaocomposite that exhibits a 'polymorphic burst' of secondary crystallization after primary crystallization has come to completion[62].

S. Kernion et. al. noted when conducting constant heating VSM Magnetization vs Temperature experiments, the variable growth inhibitor series $(Fe_{65}Co_{35})_{79.5+x}B_{13}Nb_{4-x}Cu_{1.5}$ (x=0-4), an abrupt increase in magnetization associated with the beginning of secondary crystallization[62]. Owing to the sudden onset and short time duration of this event, relative to that of primary crystallization, they have referred to this event as a 'polymorphic burst.' Indeed, secondary crystallization has been observed to proceed polymorphically, i.e. a transformation in which there is no change in composition between the untransformed and transformed regions, in several nanocomposite systems [37], [41], [47], [60], [63], [64].

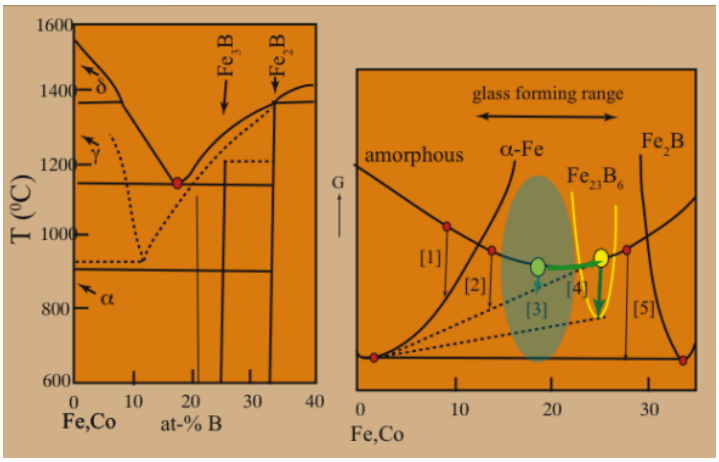

Figure 4.2.10: Schematic phase diagram and Gibbs Free Energy diagram of (Fe,Co)-B shows the relative stability of the amorphous, alpha-Fe, $Fe_{23}B_6$, Fe_3B, and Fe_2B phases and the pertinent concentrations enabling a polymorphic secondary crystallization transformation.

Shown in Fig. 4.2.10 McHenry et. al. has proposed a route for chemical partitioning and the possibility of a polymorphic secondary crystallization transformation [59]. Here I build on that proposal by relating its mechanisms to C*. McHenry's explanation of the polymorphic burst recognizes that owing to the partitioning of glass formers during primary crystallization, as the concentration of the amorphous matrix increases above the original composition, C_0 shown by point 3 in the Gibbs Free energy diagram of Fig 4.2.10, a composition may be reached, shown as point 4, at which the enriched amorphous matrix can lower its Gibbs Free energy by transforming to the 23-6 phase *without any change in composition*, hence a polymorphic transformation.

Building on this we may treat the transformation more specifically by relating the composition of the matrix at which the polymorphic transformation takes place, C_2 (which is the same as the composition of the post transformed secondary phase) to the terminal composition of primary crystallization, C*. P. Ohodnicki et. al. have thoroughly analyzed the phase selection and stability of possible secondary phases and shown that for (Fe,Co)-(Nb, Zr, B) nanocomposite systems this composition is very nearly $(Fe,Co)_{23}(Nb, Zr, B)_6$, i.e. $C_2 \cong 26at\%$ [61]. If a polymorphic transformation has been observed what does that imply about how C_2 and C* are related?

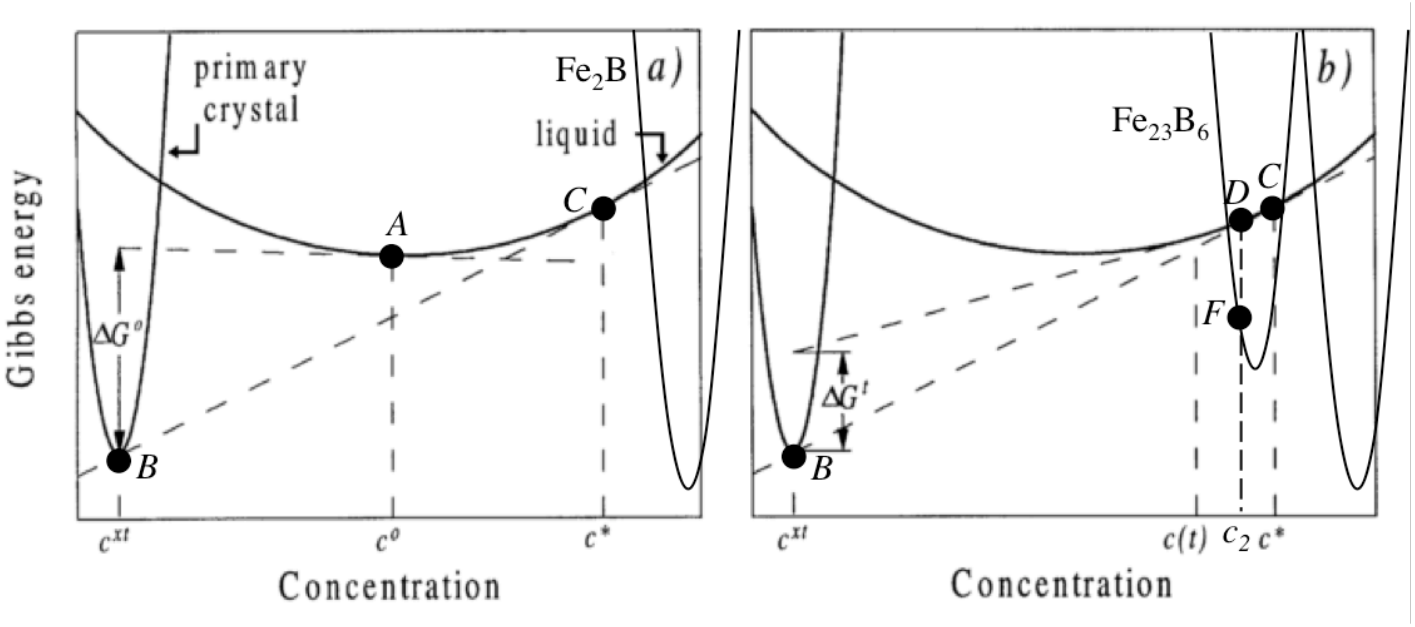

Figure 4.2.11: A schematic Gibbs Free Energy diagram which shows the relation of secondary 23-6 and Fe_2B phases and the pertinent concentrations, $C_{xtl,}$ C_0, C_2, and C*.

As is further illustrated in Fig. 4.2.11 for the (Fe,Co) and (Nb, Zr, B) system, C_2 must be very near and slightly less than C*, i.e. $C_2 = C^* - \partial$, for some small $\partial > 0$. If C_2 were much smaller than C*, for instance in the vicinity of C_0, then a transformation to the 'secondary' 23-6 phase could proceed before 'primary' alpha-(Fe,Co) phase or primary crystallization might produce a two phase crystal product, comprised of the alpha-Fe and the 23-6 phases. Moreover, C_2 cannot be larger than C* because the matrix cannot reach such a concentration via primary crystallization because C* is the maximum concentration the matrix can reach, owing to the fact that once the amorphous matrix reaches C* and equilibrium is established primary crystallization, and consequently chemical partitioning and the enrichment of the matrix, ceases. It may still be possible for an enriched matrix of concentration C_{Am}=C* to transform to a secondary phase with composition, C_2>C*, but because in this case $C_{Am} = C^* \neq C_2$ the transformation would require a change in composition from the untransformed to transformed phases and as such would not be polymorphic.

Thus, in order for secondary crystallization to proceed via a polymorphic transformation primary crystallization must proceed such that the chemical partitioning has enriched the residual amorphous matrix to a composition at least as large as the polymorphic transformation concentration, that is,

$$C_{Am} \geq C_2 = C^* - \partial . \qquad \text{Eq. 4.2.6}$$

Select concentration profiles, under the linearized Zener approximation, are shown in Fig. 4.2.12. In this schematic simulation C_{xtl}, C_0, C* are chosen to be 2, 4, and 8at% respectively. On the left side of the profiles the area of the matrix in which the concentration exceeds $C_2 = C^* - \partial = 7$at%, with $\partial = 1$at%, is highlighted in red. By the prior analysis this is the area in which a polymorphic transformation could occur because the condition of Eq. 4.2.VI, $C_{Am} \geq C_2 = C^* - \partial$, is satisfied. It is noted that this area is very small for the early stages of primary crystallization. Indeed, only a very small portion of the high glass former shell directly adjacent to the crystal/amorphous interface satisfies this criterion. This area increases as the crystal and shell grow and the residual matrix becomes enriched in glass formers. At the final stages of primary crystallization, the entire amorphous matrix satisfies Eq. 4.2.6.

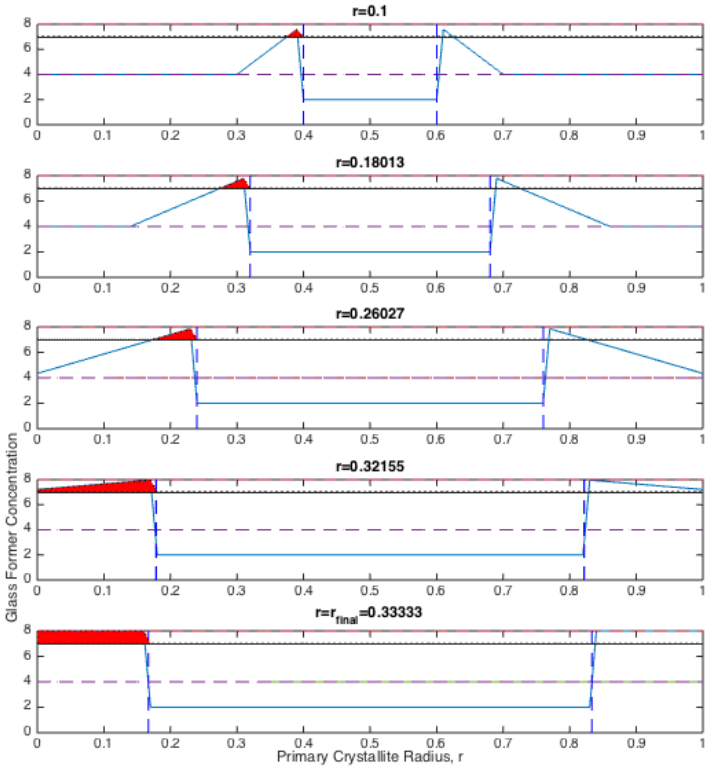

Figure 4.2.12: Concentration profiles of the nanocomposite under the Zener approximation are shown during various stages of primary crystallization and the area of the matrix whose concentration exceeds C_2 and in which a polymorphic transformation could take place are shaded in red.

Continuing this analysis, a plot of the fraction of the amorphous matrix that satisfies the polymorphic transformation criterion, Eq. 4.2.6 is shown in Fig 4.2.13(a). It can be seen that the fraction of the amorphous

matrix which satisfies Eq. 4.2.6, is nonzero and increasing throughout all stages of primary crystallization, i.e. all r>0. The most rapid increase in the amount of matrix available to transform polymorphically occurs near the end of primary crystallization, just before the primary crystal radius, r, reaches its maximum value, r_{max}, a value concomitant with $C_{Am} \rightarrow C^*$ and the termination of primary crystallization. This result is consistent with the observation of secondary crystallization occurring, in a burst, after primary crystallization. However, while there is indeed a significant increase in the amount of matrix satisfying Eq. 4.2.6 towards the end of primary crystallization, the fact that this area is nonzero at *all* stages of crystallization suggests that this analysis implies that secondary crystallization is possible, even if unlikely, also during *all* stages of crystallization. This suggestion is inconsistent with well-documented experimental observation.

To help explain this we further consider the evolution of the concentration profiles shown in Fig. 4.2.12, keeping the size of the critical nucleus, r*, in mind and looking at the dimensions of the area satisfying Eq. 4.2.6. We note two regions in the plot of matrix area satisfying Eq. 4.2.6. The first region is the small, but non-zero area at the initial stages of primary crystallization. This region corresponds to the area of the shell or matrix side of the interface that satisfies Eq. 4.2.6 even at the earliest stages of crystallization when C_{Am} is still C_0 far from the interface. Then we note the second region, the large increase and plateau in matrix area satisfying Eq. 4.2.6 that occurs when the high glass former shells of two neighbors have begun to overlap, that is when we are within the soft impingement regime, and the concentration of the matrix furthest from the interface, C_{Am}, begins to exceed C_2. Can secondary crystal products nucleate from both of these areas? And, are both of these regions able to accommodate, i.e. large enough to accommodate, a nucleus of secondary crystal product that could then grow?

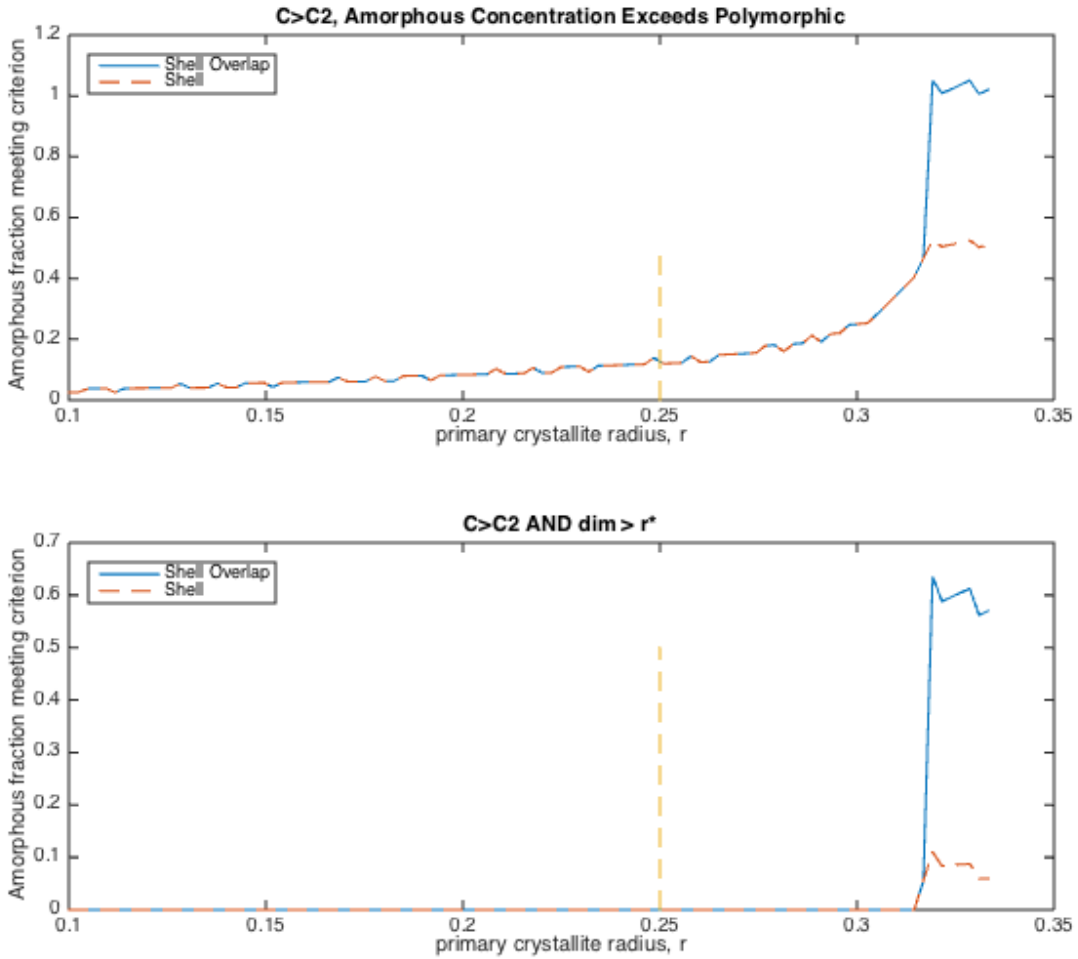

Figure 4.2.13: Plots of the fraction of the amorphous matrix that satisfy certain criterion for a polymorphic transformation to occur verses crystal size. (top) Matrix fraction with concentration exceeds C_2 or Eq. 4.2.VI and (bottom) Matrix fraction with concentration exceeding C_2 and whose size dimension is larger than the critical nucleus of the new phase, r*.

Examination of this question finds that in general both of these areas are not large enough accommodate a secondary crystal nucleus. In order to support a secondary crystal nucleus the area available for the polymorphic transformation must be of spatial dimension, A_{Poly}, greater than the critical nuclei of the nucleating phase. That is,

$$A_{Poly} \geq r^* \qquad \text{Eq 4.2.7.}$$

Eliminating the area which satisfies Eq. 4.2.6 but does not satisfy Eq. 4.2.7 because its dimension is less than the critical nuclei radius, r*, the fraction of the amorphous matrix in which a polymorphic transformation is possible is re-plotted in Fig 4.2.13(b) for the area which satisfies both Eq. 4.2.6 and 4.2.7. While the total area available for polymorphic transformation is less than was the case when only Eq. 4.2.VI was satisfied, the area

available in the shell region at the early stages of crystallization is now zero until much later stages of crystallization. This is more consistent with the observation that secondary does not transpire simultaneously with primary crystallization, but rather commences only after that event is all but completed. Moreover, the area that is available to polymorphically transform is almost entirely due to the diffusion profile overlap far from the interface. And what more, this area becomes available at even later stages of crystallization than in the less case of stringent criterion, essentially when $r=r_{max}$, and it become available even more abruptly (over a smaller range of r) than before! This result, which followed directly from our analysis of primary crystallization - C* and the primary crystallization equilibrium/termination conditions - and of secondary crystallization - C_2 and the phase selection and commencement conditions - is a very satisfying explanation of the observed 'polymorphic burst' of secondary crystallization.

*Uncertainty in Measuring Determining C**

As discussed this work employed APT in attempt to corroborate theoretical models and the parameters that comprise them to laboratory experiment and the measurement of the same. While the prior analysis of APT data was satisfactorily used to corroborate the mass balance and chemical partitioning models, here I take the opportunity to comment on some of the complications that have come to light in doing so. Primarily I discuss the uncertainty and error in the APT data particularly with regard to the sharp, discontinuous regions of the constructed concentration profiles and consequently the determination of C*, which by definition lies at a sharp, discontinuous interface. I assert that the experimentally obtained constructions of the concentration profiles of the nanocomposite system are both scientifically meaningful and useful, as they have been used in the previous sections, even if their use requires some careful explanation and interpretation.

Compared to the theoretical concentration profiles shown in Fig. 4.2.2 or Fig 4.2.3(Center Left), the concentration profiles constructed from the APT data, and shown in Fig. 4.2.6 and/or 4.2.14, appear different. While far from the interface the constructed profiles adequately show the crystalline and amorphous regions rich in Fe and Co and depleted in glass formers and vice versa, at the interface the constructed profiles show a smooth, gradual, and continuous transition from crystal to amorphous instead of the sharp, discontinuous step

profile predicted by the theory. An error analysis of the APT measurement and concentration profile construction is instructive to explain these discrepancies.

There are several sources of error incumbent of Atom Probe measurements, including but not limited to 1) experimental error - which is incurred during the ablation, travel, and most importantly the detection of sample ions - and 2) analysis/software error - which is incurred after the physical measurements have been taken and very large, very precise multidimensional data sets are processed by software to be presented to the user. After discussing these two types of error a simulated error analysis is performed which combines contributions in error from both of them into one overall technique error.

The most significant sources of experimental error occur during ablation in which the sample is very locally exposed to either very high temperatures, very large electrical potential fields, or both whose aim is to remove ions from a given locale of the sample but which can due to the limits of precision of the ablating forces remove ions from slightly neighboring positions as well. The other main source of experimental error comes from the detection of ablated ions. Collection rates for the number of atoms in a sample are around 30%. While this may seem detrimental to an experimental technique, users of APT are fortunate in that the 70% of atoms lost are representative of the sample itself, so that there is no preference as to which atoms are lost or detected. The ion detectors themselves also introduce error into the measurement. Most ion detectors are comprised of at least two but possibly more sets of crossed electrode wires, such that the two, or more, dimensional position of an ion incident on this grid of wires can be determined. The finite width of the wire and the finite mesh of the grid imposed a working limit on the precision of the ion detector. Combined experimental error can be as small as hundreds of Angstroms, but is typically ones of nanometers.

Analysis or control error is another substantial contributor to the uncertainty in APT measurements. Because APT measures very large sample volumes, on the order of $10^4 nm^3$, and detects 10^{6-9} atoms (even considering the low detection rates) each assigned with a three-dimensional position and chemical identifier APT data sets are very large. In order to ensure manageable computational time analytics are performed to simplify the data while maintaining its scientific significance. A. Devaraj noted that the largest analytical limiter to the precision of APT data is introduced when the 3-D position of each detected ion is assigned, or binned,

into to ‘voxels’ (‘volume pixel’) with additional criterion accounting for ‘border cases’ which also introduce error. Again voxel size is chosen to optimize resolution and computation time and is typically less than 3nm, while the overall analytical error is on a similar size scale.

To explore what the effects of APT’s uncertainty on the construction of nanocomposite concentration profiles might be I conducted an error analysis simulation in Matlab. A theoretical concentration profile with a constant crystalline concentration, C_{xtl}, a concentration gradient in the amorphous phase following a error function in position, and a discontinuity from C_{xtl} to C* at the interface between them was constructed as shown in Fig. 4.2.14($\Delta X = 0$). The concentrations at randomly selected positions within this theoretical profile were then sampled. To simulate the effect of uncertainty in the APT measurement and resultant concentration profiles, these sampled positions and concentration were then used to reconstruct the ‘theoretical’ profile into a ‘simulated’ concentration profile. However, the simulated reconstruction introduced variable uncertainty in the position of the sampled data, so that the simulated position of each data point was only constrained to be within a Gaussian probability distribution, with standard deviation Δ in nm, of its originally sampled theoretical position. The concentrations associated with each sampled point were averaged across these new positions, which is consistent with the ion counting as occurs in APT, and the new simulated concentration profiles are constructed, as shown in Fig. 4.2.14 for increasing uncertainty, Δ.

While the theoretical and simulated profiles agree very well in both the crystalline and amorphous phases far from the interface, the most dramatic differences in the profiles for any uncertainty, $\Delta > 0$, is that the sharp, discontinuous interface necessarily becomes 1) continuous and 2) more gradual or smooth. The smoothing at the interface results in the maximum concentration of the amorphous matrix, C*, directly adjacent the interface no longer being reached. Instead, the maximum value of the matrix appears a few nanometers away from the interface and takes a value less than theoretical C*. Even for uncertainty as small as $\Delta = 0.5nm$, far better than was achieved in our experiments a theoretical concentration profile with $C^{*,theory} = 8$at% yields a ‘simulated’ profile with peak amorphous concentration $C^{*,Sim} \cong 6$ at%, and $\Delta = 1.0nm$ yields $C^{*,Sim} \cong 4$ at%. These correspond to 25% and 50% errors respectively.

In light of this error analysis we are reassured that despite the differences in the concentration profiles obtained through APT and predicted by theory, both are scientifically meaningful and can be used, after the appropriate interpretation, to corroborate one another.

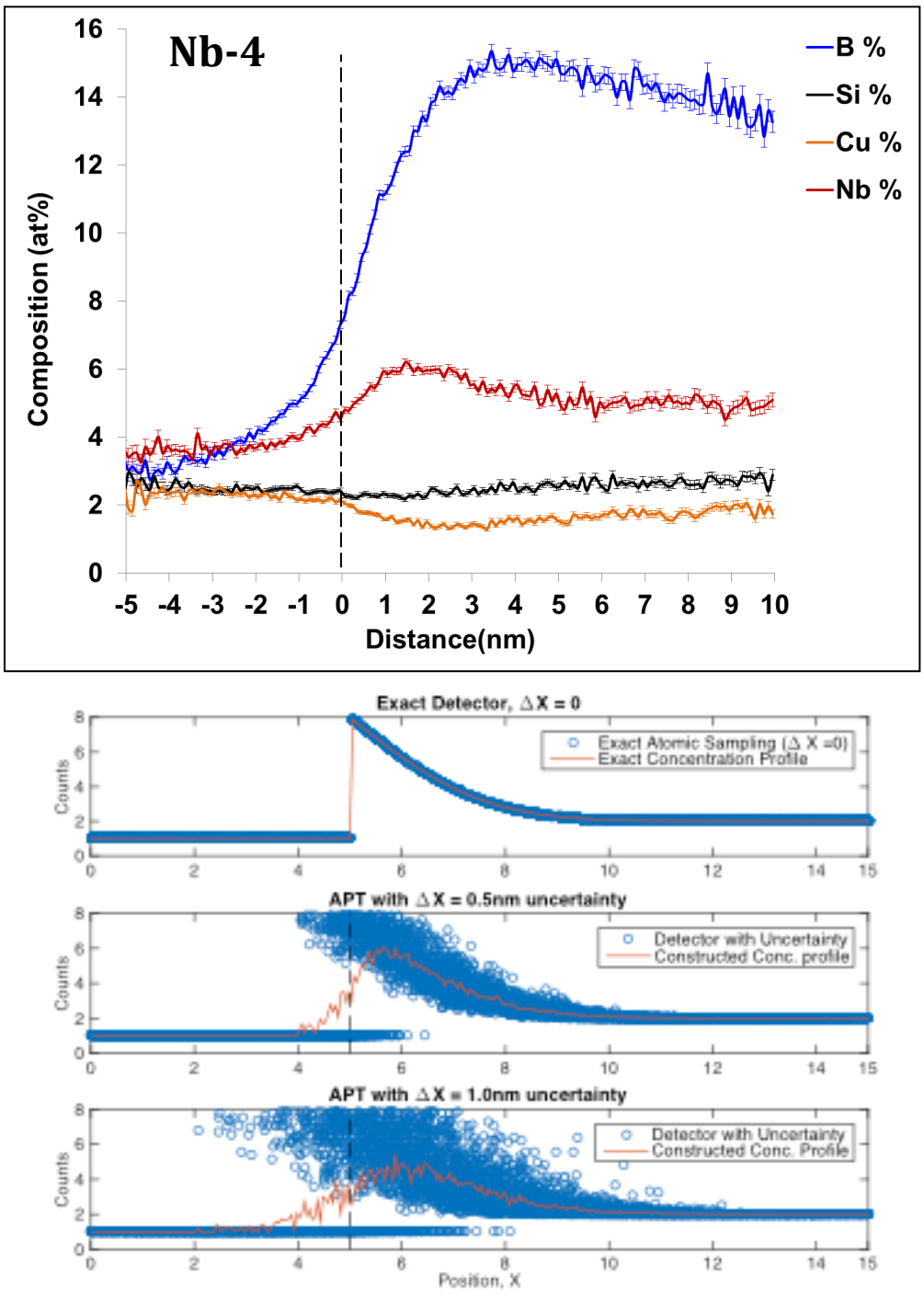

Figure 4.2.14: (Top) Experimentally obtained concentration profile from APT. For a crystal phase, X<5nm, and amorphous phase, X > 5nm, the concentration profiles for growth limiting species across their interface from APT experiment, theory, and from an error analysis simulation featuring uncertainty in position are shown. (Nb-4): Sample concentration profile from APT. ($\Delta X = 0$): Theoretical profile with exact position sampling. ($\Delta X = 0.5nm$): Simulated profile with .5nm uncertainty. ($\Delta X = 0.5nm$): Simulated profile with 1.0nm uncertainty. Interface at x=5nm. 10,000 sampled points.

4.3 Secondary Crystallization TTT Diagram

"Nucleation is the greatest known example of the free enterprise system! So many atoms are present…that the system can attempt at lease once to begin forming any physically possible design of nucleus." "The nuclei that actually form are not necessary those of either the most stable or lowest free energy composition, but simply those that form most rapidly."

-H. Aaronson[65]

The pathway from the amorphous precursor to the equilibrium state in these alloys is a long, multistep one. This notion lends itself to the high engineerability of these materials. Developing a Time-Temperature-Transformation (TTT) diagram for secondary crystallization so as to better characterize the thermal stability of the nanocomposite is the focus of this chapter.

Figure 4.3.1 The pathway to equilibrium from the amorphous precursor is a multistep process of which primary crystallization and secondary crystallization events have been most studied.

As represented in previous chapters, primary crystallization is often the focus of crystallization studies in these alloys. Apart from simply being the first crystallization event that occurs in these alloys, primary crystallization is studied because of its beneficial effects to MANCs' properties.

The amorphous/α-FeCo nanocomposite structure resulting from primary crystallization is not the equilibrium state for these alloys however and as such is not the last phase transformation to take place. Following primary crystallization and the accompanying chemical partitioning secondary crystallization occurs. For many of the MANC alloys the secondary crystal product is the cubic $(Fe, Co, Nb)_{23}B_6$, or 23-6, phase of the $Cr_{23}C_6$ prototype and $Fm\bar{3}m$ space group as has been previously reported[59], [62].

Because the $Fe_{23}B_6$ phase, and most crystal phases that occur after it, do not have the desirable magnetic properties associated with alpha-(FeCo) it is engineered so as to be avoided in MANCs. To this end understanding crystallization kinetics of this crystallization event so as to be able to predict the thermal stability of the amorphous/α-FeCo crystalline nanocomposite is of considerable interest, as is a Time-Temperature-Transformation (TTT) diagram of secondary crystallization for the Co-based HTX005, $Co_{77.4}Fe_{1.4}B_{14}Si_2Nb_4Mn_{1.4}$, alloy.

Following the example of Hsiao et. al., Differential Scanning Calorimetry (DSC) was conducted on this alloy to construct the TTT diagram[66]. A four stage heating profile, shown in Fig. 4.3.2 was developed and used to extract the necessary information from the measurements. The four stages of the scanning profile and the purpose each serves are as follows[35] :

(I) Standard Primary Crystallization Constant Heating: Constant heating from 300 to 570C at 30C/min is conducted on all samples to produce a uniform primary crystal product from which secondary crystallization can proceed.

(II) Variable, time and Temperature, Isotherm: An Isotherm of variable temperature, T, and time, t, is held allowing for secondary crystallization to proceed to various stages of completion.

(III) Rapid Quench: This standard stage simply ensures that any crystallization events that are still occurring at the completion of stage II cease before beginning stage IV.

(IV) Standard Secondary Crystallization Constant Heating: Much like stage I this is a standard constant heating for all samples from 400C to 750C at 30C/min during which any secondary crystallization events which did not proceed to completion during stage II will occur.

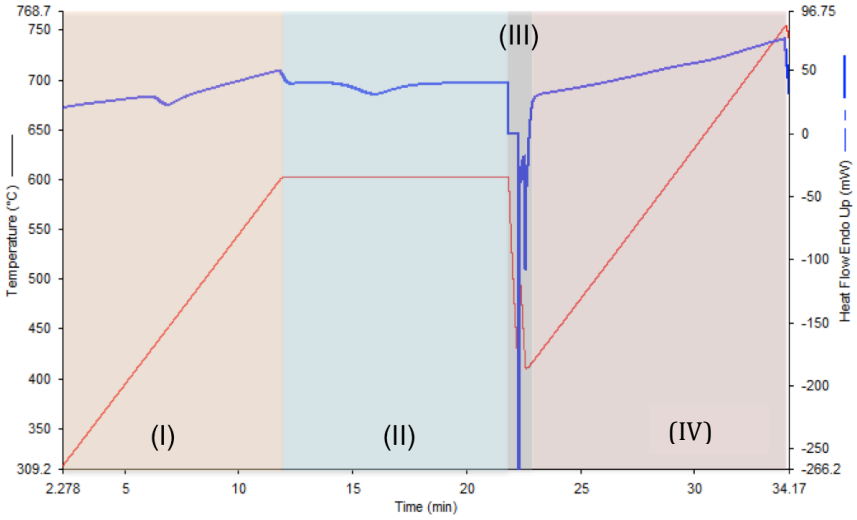

Figure 4.3.2 The four stage heating profile used to collect the information needed to construct a TTT diagram for secondary crystallization.

By monitoring the heat evolved during stage IV one has an indicator of the extent to which secondary crystallization occurred for a given time, t, and temperature, T, heat treatment during stage II. This is shown in Fig. 4.3.3.

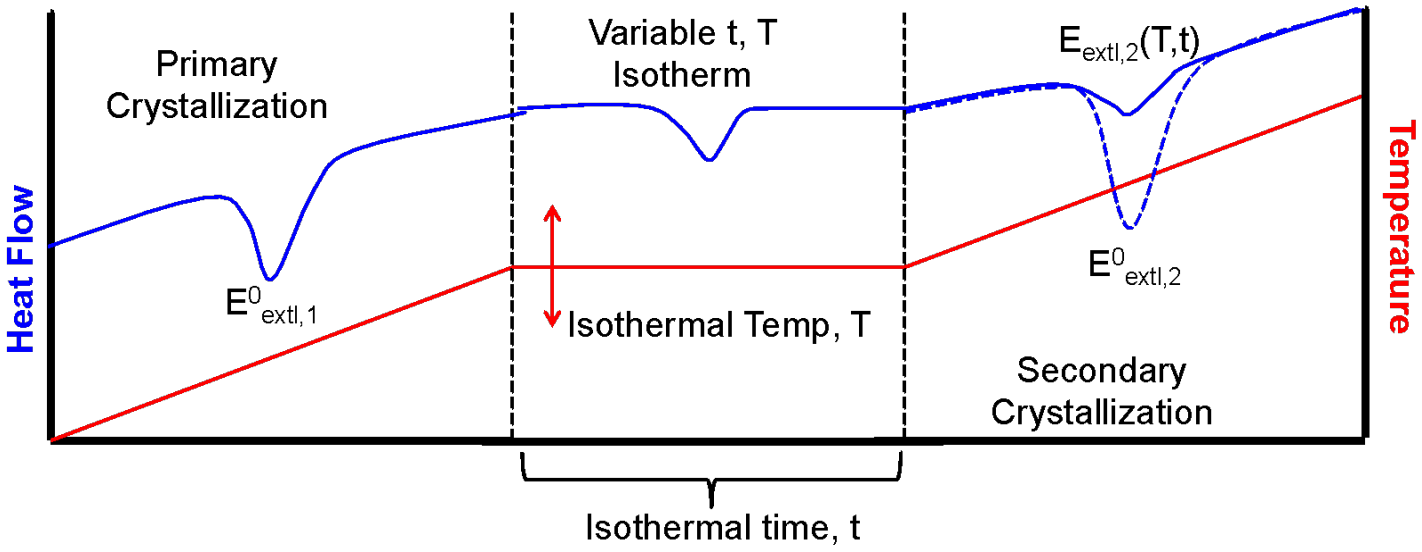

Figure 4.3.3 Schematic of the four stage DSC heating profile used to elucidate the secondary crystal fraction of HTX005 alloys for different heat treatments.

Specifically, by comparing the variable heat evolved of the exothermic peak in stage IV, $E_{xtl,2}(t,T)$, to the area of the peak corresponding to secondary crystallization going to completion, $E^0_{xtl,2}$, as in Eq 4.3.1 the

fraction of secondary crystallization that has gone to completion, f_2, referred to as the "reduced volume fraction," can be obtained.

$$f_2[\%] = \frac{E_{xtl,2}(T,t)}{E^0_{xtl,2}} \qquad \text{Eq. 4.3.1}$$

$E^0_{xtl,2}$is obtained from conducting scans which omit the variable time/temperature isotherm, stage II, such that all of the secondary crystallization occurs during the constant heating run of stage IV.

Reduced volume fraction as a function of time and temperature are shown in Fig. 4.3.4 and as a contour plot of the more conventional TTT diagram in Fig. 4.3.5. For a given isothermal time familiar "S"-curves with annealing temperature are observed. The contour TTT diagram begins to map the bottom, nucleation limited, portion of the "C"-curves typical of nucleation and growth transformations and allows predictions of the thermal stability of the amorphous/primary crystallite compose at elevated temperatures.

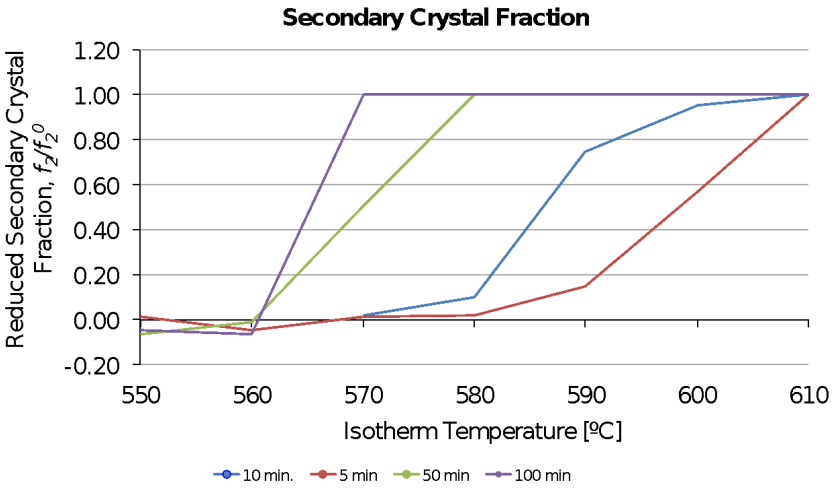

Figure 4.3.4: Volume of secondary crystallization product normalized to final secondary crystallization product after 5, 10, 50, and 100 minute variable temperature isotherms shows "S-curve" characteristic of crystallization.

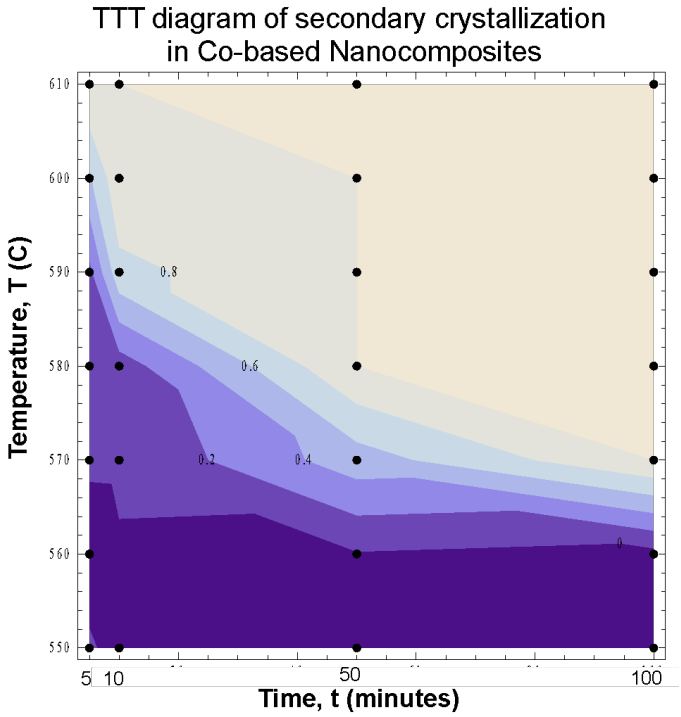

Figure 4.3.5: TTT diagram for secondary crystallization in Co-based $Co_{77.4}Fe_{1.4}$ $B_{14}Si_2Nb_4Mn_{1.4}$ nanocomposite showing reduced secondary volume fraction contours from 0.0 to 1.0.

Chapter 4 Conclusions

In all it can been seen that chemical partitioning is a defining feature of the nanocomposite system. The distinct and elegant considerations of conventional JMAK theory the phenomena requires have been discussed as has been the progress in using APT to study this phenomena. It was shown that through consideration of chemical partitioning the local nanocomposite concentration can be related directly to the crystal state by use of a mass balance and under several approximations for the concentration profiles. This mass balance was also corroborated with experiment by APT measurements conducted on the variable growth inhibitor high induction nanocomposite alloy. Finally, the richness of the scientific theory surrounding chemical partitioning during primary crystallization and its effects on determining the onset and polymorphic nature of secondary crystallization were explored in a discussion of the final amorphous matrix concentration, C*. A simulated error analysis for APT measurements used to obtain concentration profiles and determine local compositions including C* from ATP data explained discrepancies between the theoretical and experimental profiles as well as the necessary considerations for interpreting these profiles. Finally, a TTT diagram for secondary crystallization that conveys the thermal stability of a Co-based nanocomposite alloy was constructed and presented.

Chapter 5.0 Resistivity and VBS due to 3d Impurities in Co Alloys

5.0 Resistivity and VBS due to 3d Impurities in Co Alloys

This chapter focuses on the electronics structure, the fundamental physical origin of the electro-magnetic properties - particularly electrical resistivity but also magnetic moment - that make Magnetic Amorphous Nanocomposites (MANCs) exciting for device applications. A brief overview of electrical resistivity, or concomitant electrical conductivity, in these materials is given in which the structural and electronic origins of the high resistivity are discussed. Focus then concentrations on the contribution of electronic structure to resistivity as the band structure of these materials is discussed and the relationship between the electronic properties and the Density of States (DOS) is noted. After this groundwork has been laid, a model of Virtual Bound States due to impurity 3d Early Transition (TE) metals in both crystalline and amorphous Cobalt is presented. The model is a simple extension of VBS theory as has been well established for impurities in crystalline alloys in which the Lorenzian type DOS observed in metallic systems with 3d impurities is semi-empirically superimposed onto rigid band structures for Cobalt. The results of this model are compared to a V, Cr, Mn doped series of amorphous Co-based alloys measured experimentally and demonstrate the adequacy of this treatment in explaining the effects of even dilute impurities on the electrical resistivity of MANCs.

While this chapter suggests and gives physical arguments attributing the observed properties to the presence of VBS due to the addition of dilute 3d impurities in Co-containing alloys, advanced spectroscopic techniques which directly probe the electronic structure of materials is required to experimentally confirm this assertion.

This chapter summarizes and contextualizes work that from the following publications:

1) “Stress Induced anisotropy in Co-rich magnetic nanocomposites for inductive applications.” A. Leary, V. Keylin, A. Devaraj. V. DeGeorge, P. Ohodnicki, M. McHenry. Journal of Materials Research. Vol. 31, 20. (2016). [34]
2) “Virtual Bound States from 3d Impurities in Amorphous Cobalt” Not you submitted.

5.1 Resistivity in Amorphous Materials

One of the most attractive properties of MANCs is their high electrical resistivity. In high frequency switching applications high electrical resistivity reduces switching losses, and soft magnetic materials like Si-Steel, Ferrites, and MANCs have been engineered to maximize this property. As shown in Fig. 5.1.1, about an order of magnitude increase in electrical resistivity is achieved in going each from pure metals, to metallic alloys, to amorphous metallic alloys. The electrical resistivity of pure metals tends to be as low as the order of $10^0\ \mu\Omega cm$. e.g. ($\rho = 1.7, 2.8, 5.6, 10.0\ \mu\Omega cm$ for Cu, Al, Co, and Fe respectively). Crystalline alloys tend to exhibit resistivities on the order of $10^1\ \mu\Omega cm$, largely through the effects of chemical disordering in these alloys. e.g. ($\rho = 11.3,\ 14.3,\ 17.6,$ and $46.0\ \mu\Omega cm$ for AuCu, Fe-C [steel], AlCu, and Si-Fe respectively). Additionally introducing the structural disorder of amorphous metals, metallic glasses tend to exhibit resistivities on the order of $10^2\ \mu\Omega cm$. e.g. ($\rho = 76.1,\ 123.0,\ 130,$ and $137\ \mu\Omega cm$ for Ga-Au, Pb-Ag, $Co_{70}Fe_5Si_{10}B_{15}$ and $Fe_{73}Si_{14}B_9Nb_3Cu_1$ amorphous alloys respectively). Ferrites can exhibit resistivities as high as $10^{6\text{-}8}\ \mu\Omega cm$ but largely through contributions of the Oxygen to their crystal structure.

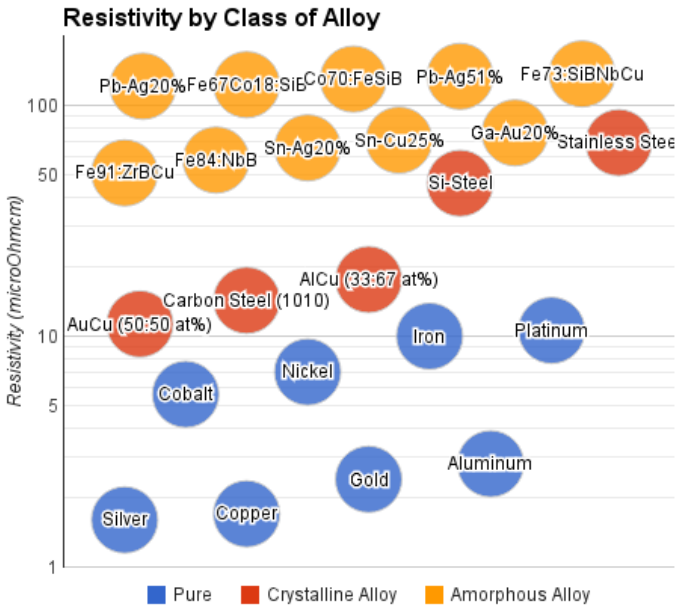

Figure 5.1.1: The resistivity of metals and alloys for Pure Metals (blue) which are both chemically and structural well ordered, Crystalline Alloys (Red) which can feature some chemical and/or structural disorder, and Amorphous Alloys (yellow) which are both chemically and structurally very disordered.

While the fundamental, physical source of electrical resistivity lies in the electronic band structure of a material, phenomenological explanations can be useful in gaining an approximate understanding of this property. Phenomenologically, resistivity is attributed to the ease or difficulty with which electrons can drift

through a material. In a *mean free path* or *mean free time* formulation Drude theory treats this process of free electrons comprising an 'electron sea' or 'free electron gas' drifting through an electric potential within a material until their flow is interrupted by 'scatterers' or 'scattering events.' Scattering centers can include: the crystal lattice, interstitial, substitutional, or vacancy impurities, grain boundaries, dislocations or other defects, and surfaces to name a few. The *mean free path,* λ, or *mean free time,* τ, represent the average length, of distance or time respectively, that a free electron can drift in a given material before it encounters a scattering center. These quantities are related to the resistivity, or inversely conductivity, σ, of a material through the Drude equation as follows,

$$\rho = \frac{1}{\sigma} = \left(\frac{m}{nq^2\tau} \right) = \left(\frac{mv}{nq^2\lambda} \right) \qquad \text{Eq. 5.1.1}$$

where *m*, *n, q,* and *v* are the mass, number density, charge, and average drift velocity of free electrons in the material. Thus, if a material has more scattering centers and the scattering distance, λ (or concomitantly time, τ) shorten the resistivity of that material increases. This phenomenological treatment works well for metals and alloys, including amorphous alloys, whose conduction electrons are well approximated as a free electron gas.

Due to the wave nature of electrons and the periodicity of atoms comprising matter the resistivity of materials can also be explained in general terms of the order/disorder of a material. A compelling example is the temperature dependence of most metals and alloys. In general, as the temperature of materials increase they become more disordered. The very precisely positioned periodic crystal lattices and the atoms that occupy them in crystalline materials begin to increasingly disorder as a material's temperature increases and vibrations and oscillations cause the positions of lattices and their atomic bases to become less well defined than they may be at low temperatures. As a consequence the temperature dependence of most 'well behaved' materials is positively correlated to temperature, and these materials have a positive temperature coefficient of electrical resistivity, usually denoted, α, and related to a material's resistivity as,

$$\rho(T) = \alpha T + \rho_0 . \qquad \text{Eq. 5.1.2}$$

Here ρ_0 is the *residual resistivity* of a material, that is, the resistivity of a material at T=0K, at perfect ordering. There are of course other modes of ordering and disordering than temperature in materials, e.g. structural or even magnetic phase transformations. The next two subsections discuss chemical and structural (dis)order and their role as the primary contributors to the high electrical resistivity of amorphous and nanocomposite materials.

5.1.1 Resistivity and Chemical/Structural Disorder

The Au-Cu system demonstrates the notion of chemical (dis)ordering and its effect on electrical resistivity within the context of a simple binary alloy system, the lessons of which can be generalized to more complex, multicomponent systems.

As evident in Fig. 5.1.1 the resistivity of even binary alloys can be more than an order of magnitude larger than that of their pure element constituents. For example, while the electrical resistivity of pure Cu and Au are 4.81 and 5.71 $\mu\Omega cm$ respectively on the 700K isotherm, shown in red in Fig. 5.1.2(a), at this temperature the electrical resistivity of the 50:50at% CuAu alloy is 16.63 $\mu\Omega cm$. Noting that all Cu, Au, and their binary alloy above 410C have the same A1 fcc crystal structure with space group Fm3m across the entire composition spectrum the nearly three-times increase in resistivity can be attributed to chemical (dis)ordering which in this system varies with composition as well as independently with temperature. Within the A1, chemically disordered fcc lattice the probability of knowing what a neighboring atom on the lattice is (Cu or Au) given the species of an origin atom goes from a maximum of 1.0 or 100% at the two ends, 100%Cu or 100% Au, to a minimum of 0.5 or 50% at the midpoint 50:50at% Cu-Au. The chemical disordering exemplified in this binary system contributes to increased resistivity in this, other binary, and also multicomponent alloy systems - including amorphous alloys and high entropy alloys - in which the irregularity of chemical species which conduction elections must navigate leads to large electrical resistivities.

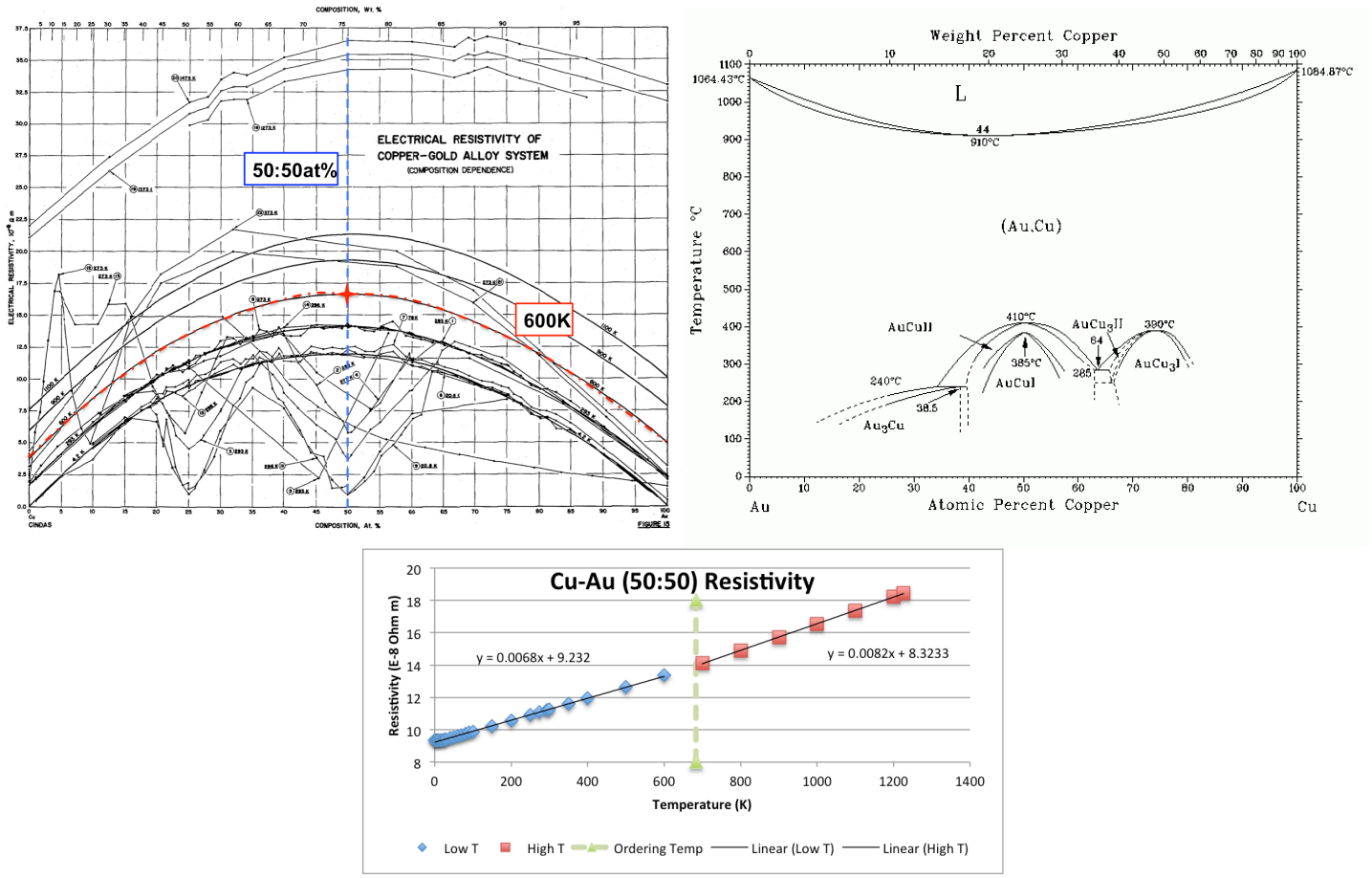

Figure 5.1.2: (a) A plot of electrical resistivity versus composition for the AuCu system demonstrates the chemical (dis)ordering that occurs in this system at, for instance, the 600K isotherm or the 50:50at% constant concentration profile. The order/disordering that leads to the dependence of resistivity independently on both composition and temperature is explained with the AuCu phase diagram (b) and by the plot of resistivity versus temperature for the 50:50at% alloy (c) in which the A1 to L10 order/disorder phase transformation is evident.

In addition to exhibiting chemical (dis)ordering across composition at constant temperature, the Au-Cu binary system also demonstrates chemical (dis)ordering with temperature at constant composition through an (dis)order phase transformation. Shown on the AuCu phase diagram in Fig. 5.1.2(b), the 50:50at% constant composition line, shown in blue in Fig. 5.1.2(a), features the disordered A1 fcc phase noted earlier at high temperature, 410C < T < 910C. Below 410C, the crystal AuCu system still exhibits a closed-packed fcc crystal structure but due to the low entropy at these temperature this fcc phase is chemically ordered and takes the L10, structure, with $P\frac{4}{m}mm$ s (#123) space group. While the lattice parameter also varies with temperature owing to thermal expansion, the is phase transformation from L10 to A1 is characteristically an order/disordering transformation with the chemical ordering giving rise to the change in crystal symmetry between the two phases. This order/disordering transformation is noted because, like the (dis)ordering with composition

exhibited by this system, the L10 to A1 transformation also exhibits an increase in resistivity, shown in Fig. 5.1.2(a & c). The A1/L10 transition at 683K (410C) leads to a 17% increase in the electrical resistivity's Temperature coefficient at 50:50at% Cu:Au shown in Fig. 5.1.2(c).

The AuCu system is introduced here to provide a simple example of the notion that chemical disorder can be large contributor to electrical resistivity for multicomponent systems as it is for this simple binary alloy. Indeed, the chemical disorder of amorphous and nanocomposite systems, which tend to feature four or more chemical species, is one of the primary contributors to this system's high electrical resistivity.

5.2 Electric Structure and Electronic Properties

While the phenomenological explanations of electrical resistivity may be instructive for some general trends, at its root the fundamental physics to which electrical resistivity can be attributed lies in the electronic structure of materials. Most of the properties, including electrical resistivity, of metals and alloys arise from the material's valance electrons. The number of valence electrons per atom, *N*, for a metal or alloy of composition $TL_XTE_YM_UN_V$ – as in the general case of MANCs - can be written,

$$N = XZ_{TL} + YZ_{TE} + UZ_M + VZ_N \,, \qquad \text{Eq. 5.2.1}$$

where Z is the atomic valence or group number of each constituent element in the alloy. For alloys with multiple TL, TE, M, or N constituents - like Fe-Co based alloys, alloys featuring both Nb and Zr growth inhibitors, or alloys featuring both Si and B metalloids – Eq. 5.2.1 must be further expanded with the respective stoichiometric concentration and group number of each additional constituent.

At an atomic level, The *Density of States*, $g(\varepsilon)$ and denoted DoS, represents the number of electron states as a function of energy level, ε, in a materials. In this way the number of valance electrons per atom in an element or alloy, *N*, can also be obtained by summing the number of filled valance states, that is integrating the density of valance states from the zero of energy, taken as $-\infty$, to the *Fermi* Energy, ε_F.

$$N = \int_{-\infty}^{\varepsilon_F} g(\varepsilon)\, d\varepsilon \,. \qquad \text{Eq. 5.2.2}$$

Similarly, the spin-split DoS, $g^{\uparrow}(\varepsilon)$ and $g^{\downarrow}(\varepsilon)$, represent the number of states per atom as a function of energy for each the spin up and spin down, respectively, valance electrons of a material with the number of spin up or spin down electrons given by the respective integrations.

$$N^{\uparrow} = \int_{-\infty}^{\varepsilon_F} g^{\uparrow}(\varepsilon)\, d\varepsilon \qquad \text{and} \qquad N^{\downarrow} = \int_{-\infty}^{\varepsilon_F} g^{\downarrow}(\varepsilon)\, d\varepsilon \,. \qquad \text{Eq. 5.2.3}$$

Summing the spin-split states yields the total number of valance electrons as in Eq. 5.2.1,

$$\begin{aligned} N &= N^{\uparrow} + N^{\downarrow} \\ &= \int_{-\infty}^{\varepsilon_F} \left(g^{\uparrow}(\varepsilon) + g^{\downarrow}(\varepsilon) \right) d\varepsilon \,. \\ &= \int_{-\infty}^{\varepsilon_F} g(\varepsilon)\, d\varepsilon \end{aligned} \qquad \text{Eq. 5.2.4}$$

Because each electron exhibits a magnetic moment, μ_B, the difference between the two sums of spin-split states yields the magnetization, μ, of the material, or the net magnetic moment per atom,

$$\begin{aligned}\mu &= N^{\uparrow} - N^{\downarrow} \\ &= \int_{-\infty}^{\varepsilon_F} \left(g^{\uparrow}(\varepsilon) - g^{\downarrow}(\varepsilon) \right) d\varepsilon \end{aligned} . \qquad \text{Eq. 5.2.5}$$

Like the atomic valance, N, it can be seen that several material properties, like atomic magnetic moment, are directly related to the density of states. This is why fundamental treatment of the electronic structure of materials is so powerful an analysis tool for analysis of materials properties.

Electrical Resistivity can also be related to the electronic structure of materials. From the mean free path scattering theory which produced Eq. 5.1.1 it has been shown that the mean free path, λ, or inversely τ, is proportional the square of a scattering potential, V_{scat}, and the population of the most energetic filled states, that is value of the DoS at the Fermi Level, $g(\varepsilon_F)$:

$$\begin{aligned}\rho &= \left(\frac{m}{nq^2\tau} \right) = \left(\frac{mv}{nq^2\lambda} \right) \\ &\propto \left| V_{scat} \right|^2 g(\varepsilon_F) \end{aligned} . \qquad \text{Eq. 5.2.6}$$

For spin-split systems, both the up and down bands act as independent paths through which conduction electrons can diffuse and as such they are added in parallel in Eq. 5.2.6 such that [67], [68],

$$\rho = c \frac{g^{\uparrow}(\varepsilon_F) \cdot g^{\downarrow}(\varepsilon_F)}{g^{\uparrow}(\varepsilon_F) + g^{\downarrow}(\varepsilon_F)} . \qquad \text{7Eq. 5.2.7}$$

Another property of interest that is easy related to the DoS is the *Cohesive Energy, E_{Coh}*. For a given energy band centered at, ε_i for {i=s, p, d, etc.} the Cohesive Energy is the integrated product of the proximity to the band center and the DoS, i.e.

$$E_{Coh} = \int_{-\infty}^{\varepsilon_F} (\varepsilon - \varepsilon_d) \cdot g(\varepsilon) d\varepsilon . \qquad \text{Eq. 5.2.8}$$

Local and Total Density of States

Because the DoS characterizes the atomic structure of materials, if different atomic species are present in an alloy for example consideration must be given to each unique atomic configuration. (In some cases

differences in atomic environment for even the same species of atom must even be considered). In this way, the DoS of Eqs. 5.2.3 - 5.28 can be regarded as the *total density of states*, made up of contributions of each atomic configuration, with its own *local density of states,* $g_{loc}(\varepsilon)$. Or,

$$g_{tot}(\varepsilon) = \frac{1}{N_{atoms}} \sum_{atoms} g_{loc}(\varepsilon) \qquad \text{Eq. 5.2.9}$$

For this study of the effect of Virtual Bound States due to dilute 3d Early Transition metal impurities in Co-based nanaocomposites we can consider the DoS of the host, $g_{host}(\varepsilon)$, and that of the 3d metal impurity, $g_{imp}(\varepsilon)$. And for alloys, $Co_{1-Y}TE_Y$, approximated to be binary as explained in the subsequent section Eq. 5.2.9 is comprised to two sums, one over the host atoms and another over the impurity atoms, and the total density of states becomes simply the weighted sum of the host and impurity DoSs,

$$\begin{aligned} g(\varepsilon) &= \frac{1}{N_{atoms}} \left[\sum_{host} g_{host}(\varepsilon) + \sum_{imp} g_{imp}(\varepsilon) \right] \\ &= \frac{1}{N_{atoms}} \left[N_{host} g_{host}(\varepsilon) + N_{imp} g_{imp}(\varepsilon) \right], \\ &= (1\text{-Y}) g_{host}(\varepsilon) + \text{Y} g_{imp}(\varepsilon) \end{aligned} \qquad \text{Eq. 5.2.10}$$

while respecting spin-splitting, i.e.

$$g^{\uparrow\downarrow}(\varepsilon) = (1\text{-Y}) g^{\uparrow\downarrow}_{host}(\varepsilon) + \text{Y} g^{\uparrow\downarrow}_{imp}(\varepsilon) . \qquad \text{Eq. 5.2.11}$$

Consequently, Eq.5.2.4 becomes,

$$N = (1\text{-Y}) \left[\text{N}^{\uparrow}_{host} + \text{N}^{\downarrow}_{host} \right] + \text{Y} \left[\text{N}^{\uparrow}_{imp} + \text{N}^{\downarrow}_{imp} \right], \qquad \text{Eq. 5.2.12}$$

and the magnetic moment, Eq. 5.2.5 becomes,

$$\mu = (1\text{-Y}) \left[\text{N}^{\uparrow}_{host} - \text{N}^{\downarrow}_{host} \right] + \text{Y} \left[\text{N}^{\uparrow}_{imp} - \text{N}^{\downarrow}_{imp} \right]. \qquad \text{Eq. 5.2.13}$$

Finally, the electrical resistivity of such an alloy and Eq. 5.2.7 become,

$$\rho = c \left[\frac{\left[(1-Y) g^{\uparrow}_{h}(\varepsilon_F) + Y g^{\uparrow}_{imp}(\varepsilon_F) \right] \cdot \left[(1-Y) g^{\downarrow}_{h}(\varepsilon_F) + Y g^{\downarrow}_{imp}(\varepsilon_F) g^{\downarrow}(\varepsilon_F) \right]}{(1-Y) \left[g^{\uparrow}_{host}(\varepsilon_F) + g^{\downarrow}_{host}(\varepsilon_F) \right] + Y \left[g^{\uparrow}_{imp}(\varepsilon_F) + g^{\downarrow}_{imp}(\varepsilon_F) \right]} \right] \qquad \text{Eq. 5.2.14}$$

5.3 3d Impurities in Late Transition Metal Alloys

Materials properties including induced anisotropy[33], [69], [70], magnetostriction[71]–[73], electrical resistivity[67], [74]–[76], and magnetic moment are sensitive to amount and species of Early Transition metal (TE) additives in amorphous and nanocomposite materials, and properties in these systems are often optimized by TE alloying[11], [32], [77]. Giant strain induced anisotropy in the Co-based alloy, $Co_{70}Fe_4TE_4Nb_4Si_2B_{14}$ for TE={V, Cr, Mn}, are shown in Fig 5.2.1 in which the effects of early transition metal additives on properties are very pronounced. The effects of dilute 3d TE on electronic structure and properties in Late Transition metal (TL) based alloys has been well ascribed to the formation of Virtual Bound States (VBS) in several such crystalline systems[78]–[85]. However, explanation of similar phenomena in amorphous alloys is complicated because first principle band structure calculations of amorphous-multicomponent alloys is very limited[67], [86]–[89]. Here, we apply features of VBS containing band structures that have been observed in similar dilute TE doped crystalline systems to rigid approximations of both the crystalline and amorphous band structure of Cobalt. We note that dependence and change of properties with dilute TE additions can be primarily ascribed to changes due to the impurity VBS. The simplified electronic structure can explain observed experimental trends in moment, resistivity, and induced anisotropy well.

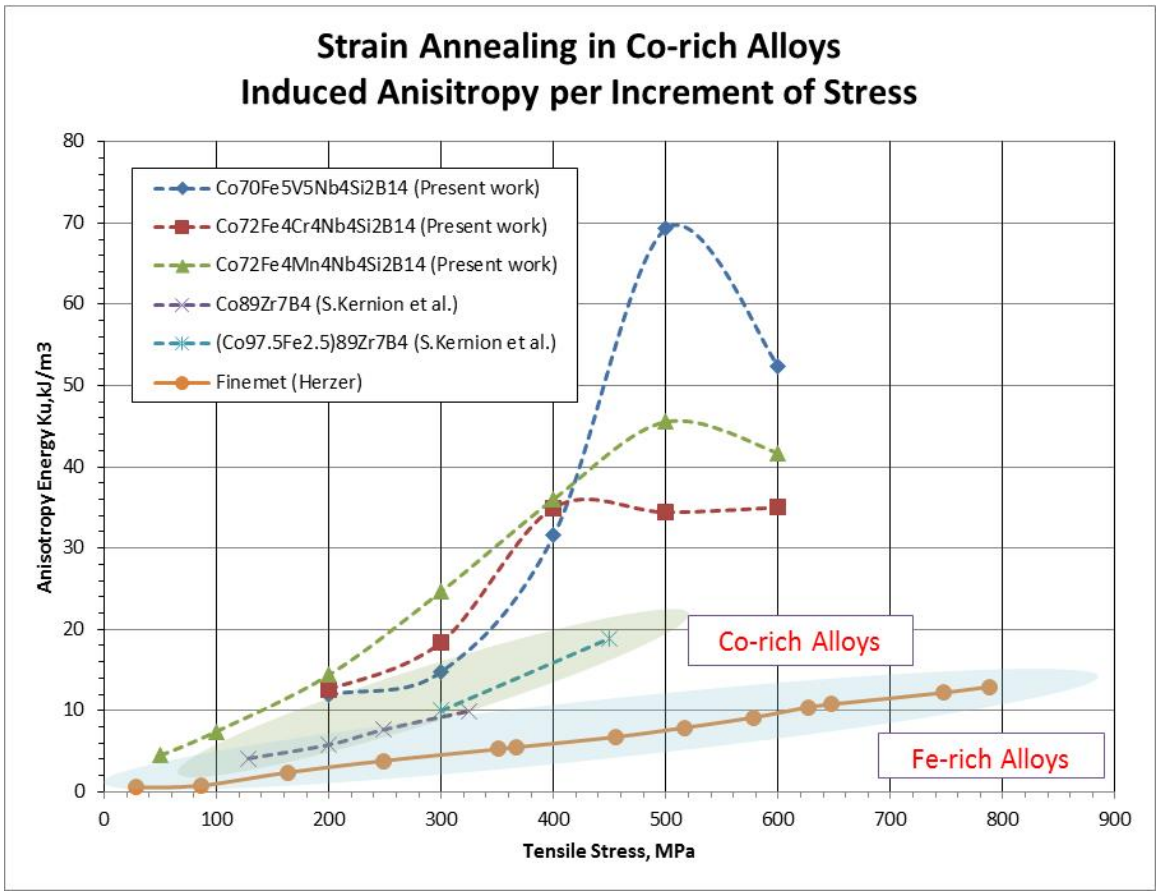

Figure 5.2.1: Comparison of strain induced anisotropy versus tensile stress applied during annealing shows that Co-based materials selectively alloyed with early transition metal additives leads to an order of magnitude increase in induced anisotropy over conventional Fe-based MANCs, and more the three times increase over other Co-based alloys.

5.3.1 Formation and Trends of Virtual Bound States due to Early Transition Metal Doping

The theory describing the formation of Virtual Bound States due to impurities in transition metal alloys was first formulated by Freidel and has since been expanded and refined by several others including Kondo and Anderson whose work on localized states received the Nobel prize in Physics in 1977[78], [86], [90]–[92]. The theory considers a perturbation in the free electron gas of metal or alloy due to an impurity atom of nuclear charge, Z_{imp}, which differs from the host charge, Z_{host}, by an amount $\Delta Z = Z_{host} - Z_{imp}$. The mobile carriers of the conduction band of the host locally *screen* the charge difference in the proximity of the impurity atom. For dilute (non-interacting screening charge typical for less than 10at% impurity) 3d impurities in transition metal alloys this buildup of screening charge causes a phase shift, η, in the wave function solutions of the alloy at the impurity[93],

$$\tan\eta_l(\varepsilon) = \frac{W_l}{\varepsilon - \varepsilon_d} \qquad \text{Eq. 5.3.1}$$

where W is the characteristic band width and ε_d and ε are the are the energies of the 3d band and screening electrons respectively. This phase shift is a function of the energy of the electrons making up the conduction band and is related to the impurity screening charge, ΔZ , by the Friedel Sum Rule[78], [94], [95],

$$\Delta Z = \frac{2}{\pi}\sum_{l}(2l+1)n_l(\varepsilon)\,. \qquad \text{Eq. 5.3.2}$$

The left side of Eq. 5.3.1 can further be expressed as the density of states for the impurity species being screened, i.e.

$$\Delta Z = 2\int_{\varepsilon=0}^{\varepsilon_F}\Delta g_{imp}(\varepsilon)d\varepsilon\,. \qquad \text{Eq. 5.3.3}$$

This results in the familiar impurity Lorentzian, Virtual Bound State density of states for the 3d impurity,

$$g_{imp}(\varepsilon,\varepsilon_d,W,I) = I\left[\frac{W^2}{\left(\varepsilon-\varepsilon_d\right)^2+W^2}\right] \qquad \text{4Eq. 5.3.4}$$

in which ε is the position of the d levels of the impurity, and W is the width of the Lorentzian, and is related to the sd hybridization potential by, $W=V_{sd}Z$[83], [96].

5.3.2 Trends in Virtual Bound States

Having established the Lorenztian DoS characteristic of VBS in this section we enumerate some of the particulars features of these states including, VBS position, width, and height, and spin-splitting and ferromagnetic or anti-ferromagnetic exchange coupling with the host.

VBS Position, Width, and Height

The first and most straightforward property of 3d impurity VBSs is the position, ε_d , of the band which mirrors that of the elemental 3d transition metals. In particular, within the same period of the periodic table the position of the 3d band increases with group number, i.e. $\varepsilon_{d,V} < \varepsilon_{d,Cr} < \varepsilon_{d,Mn} < \varepsilon_{d,Fe} < \varepsilon_{d,Co}$ and so on for the 3d transition metals. In my analysis tabulated values of ε_d compiled from the literature consisting of both experimental and theoretical considerations were used[97].

The width and height of the characteristic Lorentzian VBS DoS also trend with group number. Firstly, it is noted that the integrated intensity of the VBS DoS equals related to the number of valance electrons of the impurity. The integral of the entire Lorentzian DoS, from $-\infty$ to ∞, is equal to 10, the total number of electrons the 3d band can accommodate. And the integral of the filled or occupied VBS DoS, from $-\infty$ to ε_F, is the valance charge of the impurity, Z_{imp}. These two constraints relate the Width, W, and Height, I, of the VBS DoS such that,

$$\begin{aligned} 10 &= \int_{-\infty}^{\infty} g_{imp}(\varepsilon, \varepsilon_d, W, I) d\varepsilon \\ &= IW \arctan\left(\frac{\varepsilon - \varepsilon_d}{W} \right) \Big|_{e=-\infty}^{\infty} \end{aligned} \qquad \text{Eq. 5.3.5}$$

which implies

$$IW = \frac{10}{\pi} . \qquad \text{Eq. 5.3.6}$$

The constraint at the Fermi level yields,

$$\begin{aligned} Z_{imp} &= \int_{-\infty}^{\varepsilon_F} g_{imp}(\varepsilon, \varepsilon_d, W, I) d\varepsilon \\ &= \frac{10}{\pi} \arctan\left(\frac{\varepsilon - \varepsilon_d}{W} \right) \Big|_{e=-\infty}^{\varepsilon_F} \end{aligned} \qquad \text{Eq. 5.3.7}$$

which implies the constraint on the Lorentzian width,

$$\frac{\pi}{10} Z_{imp} = \arctan\left(\frac{\varepsilon_F - \varepsilon_d}{W} \right) \text{ or } W = \frac{(\varepsilon_F - \varepsilon_d)}{\tan\left(\frac{\pi}{10} Z_{imp} \right)}, \qquad \text{Eq. 5.3.8}$$

and height by substituting into Eq. 10,

$$\begin{aligned} IW &= \frac{10}{\pi} \Rightarrow \\ I &= \frac{10}{\pi} \frac{\tan\left(\frac{\pi}{10} Z_{imp} \right)}{(\varepsilon_F - \varepsilon_d)} . \end{aligned} \qquad \text{Eq. 5.3.9}$$

So, for the same host the width varies along a series of impurities as shown in Fig. 5.3.2 being primarily dependent on Z_{imp}, that is the impurity dopant. The general trend, as has been previously reported, is that the Lorentzian VBS width, W, increases, with impurity valance Z_{imp} along a given period, and the concomitant intensity, I, decreases with Z_{imp}[96]–[98]. Perhaps more conveniently, with respect to the host-impurity charge difference $\Delta Z = Z_{host} - Z_{imp}$, as ΔZ increases in going from Mn, to Cr, to V added to Co, the Lorentzian width, W, increases and the Lorentzian height, I, decreases.

VBS Hybridization, Spin-Splitting and Exchange

Virtual Bound States due to 3d impurities have been studied in ferromagnetic hosts, as their behavior in these systems differs from nonmagnetic systems like Al [83], [96], [98]. Anisimov details the spin splitting and exchange energies of 3d impurities including V, Cr, and Mn in ferromagnetic hosts[97]. He records that like the host, impurity bands in these systems also spin-split and each V, Cr, and Mn exhibit negative exchange coupling with the host in stable configurations. The negative exchange coupling has effects both on the overall magnetic moment of the alloy and on sd hybridization in the impurity.

Friedel et. al. demonstrated the spin splitting of VBS added to Copper by measuring the resistivity. The double peak demonstrates that the VBS is spin split, with each peak corresponding to a peak of the up/down VBS states passing through the host Fermi level[78]. Beckmann et. al. fit this data to a green theory KKR calculation quite successfully[94].

Attention thus far has been given to the electronic structure of the 3d electrons of the transition metal impurities. It must be noted that the s electrons of these impurities must also be considered. Many authors have treated this problem in detail [79], [84], [90], [97], noting that the extent of hybridization of 4s and 3d bands varies with the system of 3d impurities in transition metal hosts. The amount of overlap between the two bands, and the extent to which each is filled are primary determining facts. As such, for minority impurity bands that lie almost entirely below the Fermi level, as is the case for V, Cr, Mn in Co (and Fe), the minority impurity bands hybridize more than the majority bands. In this model, the sd hybridization in the impurity band structure

is treated by simply adding the Lorentzian 3d VBS band to a top hat 4s band for both the minority and majority bands, their sum being the total density of states for the impurity species, as shown in Fig. 5.3.3.

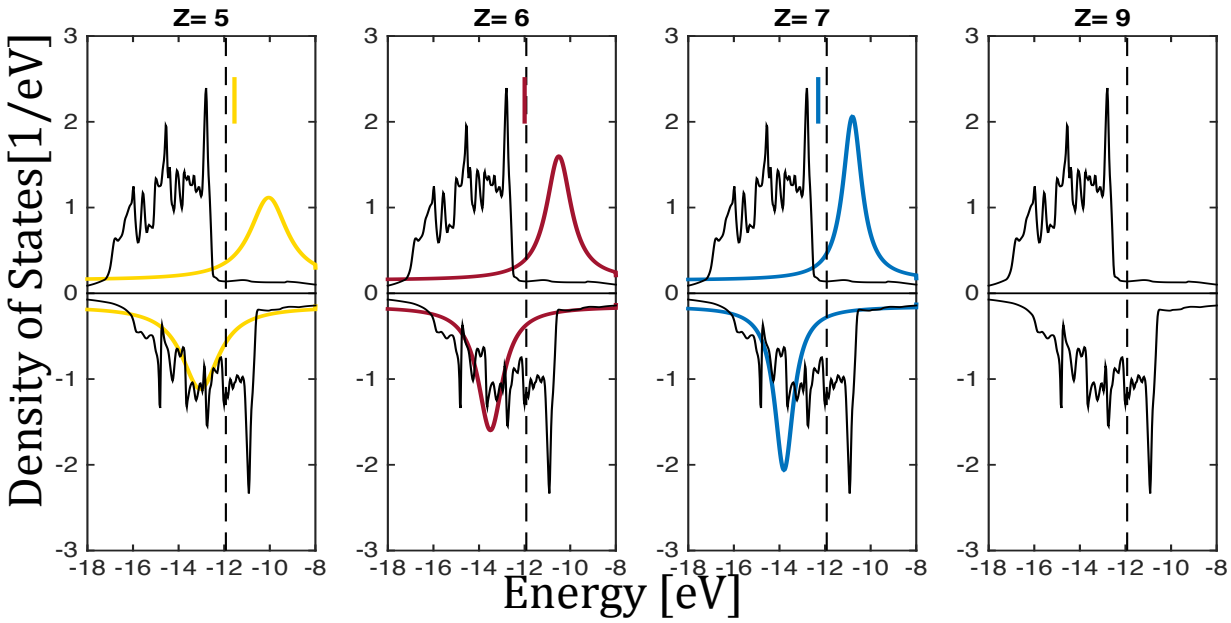

Fig. 5.3.3: Schematic Virtual Bound States due to Early Transition Metal additions, V, Cr, Mn (Z=5,6,7) to ffc Cobalt (Z=9) host band structure. VBS located near the Fermi Energy and which shift position and shape with ΔZ lead to increases in resistivity and decreases in magnetic moment consistent with those observed in the Co-based series.

5.4 Results for 3d Impurity VBSs in Co alloys

The previously described trends in Virtual Bound States due to dilute 3d metal impurities in a Cobalt host were implemented in MATLAB. The Density of States for Co as tabulated by P. Hadley was used for the host [99], [100]. The constructed VBS DoS was numerically integrated up to the Fermi level for each spin state consistent with Eq. 5.3.7. The result of Eq. 5.2.5 for the local magnetic moment of the impurities are shown in Fig. 5.3.4. Impurities that show two values for local moment (Mn and Fe) are those for which Anisimov reported both the antiferromagnetic and ferromagnetic solutions to be stable.

From the local moment shown in Fig. 5.3.4 the total magnetic moment for the $Co_{1-Y}TE_Y$ alloys is calculated using Eq. 5.2.8 and the results are shown in Fig. 5.3.5, for Y=2at%. Not surprisingly the same trend in moment is observed across the TE series, however the change in magnetization is centered about $\mu = 1.6\mu_B$, the magnetic moment of the Co host.

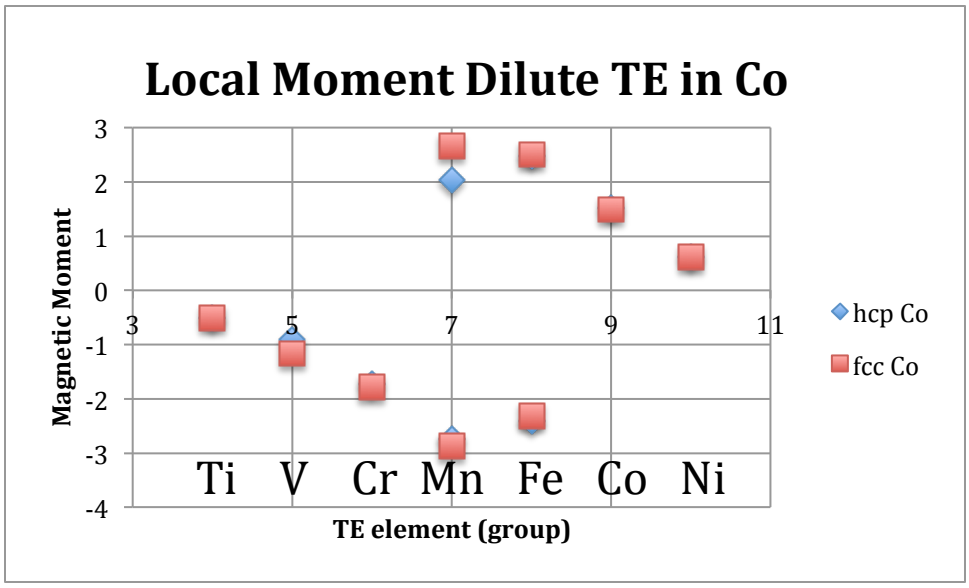

Figure 5.3.4: Local moment of impurity 3d transition metals in a Co host, show that for impurities in which $\Delta Z > 1$, i.e. Ti, V, Cr, and Mn, antiferromagnetically coupled VBS form which decrease the magnetic moment inversely with ΔZ, consistent with Anismov, Friedel, and Anderson.

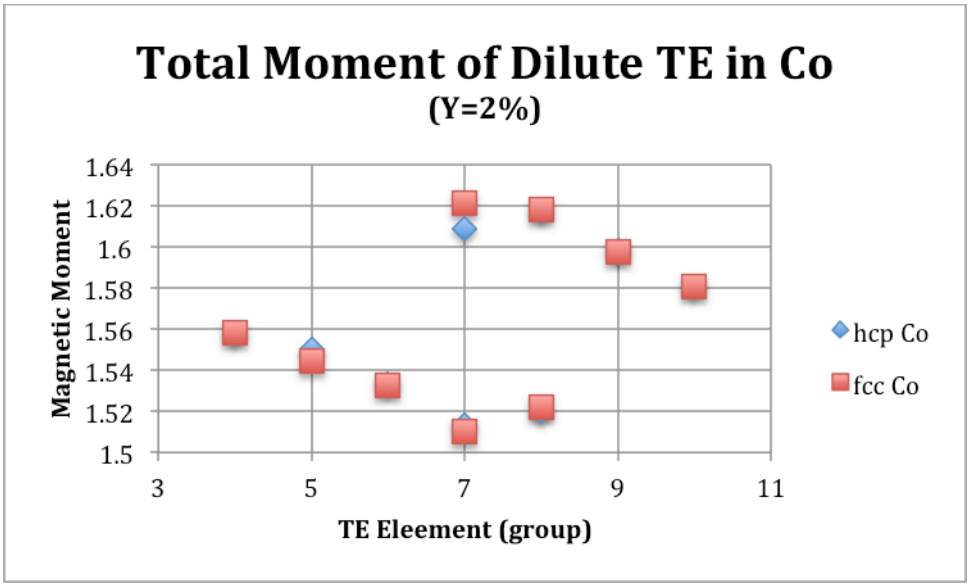

Figure 5.3.5: The total magnetic moment of $Co_{1-Y}TE_Y$ alloy simulated with VBS due to the 3d metal impurity.

The magnetic moment across a reproduction of the entire $Co_{70-Y}Fe_4TE_YNb_4Si_2B_{14}$ for TE={Ti, V, Cr, Mn} Y={0-8at%} series is shown in Fig. 5.3.6 - moment vs. TE content - and in Fig. 5.3.7(a) – moment vs. average number of electrons per atom. Because magnetic moment is a straightforward calculations from the band structure and is thoroughly tabulated for these alloy systems these plots act as a convincing check on the validity of the approximations used throughout this analysis. For example, the developed VBS model more than adequately reproduces the trends with 3d early transition metal additions to both Co and Fe featured on the well established Slater-Pauling curve

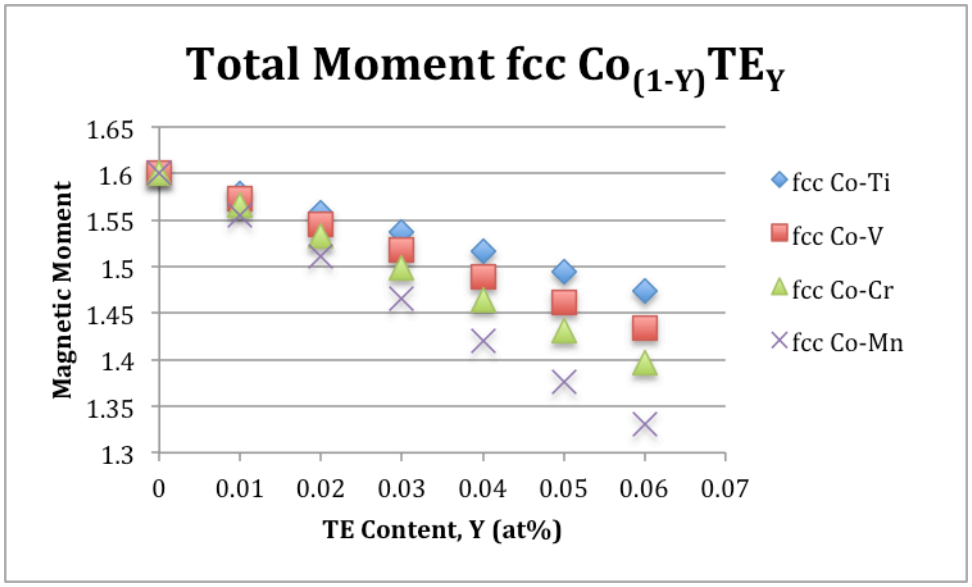

Figure 5.3.6: The total magnetic moment across the $Co_{70-Y}Fe_4TE_YNb_4Si_2B_{14}$ for TE={Ti, V, Cr, Mn} Y={0-8at%} series shows that the 3d metal impurities always act to decrease the Co-based alloy's moment with impurities with larger Z having the greatest effect.

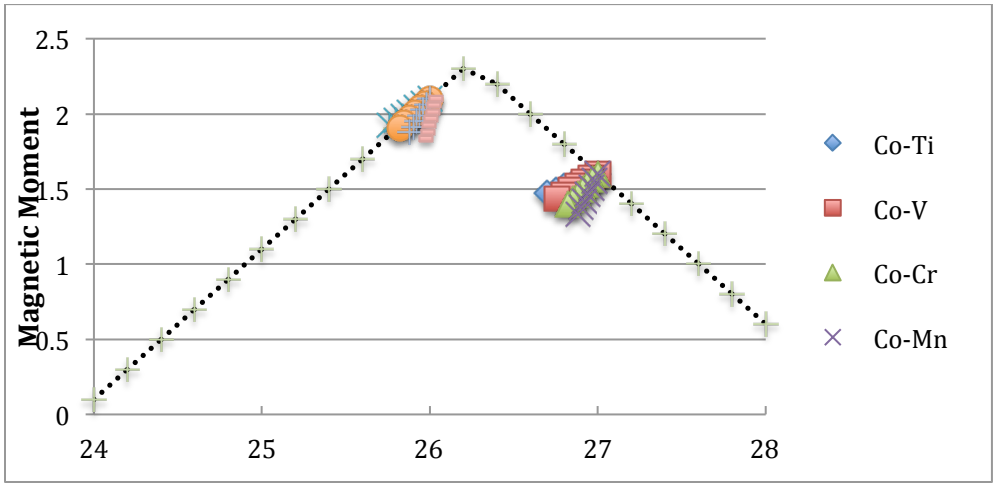

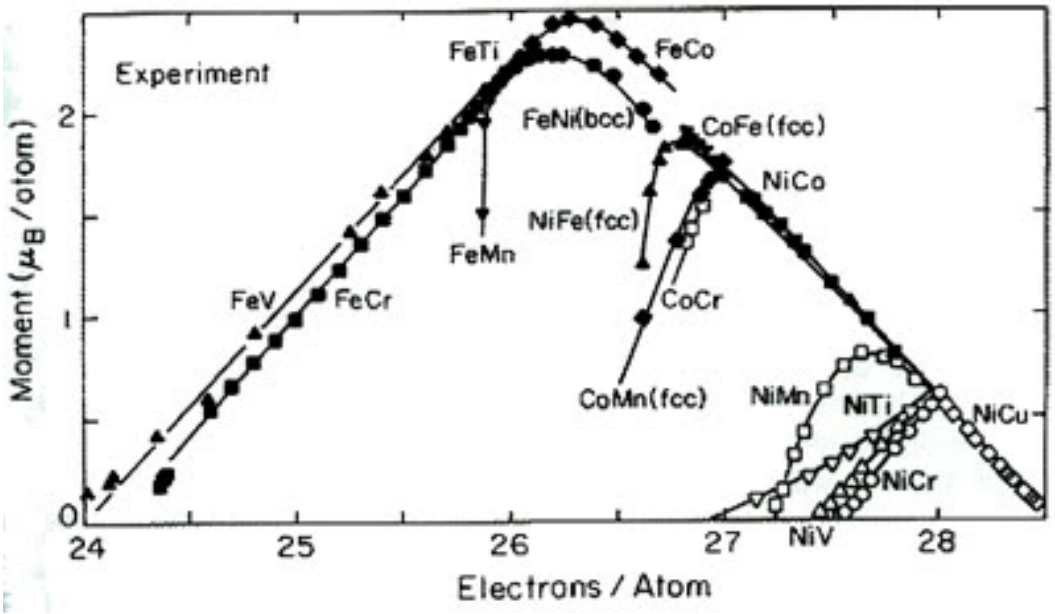

Figure 5.3.7(a): The same data for magnetic moment across the $Co_{70-Y}Fe_4TE_YNb_4Si_2B_{14}$ for TE={Ti, V, Cr, Mn} Y={0-8at%} series plotted verses average number of electrons per atom so as to reproduce the trends exhibited on the well established Slater Pauling Curve below **(b)**.

Having established credibility for the developed VBS model for 3d impurities in Co we discuss the simulated electrical resistivity and cohesive energy. The experimentally measured resistivity versus TE content, Y, for the $Co_{70-Y}Fe_4TE_YNb_4Si_2B_{14}$ for TE={Ti, V, Cr, Mn} Y={0-8at%} series is shown in Figure 5.3.8(a). The increase in resistivity with both dopant (as ΔZ increases) and with TE content is pronounced. Consistent with experimental observations, the simulated band structure superimposing the VBS DoS onto the Co band structure reproduces the nearly linear trend with TE content, Y=0-6at%, for each of the three dopants, V, Cr, and Mn. Moreover, the greatest increase in resistivity is exhibited by dopants with increasing ΔZ . That is, the Vanadium doped alloy lead to a larger electrical resistivity than the Cr doped alloy, than the Mn doped alloy.

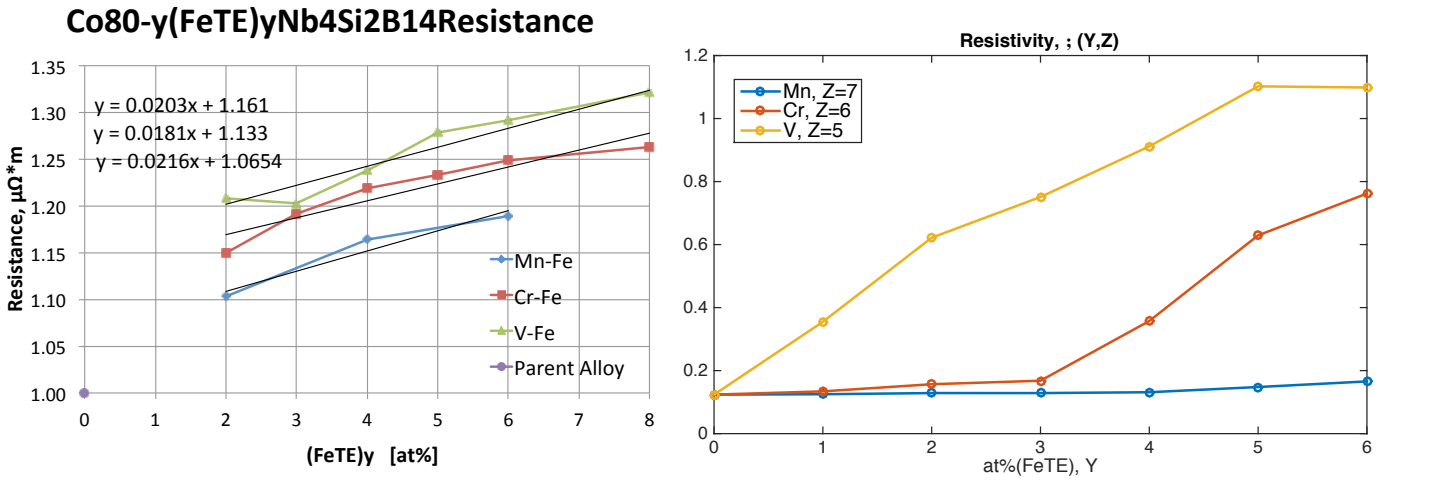

Figure 5.3.8: Experimental **(a: left)** and simulated **(b: right)** results of the electrical resistivity of the $Co_{70-Y}Fe_4TE_YNb_4Si_2B_{14}$ for TE={V, Cr, Mn} Y={0-8at%} alloy series show nearly linear trends in resistivity with TE content, Y, and the largest increase in resistivity for dopants with larger ΔZ , i.e. V, then Cr, then Mn.

Conclusions

In conclusion the high electrical resistivity is one of the principal properties which make magnetic amorphous and nanocomposite materials so well suited for high frequency switching applications including magnetic motors. Their inherently large electrical resistivity come both from the large amount of chemical and structural disorder present in these amorphous, multicomponent alloys. Additionally, selective alloy can exploit the additional increases in resistivity due to the formation of Virtual Bound States due to just small amounts of Early Transition metal elements in these materials. The $Co_{70-Y}Fe_4TE_YNb_4Si_2B_{14}$ for TE={V, Cr, Mn} Y={0-8at%} series illustrates the profound effect selective additions to MANC alloys can have on material properties, including but not limited to induced anisotropy, magnetic moment, and electrical resistivity.

Chapter 6: Multiphase Model of Electrical Resistivity in Magnetic Nanocomposites

6.0 Multiphase Model of Resistivity in Magnetic Amorphous Nanocomposites

The consequences of the chemical partitioning of glass formers in this materials system are not limited to nanostructure. As noted in the previous chapter, many properties of this class of materials are dependent on local composition. And still more are indirectly dependent on local composition through their dependence on the nanostructure. For instance, properties like coercivity and its power law dependence on grain size [4], correlate more closely to nanostructure. Others, like magnetostriction [71], [101] or Curie Temperature[39], are sensitive to small variations in composition and are less dependent on structure. Magnetic permeability has been shown to have dependencies on both composition and structure. [72], [102]

Like permeability, electrical resistivity in MANCs depends both on local composition – for instance doping with Si increases the resistivity of FINEMET – and composite nanostructure – crystallization decreases resistivity for most all amorphous alloys. This chapter examines the electrical conductivity, and concomitant resistivity, of these nanocomposite materials, specifically treating this property's dependence on the crystallization state of the material and local glass former concentration.

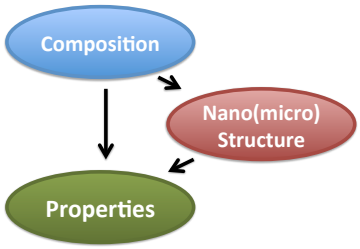

Fig. 6.0.1 Schematic illustrating that composition determines many properties both directly, and indirectly by controlling composite nanostructure.

This chapter summarizes and contextualized the work published in:

- "Multiphase Resitivity Model for Magnetic Nanocomposites Developed for High Frequency, High Power Transformaion." V. DeGeorge, S. Shen, P. Ohodnicki, M. Andio, and M. McHenry. *Journal of Electronic Materials*. (2013) [103]

6.1 Electrical Resistivity and Multiphase Model

Having noted the composite structure of these materials, the chemical partitioning of elements, and the different resistivity due to each of these solving for the effective resistivity, or total resistance, of these composites is seen to be a multiphase problem. The effective nanocomposite electrical resistivity, that is net resistance per representative cross-sectional area, is described by the model developed by DeGeorge et. al. [103] Where description of this model does not require being abridged or modified excerpts from this manuscript are reprinted directly here.

The intrinsic resistivity of the crystalline phase, ϱ_{xtl}, is considerably lower than that of the metallic glass matrix due both to its crystallinity and because it is largely depleted of high scattering glass former elements. As noted in the previous chapter the large Growth Inhibitor, GI, early transition metal elements, i.e. Zr, Nb, W, Ta, Hf, etc, are largely insoluble in the crystalline phase which therefore is comprised almost entirely of Fe, Co and Si [49]. In this model crystalline resistivity, ϱ_{xtl}, is assumed as the bulk resistivity value of the host metal. For instance for Cobalt based alloys this is, $\varrho_{xtl} = \varrho_{Cobalt} = 74\mu\Omega cm$.

Oppositely, the intrinsic resistivity of the amorphous phase, ϱ_0, of the nominal, as-cast alloy composition that is rich in glass formers and is structurally disordered, is considerably higher than the crystalline phase. The previous chapter outlines attempts to approximate this value theoretically, but here this value is taken from experimental determination of resistivity of As-Cast ribbon, which for typical Co-based ribbon ranges from, $80 < \varrho_{am} < 150\mu\Omega cm$.

The MANC mass balance describes how the GI concentration of the amorphous phase increases with crystallization either by remaining homogenous (no shell) or by accommodating a GI composition gradient, approximated by the shell formulation. By the Virtual Bound State arguments this increase in GI concentration leads to increased resistivity of either the whole amorphous phase or the high GI concentration shell. Therefore, the resistivity of this interfacial amorphous phase, ϱ_{shell}, will always be larger than ϱ_0.

Therein, this multiphase effective resistivity model accounts for contributions of $\varrho_{shell} > \varrho_{am} > \varrho_{xtl}$ from each the shell, amorphous, and crystal phases to the overal resistivity. As shown in fig. 6.1.1, because the crystalline phase is embedded within the amorphous phase the low resistivity path through crystallites requires

that current traverse the higher resistivity amorphous matrix in going from crystallite to crystallite. If the amorphous phase exhibits a GI concentration gradient, or shell, this notion is further compounded. As will be demonstrated the existence of a shell ensures that the effective composite resistivity is not independent of crystal grain size, and is instead is related to interfacial (crystal/amorphous) surface area, which is a function of each crystal volume fraction, crystallite size, and nucleation density.

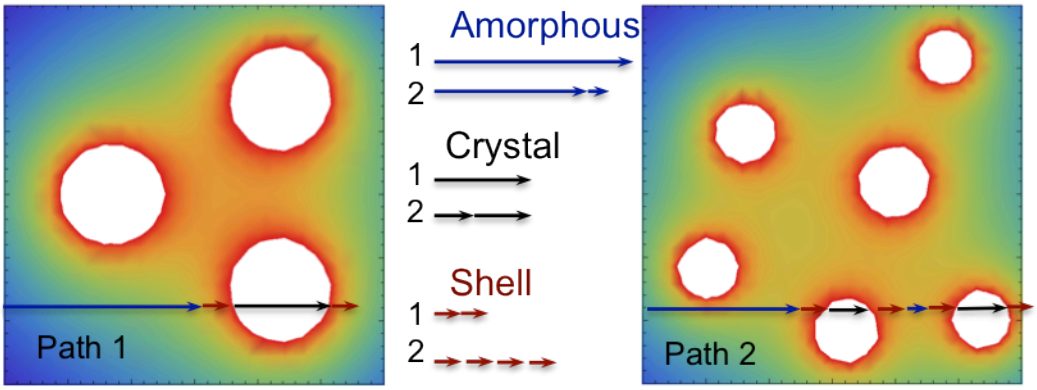

Fig. 6.1.1 Schematic growth inhibitor concentration profile with a high growth inhibitor concentrated shell surrounding low GI concentration crystals in composite systems with equal crystal volume fractions. Larger nucleation density (right) leads to more interfacial area and increased resistivity because on average current traversing the composite will encounter more high resistivity shell, less as-cast amorphous phase, and equal crystal phase than in a material with lower nucleation density (left).

6.2 Multiphase Formalism

A common approach to addressing electric resistivity in composite materials has been to consider the two "phases" as being in electrical contact in either a parallel or series circuit configuration. This approach was developed by Oring [104] and extended to a variety of composite materials systems. In each system, the configuration with the two phases oriented in parallel acts as a lower bound for the composite resistivity. This is because in this assumption there is always a path through the low resistivity phase continuously traversing the sample. Oppositely, the series configuration bounds the composite resistivity above[105]. By extending Oring's multiphase formalism from two to three phases an equivalent circuit is constructed considering the path current must take through a cross section of nanocomposite ribbon. Particular consideration must be given to the fact that the high resistivity shell completely surrounds each portion of the crystal phase.

A unit volume, in which a volume fraction, V_{xtl}, is occupied by crystalline particles of characteristic size, s, is partitioned into N equivalent sub-volumes, so that N is the number, or nucleation, density of crystalline particles, $N=V_{xtl}/s^3$. A cross-section orthogonal to the current flow of one such 1/N sub-volume is shown in Fig. 6.2.2 and depicts parallel paths (denoted with a superscript "∥") current must take through the nanocomposite. Similarly, series paths (denoted with a superscript "⊥") are described by considering a sub-volume cross-section *in* the plane of current flow. The equivalent circuit for the sub-volume, shown in Fig. 6.2.2b, is constructed. In nanocomposites with isotropic nucleation there are $N^{1/3}$ of these sub-volumes in series and $N^{2/3}$ in parallel leading to an equivalent, effective nanocomposite resistivity, $\varrho_{eq}=r_{eq}$ in which,

$$\frac{1}{r_{eq}}N^{1/3}=\frac{1}{r_{am}^{\parallel}}+\left(\left(\frac{1}{r_{shell}^{\perp}+r_{xtl}^{\perp}}+\frac{1}{r_{shell}^{\parallel}}\right)^{-1}+r_{am}^{\perp}\right)^{-1} \qquad \text{Eq. 6.2.1}$$

The extrinsic resistance, r_i^h, of each of the $h=\{//, \perp\}$ configurations and the $i=\{am, xtl, shell\}$ phases is related to its intrinsic resistivity, ϱ_i, through that phase's volume fraction by,

$$r_i^h=\rho_i\frac{l_i}{a_i}, \qquad \text{Eq. 6.2.2}$$

in which l_i and a_i are the appropriate length parallel to and area perpendicular to current flow through each phase. For instance, in one sub-volume the crystal comprises a volume, $V_{xtl}/N=a_{xtl}l_{xtl}$, and contributes no parallel

resistance, $r_{xtl}^{\parallel} = 0$ (because there is only one crystallite in each sub-volume). Therefore, for isotropic crystals in which $l_{xtl} = (a_{xtl})^{1/2} = s$, the only contribution from the crystal is $r_{xtl}^{\perp} = \rho_{xtl} \frac{s}{s^2}$.

Then, for the parallel contributions of the shell and amorphous phases, a_i and l_i are related to the crystal fraction through the shell depth, d. For instance,

$$r_{shell}^{\parallel} = \rho_{shell} \frac{l_{shell}}{a_{shell}} = \rho_{shell} \frac{s+2d}{(s+2d)^2 - a_{xtl}} \qquad \text{and} \qquad r_{am}^{\parallel} = \rho_{am} \frac{l_{am}}{a_{am}} = \rho_{am} \frac{1/N}{1/N - a_{xtl} - a_{shell}}.$$

Eq. 6.2.3 and Eq. 6.2.4

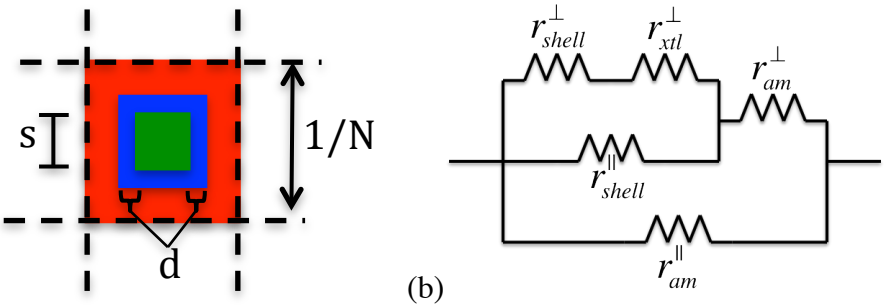

Fig. 6.2.2: **(a)** Schematic of cross-sectional area of a sub-volume of the nanocomposite ribbon. Cross sectional areas for the crystal, shell, and residual amorphous phases are shown in green, blue and, red respectively. **(b)** The equivalent circuit for the three phase nanocomposite system accounting for the series, $r_i^{\perp}$, and parallel, $r_i^{\parallel}$, contributions of the shell, crystal, and amorphous (i=shell, xtl, am) phases.

This multiphase formalism has been implemented using Mathematica in which the resistivity of each phase, ϱ_{shell}, ϱ_{am}, and ϱ_{xtl}, shell depth, d, and either of the crystal fraction, V_{xtl}, nucleation density, n, or crystal size, s are input variables. Varying one of the other variables, V_{xtl}, n, or s, while maintaining that the crystal volume fraction, crystallite size, and nucleation density are related by, $ns^3 = V_{xtl}$, the nanostructural dependence of a MANC's effective resistivity is calculated. General output demonstrating the capabilities and predictions of the model are shown in Fig. 6.2.3.

It is important to note that the scenarios simulated in Fig. 6.2.3a-c are carried out under the over assumption that crystal volume fraction, V_{xtl}, shell depth, d, particle size, s, and shell resistivity, ϱ_{shl}, are independent of one another. While such an assumption is instructive in conceptually demonstrating the dependencies of resistivity on these parameters, in fact d, V_{xtl}, s, and ϱ_{shl} are not independent but are instead related by the mass balance detailed in Chapter 4, a constraint which was applied for each of the other results using the multiphase model.

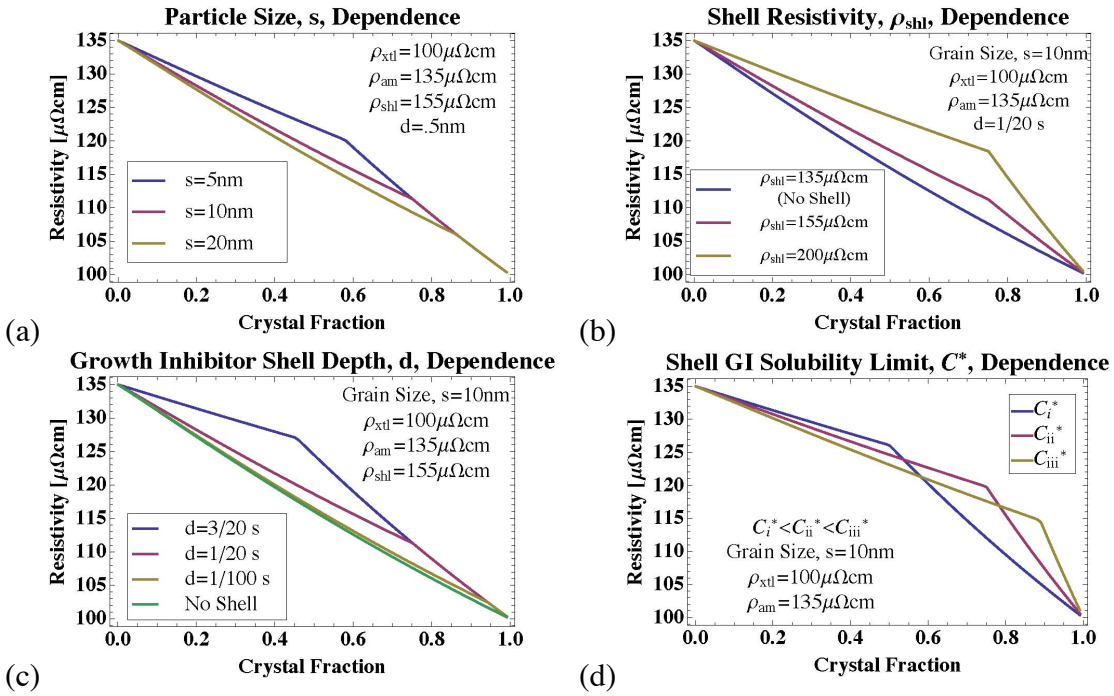

Figure 6.2.3 (a) Smaller crystallite sizes, s, **(b)** increased resistivity, ϱ_{shell}, of high Growth Inhibitor concentration shell and **(c)** increased shell depth, *d*, all lead to larger effective nanocomposite resistivity. Particle size and Shell depth also affect final crystal fraction of the nanocomposite. Shell resistivity and Shell depth both depend on GI concentration in the shell, the competing effects of which are demonstrated in **(d)** in which a GI mass balance constraint is placed on the system.

Fig. 6.2.3a shows the model eliciting particle size dependence as shown conceptually in Fig. 6.2.1. For a given volume fraction, V_{xtl}, and constant shell depth, d, a greater number of smaller particles leads to more interfacial area and therefore a larger effective resistivity. Fig 6.2.3a also demonstrates a second feature of the model, a characteristic "bend" or "knee." In this model, this knee occurs when neighboring particles' shells overlap and begin to impinge on one another and corresponds physically to the well established "soft impingement" phenomenon which halts crystal growth when neighboring crystallites' composition profiles overlap and saturate the residual amorphous phase with GI species. It shows itself as an abrupt decrease, bend, or knee, in the effective resistivity in this simulation, a feature that should be regarded as the "final" or "full" volume fraction to which the composite system will grow, for instance after long annealing times. The model predictions for crystal fractions after this knee should not be considered as physically meaningful as the GI mass does not balance in this region, and physically crystals will not grow beyond this soft impingement limit.

We note that as exhibited in Fig 6.2.3a this final crystal fraction shifts to lower values with decreasing particle size, *s*, when *s* is considered as independent. This is explained by the notion that for the same shell depth the shells of more numerous, small particles will impinge on one another at a smaller total crystal fraction

than that at which the shells of less numerous, large particles impinge on one another. Investigation of this final volume fraction shift constrained to the growth inhibitor mass balance is discussed hereafter.

Fig. 6.2.3 (b) and (c) illustrate the (competing) effects that the two defining features of the high growth inhibitor shell - shell depth, d, and intrinsic shell resistivity, ϱ_{shell} - have on the nanocomposite's net effective resistivity. Fig. 6.2.3 (b) shows a larger ϱ_{shell} leads to a larger effective nanocomposite resistivity. In the non-mass balanced scenario the final crystal fraction is not dependent on ϱ_{shell}. Also worth noting for comparison sake is the case when $\varrho_{shell}=\varrho_{am}$. This is the case when the high GI shell has the same resistivity as the as-cast amorphous alloy, which is the trivial case when there is no high GF shell and which reduces to Oring's simple two-phase composite formalism.

Fig. 6.2.3(c) illustrates that the effect of the shell depth, d, on the nanocomposite resistivity of the nanocomposite is two fold. Firstly, as might be expected, a larger shell depth, d, increases the effective resistivity of the nanocomposite. Again we can compare the shell model to that without a shell by considering the case in which $d=0$, which is a lower bound for all finite shell depths. Secondly, it can be seen that the final crystal fraction takes smaller values as shell depth increases. This can be expected as, when considering equi-sized particles, those with larger surrounding shells will impinge on one another sooner than those with smaller surrounding shells as the crystallites grow with increasing crystal fraction. This effect becomes significant if applications require a minimum crystal fraction, however again a mass balance relating d, s, V_{shl}, and ϱ_{shl} is necessary to more completely describe this effect.

Finally we comment on the physical cause and the competition between the two previously mentioned features that act to maximize a nanocomposite's effective resistivity. Both the depth of the shell and its intrinsic resistivity are determined primarily by the concentration of GIs in the shell, defined to be the solubility limit of GIs in the amorphous phase, C^*. Moreover, we note that these are competing effects. A larger C^*, i.e. a shell with a higher concentration of GIs, will lead to a larger intrinsic resistivity, ϱ_{shell}. However, a higher concentration of GI in the shell will take up less room, or have a smaller shell depth, d, than a shell with a lower

C^*. Thus, the GI concentration of the alloy is one of the main controls in the problem of optimizing resistivity in these MANC systems.

We begin approaching this problem is by considering the GI mass balance between the crystalline, shell, and amorphous phases and an intrinsic resistivity of the shell phase, ϱ_{shell}, which is proportional to C^*. We assume zero solubility of GIs in the crystalline phase, $C_{xtl}=0$. Then the particle size, s, and the volume and depth, d, of the shell can be related to the crystal fraction transformed, f_{xtl}, through the GI concentrations as described previously. Here, the dependence of the resistivity of the amorphous shell on GI concentration described in the previous chapter is assumed approximated as proportional to the GI concentration of this phase, C^*. The results are shown in Fig. 6.2.4.

Having related both defining features of the shell, d and ϱ_{shell}, to C^* so that they are no longer independent the competing effects previously described can be better explained. The final crystal fraction transformed, indicated by the knee, is shifted to higher crystal fractions as C^* increases while the effective resistivity of the nanocomposite is lessened.

6.3 Application of the Multiphase Model

Here we apply the multiphase resistivity model to two MANC alloys. The first comparison is a FINEMET type alloy, HTX002, which was prepared and reported by S. Kernion et. al. but for which we have little knowledge of the GI concentrations, C_0, C_{xtl}, and C* [11]. The second comparison is from a more recent Co-based Mn alloy series, for which Atom Probe Tomography was performed so more precise knowledge of these GI concentrations as well as the resistivities, ϱ_{xtl}, ϱ_{am}, *and* ϱ_{shell}, are available.

FINEMET System:

Fig. 6.3.1 shows predictions of the model compared to experimental results for a FINEMET type alloy. MANC resistivity was determined by four probe measurement of ribbon annealed to difference crystal fractions using the spiral method ribbon method. Structural properties were determined using conventional XRD analysis. For samples annealed at increasing temperatures for one hour, particle size was approximated by analyzing Scherrer peak broadening. Approximate volume fraction was determined by monitoring the development of the first three crystal diffraction peaks assuming the final volume fraction of the last annealing treatment before observation of secondary crystallization was 0.9 at which first signs of secondary crystal product were observed.

Experimental data is presented alongside output of the multiphase model from large and small particles under the assumption of independent particle size because in practice crystal size is not constant with growth but instead grows with crystal fraction. Additionally crystallites are not perfectly monodisperse, but instead exhibit a distribution of particle sizes. More precise structural parameters can be determined by utilizing higher resolution characterization techniques including more advance X-ray techniques, TEM, Magnetometry and others. As-cast resistivity of the amorphous phase, ϱ_{am}, was measured to be 135μΩcm.

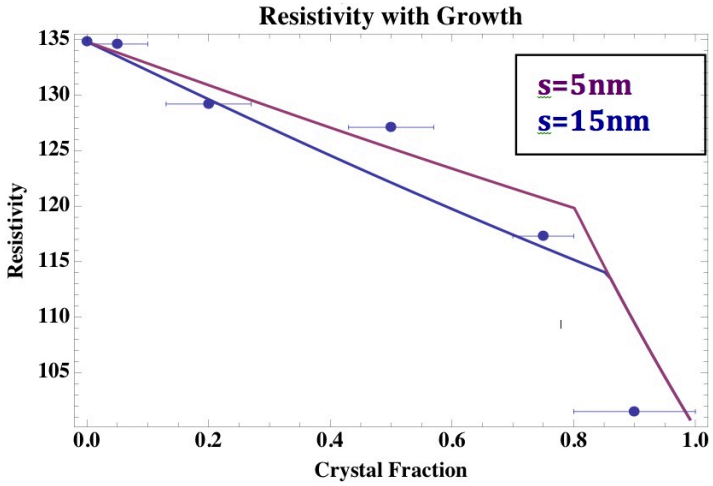

Fig. 6.3.1: Comparison of multiphase resistivity model to experimental data for FINEMET type FeCo nanocomposite. The model for two different crystallite sizes, s, are show. The resistivities of the crystal, amorphous, and shell phases were taken as ϱ_{xtl}=100, ϱ_{am}=135, and ϱ_{shell} = 150 μΩcm respectively.

HTX005, $Co_{1-2X}Nb_4(FeMn)_XSi_2B_{14}$, System

The resistivity of As-Cast amorphous alloy belonging to the series $Co_{1-2X}Nb_4(FeMn)_XSi_2B_{14}$, designated HTX005, with 0<x<6, is shown in Fig. 6.3.2a. Atom Probe Tomography was also performed on this alloy series so more complete knowledge of the concentration of GI is known for this alloy. The observed sample had an FeMn concentration $X=C_0$=2.3at%Mn, and was confirmed by APT. The corresponding resistivity of this as-cast amorphous phase was extrapolated from the fit of Fig. 6.3.2 to be, $\varrho_{am} = 108$μΩcm. APT of a partially devitrified sample of this alloy revealed a crystal volume fraction, V_{xtl}=0.55 and average crystal size, s = 8nm, which was also confirmed through TEM. Using the mass balance equation $V_{xtl}=(C^*-C_0)/(C^*-C_{xtl})$ and assuming the crystalline phase to be completed depleted of Mn, we solve for C*=5.11at%Mn and note that the sample has not grown to its final crystal fraction as samples prepared with 6at%Mn show that Mn is still further soluble in the amorphous phase. A final crystal fraction of 0.7 yields C*=7.6at%Mn, which is indeed larger than the greatest Mn concentration from which amorphous ribbon could be prepared. This value, C*=7.6at%Mn was used in the multiphase analysis and corresponds to an interfacial resistivity, $\varrho_{shell} = 126.9$μΩcm . The values for each of the input variables for the multiphase analysis of this MANC are shown in table 6.3.1.

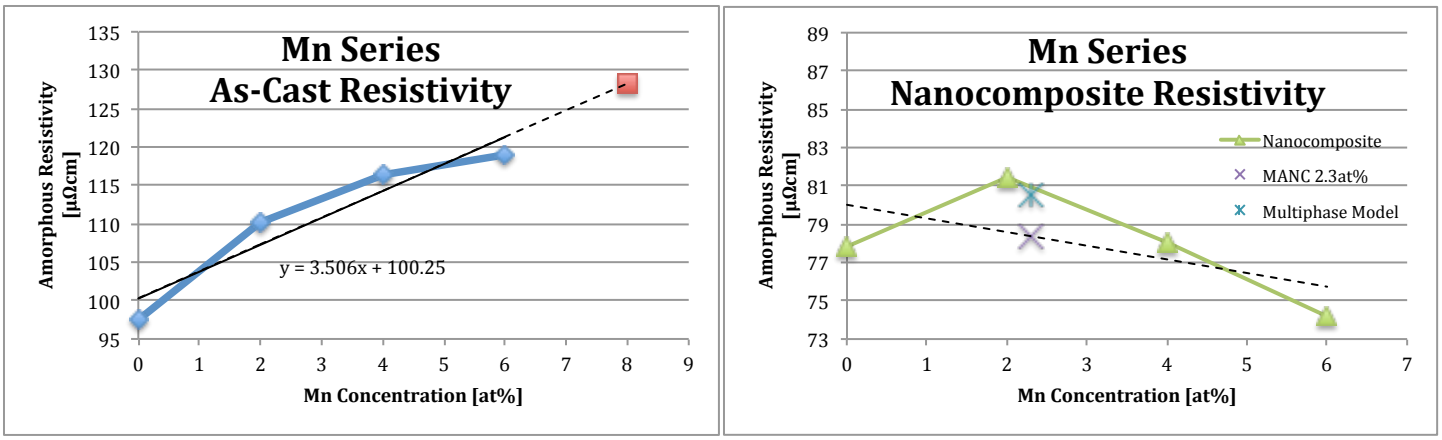

Figure 6.3.2 (a) Resistivity of As-Cast Amorphous Co-Mn alloy, with extrapolation to 7.6at%Mn. (b) Resistivity of partially crystallized Co-Mn MANC, also showing interpolated composite resistivity at 2.3at%Mn and that calculated from the multiphase model with inputs from APT experiments.

Semi-empirical Assumptions of Analysis					
Mn Concentration in at%Mn of Amorphous, Crystalline, and Interface			Resistivity in μΩcm of each of the composite phases, Amorphous, Crystalline, and Interface		
C_0	**C_{xtl}**	**C***	**ϱ_{Am}**	**ϱ_{xtl}**	**ϱ_{shell}**
2.3	0	5.11	108	64	126.9
Synthesis + APT	Synthesis + ATP	ATP + Modeling	Experiment	Literature	Extrapolation

Table 6.3.1 Input variables for the multiphase MANC resistivity model determined experimentally through APT and application of the chemical partitioning mass balance model for GI concentration and by four probe measurement and extrapolation of the results of the amorphous alloy for the respective resistivities of each phase.

The resistivity verse crystal fraction results of the multi-phase resistivity model for these inputs are shown in Fig. 6.3.3. The two experimentally measured resistivity values for this composition, the as-cast and V_{xtl}=0.55 nanocomposite, are also indicated on this plot. Composite resistivity for crystal fractions above the final crystal fraction are shown by a dashed line. The multiphase model predicts an equivalent composite resistivity value, ϱ_{eq}=*80.5*μΩcm, which agrees with the experimentally observed value, 78.45μΩcm, to within 2.8%.

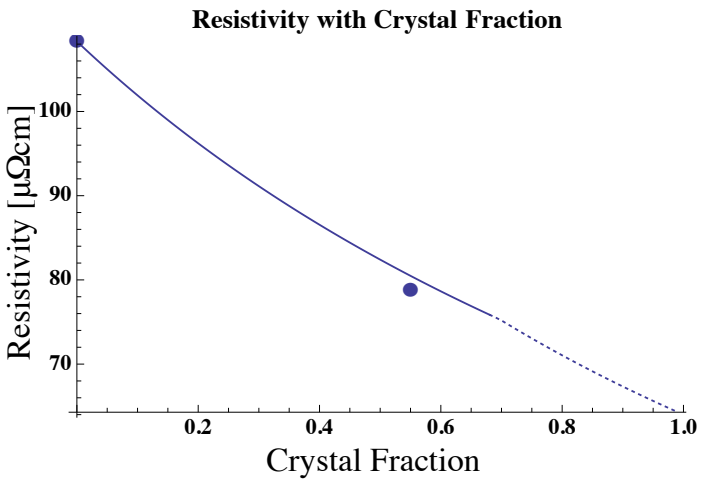

Figure 6.3.3 Results of the multiphase composite resistivity model are plotted for the input variables listed in table 6.3.1. The experimentally measured resistivity values are also shown for the as-cast amorphous phase and nanocomposite with crystal fraction V_{xtl}=0.55m for which the model and experiment agree to within 2.8%.

Summary

The multiphase resistivity model developed here draws from the previously described mass balance and GI concentration dependence of each phase's intrinsic resistivity and integrates these into a model which accounts for the complex composite structure of magnetic amorphous nanocomposites. The model represents a useful extension of Oring's original formulation of the resistivity of nanocomposites, by integrating the high resistivity interfacial phase consistent with the mass balance. Comparison between the model and experiment can help in guiding the development of new alloys – for instance with alloys for electric motors in which resistivity is a chief design consideration. This model can also be helpful in characterizing the properties of the nanocomposite system that are not easily determined directly through experiment. i.e. C^*, ϱ_{shell}, etc. As demonstrated, another of the main strengths of this model is its ability to span chemical systems. For instance, nanocomposite systems like Fe-Si-Nb-B and Fe-Zr-B which exhibit similar nanostructure but different amorphous and effective resistivities can still be compared via this model accounting for their similarities *and* differences. Moreover, the semi-empirical model can be further improved by recursively refining it through experimental characterization of the nano-structure, electrical, and magnetic properties in order to improve input parameters and check the underlying assumptions of the model.

Chapter 7 Future Work

7.1 MANC Alloys and Processing for Motors

7.1.1 Alloys

As-based Finemet-like materials were among the first to be developed and commercialized these have been the primary material of choice in efforts to integrate MANCs into motors. Within this light, two trends are noticeable in these efforts:

I) Fe-based compositions - no specialized/tailored compositions featured in prototype motor,

II) Purely amorphous materials, not nanocomposites. To date I have not found evidence in the literature that a nanocomposite material has been used in a motor or electric machine.

Mechanical properties, particularly brittleness, limit in Fe-based nancomposite materials in electric machines, however other compositions, including Co-based or Co-contining alloys, demonstrate more robust mechanical properties.

After granting the mechanical properties requirements, thermal stability is the main motivator for this line of investigation as nanocomposite materials are considerably more stable to higher temperatures, leading to heightened operation temperature range - in the range of >300C instead of <300C – in electrical machines. That nanocomposites tend to demonstrate larger Magnetic Inductions while maintaining magnetic softness is also an advantage.

7.1.2 Processing

One of the more significant findings confirmed in the CMU, UCB collaboration and C2M project and report was the identification of core material processing - the shaping of core material, which is often laminates, into core geometries - as one of the main obstacles in integrating MANCs into electric machines. Interviews with technical personnel (See Chapter 2) identified processing as one of the chief engineering obstacle to integrating MANCs into motors, as conventional processing techniques used on electrical steels are not readily feasible. The increased hardness of amorphous materials was identified as the chief materials property complicating these efforts.

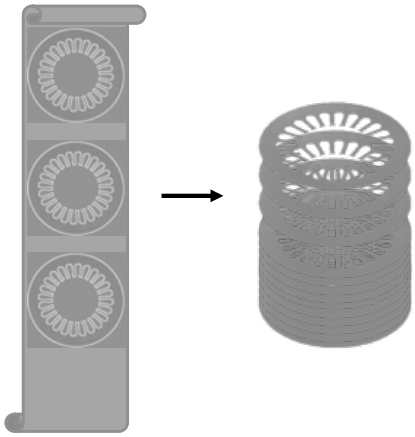

Figure 7.1 A schematic illustrating how a magnetic core can be constructed from stacking laminates of a magnetic core material that have been stamped from either laminates (of Si-Steel) or amorphous ribbon.

Three of the processing techniques that have garnered the most attention include:
1) Stamping 2) Laser Cutting 3) Water-jet Cutting

Stamping: Stamping is the conventional processing technique used to achieve core geometries for Si-steels. It is low cost, scaled well to commercial sizes, and is effective in achieving core geometries from steel laminates. However, stamping is not feasible amorphous and nanocomposite materials. Early efforts revealed that the hardness of, particularly Fe-based, amorphous materials limited the process specifically due to the excessive wearing of stamping dyes (See Chapter 2 and C2M report).

Laser cutting: Laser cutting, in which a high power laser is used to cut metals, has been proposed as possible core material shaping technique. J. Silveyra et. al. and other groups have demonstrated the technique and found it feasible.[106] However, very high local heating at the cutting edge of magnetic material due to laser compromises material properties at these edges. Some analysis has been done to investigate the extent of the damage but the sacrifice of material properties and device performance detract from the merits of the technique.

Water-jet cutting: In light of the damage to heat sensitive material due to local heating water-jet cutting, in which a tremendously high speed, highly focused, and high pressure jet of water cuts material, has emerged as promising magnetic core material shaping technique. This technique has been demonstrated in some very successful prototype motors featuring MANC materials.[31] The water-jet is powerful enough to cut through several layers, ~100, of ribbon at once and still produce a clean edge. This also allows for ribbon to be wound

first and cut after having been wound. Moreover, there is very little to no local heating, approaching the thermal stability limits of the material, induced by the water-jet cutting so edges are not compromised as in laser cutting. It appears that water-jet cutting is the most promising processing technique for shaping magnetic amorphous and nancomposite materials that has been identified to date.

7.2 Thermal Conductivity

Also identified in the IEA report, is the thermal transport and cooling of motors as having the potential to most improve efficiency in motors. Efficiently preventing and removing heat from motors is particularly important because as losses are inherent in these machines heat is released. If this heat cannot be adequately removed from the machine it remains and increases the device temperature to the point of operation beyond the thermal stability limits of the device. Local heating is also particularly important for the magnetic core material within a motor as magnetic properties can be both temporarily and permanently compromised by even short times at elevated temperatures.

Moreover, in addition to practical device operation considerations the scientific question of thermal transport in MANCs is as interesting if not more so than the electrical transport properties. Often in materials, especially in metals, electrical transport and thermal transport are related. Particularly when free electrons are the dominant mechanism of both electric and thermal transport, as in most metals, then the Wiedemann-Franz Law relates the electrical conductivity and the thermal conductivity. When free electrons are not the dominant mechanism and lattice vibrations also contribute to thermal and electric transport the connection between the two is considerably more complicated. That there is no crystal structure in amorphous materials adds another significant consideration to this problem in that lattice vibrations cannot be expected as in crystalline materials. Thus, as electrical conductivity is a multiphase problem dealing with all crystalline and amorphous phases and their boundary, so is thermal conductivity. It is an exciting problem in that by having studied electrical conductivity well, one might expect that thermal conductivity is easily extrapolated through the Wiedemann-Franz law, however the validity of the dominant free-electron transport mechanism is seriously called into question particularly in the amorphous phase. Thus the question of thermal conductivity presents an intricate and exciding scientific problem both theoretically and experimentally as well as practically and operationally for device applications.

The purpose of this section is to explore the validity of the Wiedemann-Franz Law in these MANC alloys that relates the electrical and thermal conductivity of materials in which free electrons are the dominated mode of heat transfer. Understanding of thermal transfer has significance in its effects on

performance, through heat dissipation during device operation, as well as scientifically understanding of the mode(s) of heat transfer in the multi-phase composite as can be elucidated through the temperature dependence of the thermal conductivity.

It is well known that electrical conductivity and thermal conductivity are intimately related in many material systems, particularly metals. Along with electrical resistivity, because thermal conductivity is an important application design parameter in both power converter and electric machine applications, in terms of dissipating thermal energy due to losses, the applicability of the previous multiphase electrical resistivity model to thermal resistivity is explored.

For materials in which the dominant mechanism of heat transfer is free electrons, and not say lattice vibration, i.e. phonons, or atomic collisions, as in gasses, thermal and electrical conductivity are related via the Wiedemann-Franz Law,

$$\frac{\kappa}{\sigma} = LT \quad \text{or} \quad L = \frac{\kappa}{\sigma T} \qquad \text{Eq. 7.2.1}$$

where $\varkappa$ is the thermal conductivity, σ is the electrical conductivity, T, is the absolute temperature and L is the Lorenz number and is a constant.

The value of the Lorenz number can obtained by considering expressions for electrical and thermal conductivities in the Fermi-Dirac formalism of the electron gas:

$$\text{Electrical:} \qquad \sigma = \frac{ne^2\lambda}{mv_f} \qquad \text{Eq. 7.2.2}$$

$$\text{Thermal:} \qquad \kappa = \frac{\pi^2 k_B^2 nLT}{3mv_f} \qquad \text{Eq. 7.2.3}$$

in which n is the number density of free electrons, e is the electron charge, v_f is the Fermi velocity, λ, is the electron mean free path, and k is the Boltzmann constant, and m is the effective mass of the electrons. The ratio of $\varkappa$ to σ can be constructing yielding the value for the Lorenz constant,

$$L = \frac{\kappa}{\sigma T} = \frac{\pi^2 k_B^2}{3e^2} = 2.45 \times 10^{-8} \, W\Omega/K^2 \qquad \text{Eq. 7.2.4}$$

Based on the electrical conductivities observed in these MANC's the thermal conductivity of these materials can be predicted using the Wiedemann-Franz Law. Predicted thermal conductivities for the three

phases and the effective composite are shown in Table 7.2.1. In collaboration with Prof. John Malen's thermal transport group the thermal conductivity of the Nb series MANC is being measured. The extent of agreement with the Wiedemann-Franz predictions offer insight into the validity of the assumption that free electrons are the dominant mode of heat transfer in these composites.

	Electrical Resistivity, ϱ [μΩcm]	Electrical Conductivity, $\varkappa$ [1/Ωm]	W.F. Predicted Thermal Conductivity, σ [W/mK]
Crystalline	10	1.0×10^7	98.0
Amorphous	130	7.7×10^5	7.5
Shell	150	6.7×10^5	6.5
Effective Composite	100	1.0×10^6	9.8

Table 7.2.1 Typical electrical resistivities, electrical conductivities, and thermal conductivities predicted by the Wiedemann-Franz law at room temperature for each the crystalline, amorphous, and shell phases, and the net composite effective.

In all the investigation of thermal transport and thermal conductivity in magnetic amorphous and nanocomposite materials is motivated by both practical engineering considerations – of removing heat and maintaining operation with thermal limitation - and scientifically – in acswering questions of thermal transport mechanism in both amorphous and particularly nanocomposite multiphase materials.

Chapter 8 Bibliographic References

[1] D. E. Laughlin, M. A. Willard, and M. E. McHenry, "Magnetic ordering: some structural aspects," *Phase Transform. Evol. Mater.*, pp. 121–137, 2000.

[2] O. Gutfleisch, M. A. Willard, E. Brück, C. H. Chen, S. G. Sankar, and J. P. Liu, "Magnetic materials and devices for the 21st century: Stronger, lighter, and more energy efficient," *Adv. Mater.*, vol. 23, no. 7, pp. 821–842, 2011.

[3] A. Inoue, "STABILIZATION OF METALLIC SUPERCOOLED LIQUID," vol. 48, 2000.

[4] G. Herzer, "Grain structure and magnetism of nanocrystalline ferromagnets - Magnetics, IEEE Transactions on," *Structure*, vol. 25, no. 5, pp. 3327–3329, 1989.

[5] T. Pradell, D. Crespo, N. Clavaguera, and M. T. Clavaguera-Mora, "Diffusion controlled grain growth in primary crystallization: Avrami exponents revisited," *J. Phys. Condens. Matter*, vol. 10, no. 17, pp. 3833–3844, May 1998.

[6] Y. Yoshizawa, S. Oguma, and K. Yamauchi, "New Fe-based soft magnetic alloys composed of ultrafine grain structure," *J. Appl. Phys.*, vol. 64, no. 10, p. 6044, 1988.

[7] D. P. Urciuoli, T. E. Salem, and U. S. N. Academy, "New nanocrystalline core performance versus finemet ® for high- power inductors," vol. 4, 2007.

[8] S. Kernion, P. Ohodnicki, J. Grossmann, A. Leary, S. Shen, V. Keylin, J. F. Huth, J. Horwath, M. S. Lucas, and M. E. McHenry, "Giant induced magnetic anisotropy In strain annealed Co-based nanocomposite alloys," *Appl. Phys. Lett.*, vol. 101, no. 10, p. 102408, 2012.

[9] M. A. Willard, T. M. Heil, and R. Goswami, "Phase Formation in Isothermally Annealed (Co0.95Fe0.05)89Zr7B4 Nanocrystalline Alloys," *Metall. Mater. Trans. A*, vol. 38, no. 4, pp. 725–731, Apr. 2007.

[10] P. Ohodnicki, Y. L. Qin, D. E. Laughlin, M. E. McHenry, M. Kodzuka, T. Ohkubo, K. Hono, and M. A. Willard, "Composition and non-equilibrium crystallization in partially devitrified co-rich soft magnetic nanocomposite alloys," *Acta Mater.*, vol. 57, no. 1, pp. 87–96, Jan. 2009.

[11] S. Kernion, K. J. Miller, S. Shen, V. Keylin, J. Huth, and M. E. McHenry, "High Induction, Low Loss FeCo-Based Nanocomposite Alloys With Reduced Metalloid Content," *IEEE Trans. Magn.*, vol. 47, no. 10, pp. 3452–3455, Oct. 2011.

[12] J. Long, "FeCoB and FeZrSi-based Nanocomposite Soft Magnetic Alloys and Application," Carnegie Mellon University, 2008.

[13] G. Bordin, G. Buttino, A. Cecchetti, and M. Poppi, "Nanocrystallization of ferromagnetic Co-rich amorphous alloys and magnetic softening," vol. 2163, 1997.

[14] S. Kernion, P. Ohodnicki, and M. E. McHenry, "In-situ investigation of phase formation in nanocrystalline (Co97.5Fe2.5)89Zr7B4 alloy by high temperature x-ray diffraction," *J. Appl. Phys.*, vol. 111, no. 7, p. 07A316, 2012.

[15] M. Ohnuma, G. Herzer, P. Kozikowski, C. Polak, V. Budinsky, and S. Koppoju, "Structural anisotropy of amorphous alloys with creep-induced magnetic anisotropy," *Acta Mater.*, vol. 60, no. 3, pp. 1278–1286, Feb. 2012.

[16] J. M. Silveyra, A. Leary, V. DeGeorge, S. Simizu, and M. E. McHenry, "High speed electric motors based on high performance novel soft magnets," *J. Appl. Phys.*, vol. 115, no. 17, p. 17A319, May 2014.

[17] J. M. Silveyra, P. Xu, V. Keylin, V. DeGeorge, A. Leary, and M. E. McHenry, "Amorphous and Nanocomposite Materials for Energy-Efficient Electric Motors," *J. Electron. Mater.*, pp. 1–7, 2015.

[18] A. Chun, D. Hellebusch, P. Hogan, B. Li, D. Liu, C. Reed, M. E. McHenry, A. Leary, and V. DeGeorge, "Iron - Cobalt Based Magnetic Amorphous Nanocomposites for Smaller , Lighter , More Efficient , and More Powerful Electric Motors," 2014.

[19] S. Constantinides and J. Deleon, "Permanent Magneti Materials and Current Challenges," 2011.

[20] P. Waide and C. Brunner, "Energy-Efficiency Policy Opportunities for Electric Motor-Driven Systems," 2011.

[21] C. A. Smith, R. D. Belles, and A. J. Simon, “2007 Estimated International Energy Flows,” 2011.
[22] M. Doppelbauer, “IEC Motor Efficiency Classes,” 2012.
[23] A. Al-badi, A. Gastli, H. Bourdoucen, and J. Jervase, “Evolution of Axial-Field Electrical Machines,” pp. 227–245, 2000.
[24] D. J. Patterson, “Why Small Permanent Magnet Machine Drives are Relegating the Induction Machine Drive to Niche Applications,” *2005 Int. Conf. Power Electron. Drives Syst.*, vol. 1, pp. 1–8, 2005.
[25] E. Król and R. Rossa, “Modern Magnetic Materials in Permanent Magnet Synchronous Motors,” vol. 1, pp. 1–3, 2010.
[26] S. Baldwin, “The Materials Revolution And Energy-Efficient Electric Motor Drive Systems,” *Annu. Rev. Energy Environ.*, vol. 13, pp. 67–94, 1988.
[27] T. Fukao, A. Chiba, and M. Matsui, “Test Results on a Super-High-speed Amorphous-Iron Reluctance Motor,” vol. 2, no. 8823826, pp. 119–125, 1989.
[28] A. D. Hirzel, *Efficient High-Speed electric device using low-loss materials*, vol. 2, no. 12. 2007.
[29] R. Masaki, S. Morinaga, Y. Enomoto, H. Itabashi, M. Ito, and S. Tanigawa, “Development of an Axial Gap Motor With Amorphous Metal Cores,” *IEEE Trans. Ind. Appl.*, vol. 47, no. 3, pp. 1293–1299, May 2011.
[30] Y. Enomoto, H. Toloi, T. Imagawa, T. Suzuki, T. Obata, and K. Souma, “Amorphous Motor with IE5 Efficiency Class,” *Hitachi Rev.*, vol. 64, no. 8, pp. 480–487, 2015.
[31] N. Ertugrul, R. Hasegawa, W. Soong, J. Gayler, S. Kloeden, and S. Kahourzade, “A Novel Tapered Rotating Electrical Machine Topology Utilising Cut Amorphous Magnetic Material,” *IEEE Trans. Magn.*, vol. 9464, no. c, pp. 1–1, 2015.
[32] K. J. Miller, A. Leary, S. Kernion, a. Wise, D. E. Laughlin, M. E. McHenry, V. Keylin, and J. Huth, “Increased induction in FeCo-based nanocomposite materials with reduced early transition metal growth inhibitors,” *J. Appl. Phys.*, vol. 107, no. 9, p. 09A316, 2010.
[33] S. Shen, V. DeGeorge, P. Ohodnicki, S. Kernion, V. Keylin, J. F. Huth, and M. E. McHenry, “Induced anisotropy in FeCo-based nanocomposites: Early transition metal content dependence,” *J. Appl. Phys.*, vol. 115, no. 17, p. 17A335, May 2014.
[34] A. Leary, V. Keylin, A. Devaraj, V. DeGeorge, P. Ohodnicki, and M. E. McHenry, “Stress induced anisotropy in Co-rich magnetic nanocomposites for inductive applications,” *J. Mater. Res.*, vol. 31, no. 20, 2016.
[35] V. DeGeorge, E. Zoghlin, V. Keylin, and M. E. McHenry, “Time temperature transformation diagram for secondary crystal products of Co-based Co-Fe-B-Si-Nb-Mn soft magnetic nanocomposite,” *J. Appl. Phys.*, vol. 117, no. 17, p. 17A329, 2015.
[36] V. Degeorge, A. Devaraj, V. Keylin, J. Cui, and M. E. McHenry, “Mass Balance and Atom Probe Tomography Characterization of,” *IEEE Trans. Magn.*, vol. 51, no. 6, 2015.
[37] H. J. Guntherodt and A. Greer, *Metallic Glasses*, Fifth Edit., vol. 33, no. 7. Elsevier B.V., 1979.
[38] G. Wilde, *Physical Metallurgy of Nanocrystalline Metals*, Fifth Edit., no. 1984. Elsevier B.V., 2014.
[39] M. E. McHenry, M. A. Willard, and D. E. Laughlin, *Amorphous and nanocrystalline materials for applications as soft magnets*, vol. 44. 1999.
[40] T. Pradell, D. Crespo, N. Clavaguera, J. Zhu, and M. T. Clavaguera-Mora, “Kinetics of Microstructural Development in Nanocrystalline Materials.” 1997.
[41] K. Hono, “OVERVIEW NO . 133 ATOM PROBE MICROANALYSIS AND NANOSCALE MICROSTRUCTURES IN METALLIC MATERIALS,” vol. 47, no. 11, pp. 3127–3145, 1999.
[42] K. G. Pradeep, G. Herzer, P. Choi, and D. Raabe, “Atom probe tomography study of ultrahigh nanocrystallization rates in FeSiNbBCu soft magnetic amorphous alloys on rapid annealing,” *Acta Mater.*, vol. 68, pp. 295–309, Apr. 2014.
[43] Y. Zhang, K. Hono, A. Inouea, and T. Sakurai, “APFIM studies of nanocrystalline microstructural amorphous alloys evolution in FeZrB(Cu) Amorphous Alloys,” pp. 407–413, 1996.
[44] B. Gault, M. P. Moody, F. De Geuser, D. Haley, L. T. Stephenson, and S. P. Ringer, “Origin of the spatial

resolution in atom probe microscopy," *Appl. Phys. Lett.*, vol. 95, no. 3, pp. 93–96, 2009.
[45] H. S. Kitaguchi, M. P. Moody, H. Y. Li, H. E. Evans, M. C. Hardy, and S. Lozano-Perez, "An atom probe tomography study of the oxide-metal interface of an oxide intrusion ahead of a crack in a polycrystalline Ni-based superalloy," *Scr. Mater.*, vol. 97, pp. 41–44, 2015.
[46] K. Hono, K. Hiraga, Q. Wang, A. Inoue, and T. Sakurai, "The Microstructure Evolution of a Fe73.5Sil3.5B9Nb3Cu1 Nanocrystalline Soft Magnetic Material," vol. 40, no. 9, pp. 2137–2147, 1992.
[47] Y. Zhang, K. Hono, A. Inoue, A. Makino, and T. Sakurai, "Nanocrystalline STRUCTURAL evolution in Fe90Zr7B3 SOFT MAGNETIC MATERIAL," vol. 44, no. 4, pp. 1497–1510, 1996.
[48] J. D. Ayers, V. G. Harris, J. A. Sprague, and W. T. Elam, "On the role of Cu and Nb in the formation of nanocrystals in amorphous in amorphous FeNbCuSiB," vol. 974, no. 1994, pp. 10–13, 1994.
[49] D. H. Ping, Y. . Wu, K. Hono, M. A. Willard, M. E. McHenry, and D. E. Laughlin, "Microstructural characterization pf FeCpZrBCu nanocrystalline alloys," vol. 45, pp. 781–786, 2001.
[50] K. Hono, D. H. Ping, M. Omnuma, and H. Onodera, "Cu CLUSTERING AND Si PARTITIONING IN THE EARLY Crystallization Stage of An Fe73.5Si13.5B9Nb3Cu1 Amorphous Alloy," vol. 47, no. 3, pp. 997–1006, 1999.
[51] J. Long, P. Ohodnicki, D. E. Laughlin, M. E. McHenry, T. Ohkubo, and K. Hono, "Structural studies of secondary crystallization products of the Fe[sub 23]B[sub 6]-type in a nanocrystalline FeCoB-based alloy," *J. Appl. Phys.*, vol. 101, no. 9, p. 09N114, 2007.
[52] Y. Zhang, J. S. Blazquez, A. Conde, P. J. Warren, and A. Cerezo, "Partitioning of Co during crystallisation of FeÁ CoÁ NbÁ B (Á Cu) amorphous alloys," vol. 353, pp. 158–163, 2003.
[53] P. Ohodnicki, S. Y. Park, D. E. Laughlin, M. E. McHenry, V. Keylin, and M. A. Willard, "Crystallization and thermomagnetic treatment of a Co-rich Co–Fe–Ni–Zr–B–Cu based nanocomposite alloy," *J. Appl. Phys.*, vol. 103, no. 7, p. 07E729, 2008.
[54] M. E. McHenry, F. Johnson, H. Okamoto, T. Ohkubo, V. R. V. Ramanan, and D. E. Laughlin, "The kinetics of nanocrystallization and microstructural observations in FINEMET, NANOPERM and HITPERM nanocomposite magnetic materials," *Scr. Mater.*, vol. 48, no. 7, pp. 881–887, Apr. 2003.
[55] J. S. Blazquez, C. F. Conde, and A. Conde, "Kinetics of nanocrystallization in FeCoNbB(Cu) alloys," *Appl. Phys. A Mater. Sci. Process.*, vol. 76, no. 4, pp. 571–575, Mar. 2003.
[56] H. Hermann, "Crystallization Kinetics of Metallic Glasses on a Nanometer Scale," *Mater. Sci. Forum*, vol. 307, pp. 113–118, 1999.
[57] C. Zener, "Theory of growth of spherical precipitates from solid solution," *J. Appl. Phys.*, vol. 20, no. 10, pp. 950–953, 1949.
[58] K. Hono, H. Onodera, J. S. Pedersen, and S. Linderoth, "Cu Clustering Stage Before the Crystallization in Fe-Si-B-Nb-Cu AMORPHOUS ALLOYS," vol. 12, pp. 693–696, 1999.
[59] M. E. McHenry, S. Shen, P. Ohodnicki, S. Kernion, A. Leary, V. Keylin, and J. Huth, "NANOCOMPOSITE ALLOY DESIGN FOR HIGH FREQUENCY POWER CONVERSION APPLICATIONS," pp. 275–282, 2012.
[60] M. T. Clavaguera-Mora, N. Clavaguera, D. Crespo, and T. Pradell, *Crystallisation kinetics and microstructure development in metallic systems*, vol. 47, no. 6. 2002.
[61] P. Ohodnicki, N. C. Cates, D. E. Laughlin, M. E. McHenry, and M. Widom, "Ab initio theoretical study of magnetization and phase stability of the (Fe,Co,Ni)23B6 and (Fe,Co,Ni)23Zr6 structures of Cr23C6 and Mn23Th6 prototypes," *Phys. Rev. B*, vol. 78, no. 14, p. 144414, Oct. 2008.
[62] S. Kernion, V. Keylin, J. Huth, and M. E. McHenry, "Secondary crystallization in (Fe65Co35)79.5+xB13Nb4−xSi2Cu1.5 and (Fe65Co35)83B10Nb4Si2Cu1 nanocomposite alloys," *J. Appl. Phys.*, vol. 111, no. 7, p. 07A329, 2012.
[63] V. G. Harris, W. T. Elam, and C. Vittoria, "FMR and EXAFS Modeling of Heat-Treated Fe-Rich and CO-Rich TM-M Thin Films," vol. 21, no. 4, pp. 3620–3639, 1991.
[64] R. C. O'Handley, J. Megusar, S.-W. Sun, Y. Hara, and N. J. Grant, "Magnetization process in devitrified glassy alloy," *J. Appl. Phys.*, vol. 57, no. 8, p. 3563, 1985.
[65] J. L. H. Aaronson, M. Enomoto, *Mechanism of Diffusional Phase Transformations in Metals and Alloys*.

London: Taylor & Francis Group, 2010.
[66] A. Hsiao, M. E. McHenry, D. E. Laughlin, M. Kramer, C. Ashe, and T. Ohkubo, "The Thermal , Magnetic , and Structural Characterization of the Crystallization Amorphous Soft Magnetic Ribbon," vol. 38, no. 5, pp. 3039–3044, 2002.
[67] S. Shen, P. Ohodnicki, S. Kernion, and M. E. McHenry, "Two-current model of the composition dependence of resistivity in amorphous (Fe100 − xCox) 89 − yZr7B4Cuy alloys using a rigid-band assumption Two-current model of the composition dependence of resistivity in," vol. 103705, pp. 1–6, 2012.
[68] J. W. F. Dorleijn and a R. Miedema, "A quantitative investigation of the two current conduction in nickel alloys," *J. Phys. F Met. Phys.*, vol. 5, no. 3, pp. 487–496, 2001.
[69] P. Ohodnicki, J. Long, D. E. Laughlin, M. E. McHenry, V. Keylin, and J. Huth, "Composition dependence of field induced anisotropy in ferromagnetic (Co,Fe)[sub 89]Zr[sub 7]B[sub 4] and (Co,Fe)[sub 88]Zr[sub 7]B[sub 4]Cu[sub 1] amorphous and nanocrystalline ribbons," *J. Appl. Phys.*, vol. 104, no. 11, p. 113909, 2008.
[70] M. E. McHenry and D. E. Laughlin, *19 - Magnetic Properties of Metals and Alloys*, Fifth Edit., vol. 1. Elsevier B.V., 2015.
[71] R. C. O'Handley, "Magnetostriction of Co80−xTxB20 (T = Fe, Mn, Cr, or V) glasses," *J. Appl. Phys.*, vol. 52, no. 3, p. 1841, 1981.
[72] a Makino, T. Bitoh, A. Kojima, A. Inoue, and T. Masumoto, "Magnetic properties of zero-magnetostrictive nanocrystalline Fe–Zr–Nb–B soft magnetic alloys with high magnetic induction," *J. Magn. Magn. Mater.*, vol. 215–216, pp. 288–292, Jun. 2000.
[73] M. A. Willard, J. C. Claassen, R. M. Stroud, T. L. Francavilla, and V. G. Harris, "(Ni , Fe , Co) -Based Nanocrystalline Soft Magnets With Near-Zero Magnetostriction," vol. 38, no. 5, pp. 3045–3050, 2002.
[74] D. Korn, H. Pfeifle, and G. Zibold, "Electrical Resistivity of Amorphous Alloys," vol. 202, pp. 195–202, 1974.
[75] M. S. Lucas, W. C. Bourne, a. O. Sheets, L. Brunke, M. D. Alexander, J. M. Shank, E. Michel, S. L. Semiatin, J. Horwath, and Z. Turgut, "Nanocrystalline Hf and Ta containing FeCo based alloys for high frequency applications," *Mater. Sci. Eng. B Solid-State Mater. Adv. Technol.*, vol. 176, no. 14, pp. 1079–1084, 2011.
[76] M. Peter, A. a. Manuel, L. Hoffmann, and A. Shukla, "Electronic Structure and magnetic properties of dilute Fe alloys with transition-metal impurities," *Mater. Sci. Forum*, vol. 175–178, no. 12, pp. 71–76, 1995.
[77] F. Audebert, S. Vázquez, A. Gutierrez, I. Vergara, G. Alvarez, A. Garcia Escorial, and H. Sirkin, "Mechanical and Corrosion Behaviour of Al-Fe-Nb Amorphous Alloys," *Mater. Sci. Forum*, vol. 269–272, pp. 837–842, 1998.
[78] J. Friedel, "Metallic alloys," *Nuovo Cim.*, vol. 2, pp. 287–311, 1958.
[79] K. Fischer, "Theory of Dilute Magnetic Alloys," *phys. stat. sol.*, vol. 46, no. 11, pp. 11–52, 1971.
[80] C. L. Cook and P. V. Smith, "Virtual bound states in dilute transition metal and noble metal based disordered alloys," *J. Phys.*, vol. 1344, 1974.
[81] D. Seib and W. Spicer, "Physical Evidence For the Validity of the Virtual Bound State Model for Cu-Ni Alloys," *Phys. Rev. Lett.*, vol. 20, no. 2, pp. 1441–1444, 1968.
[82] I. Borbely, "Resonance and virtual bound state solutions of the radial Schrodinger equation," pp. 1–32, 2008.
[83] R. Jacobs, E. Babic, and J. Xanthakis, "Virtual bound states in transition-metal alloys," vol. 1941, 1985.
[84] A. Clogston, "Impurity States in Metals," *Phys. Rev.*, vol. 125, no. 2, p. 439, 1962.
[85] V. S. Stepanyuk, R. Zeller, and P. H. Dederichs, "Electronic structure and magnetic properties of dilute Co alloys with transition-metal impurities," *Phys. Rev. B*, vol. 49, no. 8, pp. 5157–5164, 1994.
[86] J. Kondo, "Theory of Dilute Magnetic Alloys," in *Modern Theory of Magnetism in Metals and Alloys*,

1970, pp. 183–280.
[87] I. Lykissa, S. Y. Li, M. Ramzan, S. Chakraborty, R. Ahuja, C. G. Granqvist, and G. A. Niklasson, "Electronic density-of-states of amorphous vanadium pentoxide films: Electrochemical data and density functional theory calculations," *J. Appl. Phys.*, vol. 115, no. 18, 2014.
[88] H. Tanaka, S. Takayama, M. Hasegawa, T. Fukunaga, U. Mizutani, A. Fujita, and K. Fukamichi, "Electronic Structure and magnetism of amorphous CoB alloys," *Phys. Rev. B*, vol. 47, no. 5, pp. 2671–2677, 1993.
[89] J. Hafner, M. Tegze, and C. Becker, "Amorphous Magnetism in Fe-B Alloys: First-Principles Spin-Polarized Electronic-Structure Calculations," *Phys. Rev. B*, vol. 49, no. 1, pp. 285–298, 1994.
[90] P. W. Anderson, "Localized Magnetic States in Metals," *Nuovo Cim.*, vol. 124, 1961.
[91] D. E. Laughlin and K. Hono, *Physical Metallurgy*, V. Oxford: Elsevier, 2014.
[92] P. W. Anderson, "Local moments and localized States.," *Science*, vol. 201, no. 4353, pp. 307–16, Jul. 1978.
[93] I. Borbély, "Resonance and virtual bound state solutions of the radial Schrödinger equation," pp. 1–32, 2008.
[94] H. Beckmann and G. Bergmann, "Success and failure of the Friedel-Anderson resonance model for magnetic impurities: 3d impurities on the surface of Au.," *Phys. Rev. B. Condens. Matter*, vol. 54, no. 1, pp. 368–372, Jul. 1996.
[95] D. Langreth, "Friedel Sum Rule for Anderson's Model of Localized Impurity States," *Phys. Rev.*, vol. 150, no. 2, 1966.
[96] J. Deutz, P. H. Dederichs, and R. Zeller, "Local density of states of impurities in Al," *J. Phys. F Met. Phys.*, vol. 11, no. 9, pp. 1787–1800, 2000.
[97] V. Anisimov, P. Antropov, A. Liechtenstein, V. Gubanov, and A. Postnikov, "Electronic Structure and magnetic properties of 3d impurities in ferromagnetic metals," *Phys. Rev. B*, vol. 37, no. 10, pp. 8186–8190, 1986.
[98] R. M. Nieminen and M. Puska, "3d impurities in Al: density functional results," *J. Phys. F Met. Phys.*, vol. 10, no. 5, pp. L123–L127, 2000.
[99] F. Batallan, I. Rosenman, and C. B. Sommers, "Band structure and Fermi surface of hcp ferromagnetic cobalt," *Phys. Rev. B*, vol. 11, no. 1, pp. 545–557, 1975.
[100] Peter Hadley (Graz University of Technology), "http." [Online]. Available: http://lamp.tu-graz.ac.at/~hadley/ss1/materials/dos/cobalt.html.
[101] A. Makino, T. Hatanai, A. Inoue, and T. Masumoto, "Nanocrystalline soft magnetic Fe-M-B (M = Zr, Hf, Nb) alloys and their applications," vol. 226228, pp. 594–602, 1997.
[102] Y. . Wu, T. Bitoh, K. Hono, A. Makino, and A. Inoue, "MICROSTRUCTURE AND PROPERTIES OF NANOCRYSTALLINE Fe – Zr – Nb – B SOFT MAGNETIC ALLOYS WITH LOW MAGNETOSTRICTION," vol. 49, pp. 4069–4077, 2001.
[103] V. DeGeorge, S. Shen, P. Ohodnicki, M. Andio, and M. E. McHenry, "Multiphase Resistivity Model for Magnetic Nanocomposites Developed for High Frequency, High Power Transformation," *J. Electron. Mater.*, Dec. 2013.
[104] M. Oring, "Materials Science of Thing Films," 1992.
[105] W. Callister and D. Rethwisch, *Fundamentals of Materials Sicence and Enginee*, no. 3. 2008.
[106] J. M. Silveyra, P. Xu, V. Keylin, V. Degeorge, A. Leary, and M. E. McHenry, "Amorphous and Nanocomposite Materials for Energy-Efficient Electric Motors," *J. Electron. Mater.*, no. August, 2015.